UNLV Theses, Dissertations, Professional Papers, and Capstones

5-1-2020

Remote Radiation Sensing using Robotic Platforms

Monia Kazemeini

REMOTE RADIATION SENSING USING ROBOTIC PLATFORMS

By

Monia Kazemeini

Bachelor of Science – Mechanical Engineering
University of Nevada, Las Vegas
2015

A dissertation submitted in partial fulfillment
of the requirements for the

Doctor of Philosophy – Mechanical Engineering

Department of Mechanical Engineering
Howard R. Hughes College of Engineering
The Graduate College

University of Nevada, Las Vegas
May 2020

UNLV | GRADUATE COLLEGE

Dissertation Approval

The Graduate College
The University of Nevada, Las Vegas

April 23, 2020

This dissertation prepared by

Monia Kazemeini

entitled

Remote Radiation Sensing Using Robotic Platforms

is approved in partial fulfillment of the requirements for the degree of

Doctor of Philosophy – Mechanical Engineering
Department of Mechanical Engineering

Alexander Barzilov, Ph.D.   Kathryn Hausbeck Korgan, Ph.D.
Examination Committee Chair   *Graduate College Dean*

Yi-Tung Chen, Ph.D.
Examination Committee Member

William Culbreth, Ph.D.
Examination Committee Member

Woosoon Yim, Ph.D.
Examination Committee Member

Moses Karakouzian, Ph.D.
Graduate College Faculty Representative

Abstract

Remote Radiation Sensing Using Robotic Platforms

By

Monia Kazemeini

Dr. Alexander Barzilov, Examination Committee Chair

Associate Professor of Mechanical Engineering

University of Nevada, Las Vegas

Remote sensing of ionizing radiation has a significant role in waste management, nuclear material management and nonproliferation, radiation safety, and accident response in situations such as the Fukushima nuclear power plant accident. Robotic platforms are able to surpass the number of tasks that could be achieved by humans. With the use of robots, the operator's radiation exposure can be considerably decreased. Remote sensing allows for the evaluation and monitoring of radiological contamination in hazardous and hard to reach areas and locating radiation sources. In this work, gamma-ray and neutron sensors were integrated onto the unmanned aerial systems (UAS) making it possible to assay the unsafe zones remotely. Radiation data were automatically processed onboard of the smart sensor (segregation of photon and neutron signatures, gamma spectra analysis) and fused with the GPS data. This approach allows for the radiation sensor data to be dynamically tracked and mapped thus enabling further analysis of the radiation flux in the time and space domains. Maximum likelihood estimation (MLE) technique was used to locate the position of the radiation source based on the signal intensities measured in three or more locations by a single UAS or simultaneously by multiple UAS. The probabilities to locate a source with an unknown yield in an assayed area were calculated. If the robotic platforms are exposed to ionizing

radiation, radiation damage occurs in the electronics components, limiting the platform's operational time. The estimation of radiation damage of the components is important in order to optimize the robot's operational lifetime in contaminated zones. Displacement per atom (DPA) characterizes the displacement damage on materials incurred by the radiation, which affects the macroscopic crystal defects. DPA depicts how many times atoms have been displaced from their lattice sites, representing the damage-based exposure unit. The FLUKA and SRIM/TRIM codes were used to analyze the DPA and ions transport processes in components of UAS and ground platforms. Packaging and the shielding designs were determined so that the operational time of the robot is increased.

Acknowledgements

One of the greatest decisions I made in my life was to go for my Ph.D. degree. I have never had such a big challenge in my life. However, knowing that I have come this far makes me feel so accomplished about myself. I did not do it all alone though, I had a strong team who supported me. I could had never done it without my professors and family. I am forever grateful for them.

First, I would like to thank my advisor, Dr. Barzilov. Dr. Barzilov provided me guidance and assistance on a regular basis to achieve my Ph.D. degree. Ever since Dr. Barzilov has become my advisor, I have become a much more confident student/researcher/ and leader. He encouraged and supported me to become better engineer every day and to not give up no matter how hard research or school gets. He taught me that hard work leads to success. I am just very thankful to know that I am able to go to Dr. Barzilov for any counsel that I will ever need. Dr. Barzilov has made a huge difference in my life. I don't know how I will ever thank him.

I would like to thank Dr. Culbreth. He is a very knowledgeable and creative professor that I learned something new from him every day. Dr. Culbreth always provided me with advice for anything in life. He told me not to give up and always look for clever solutions to problems. I developed the mentality that anything is possible because of him. He made sure that every single student was in the path for success. I am very thankful that not only do I have Dr. Culbreth as a professor, but a lifelong friend.

I would like to thank Dr. Yim and his team. They provided me so much guidance and information regarding robotic platforms. This dissertation would not be possible without them. I don't know how to thank them for guidance and support. I was very lucky to have them on my

side throughout my entire Ph.D. studies. Dr. Yim made me understand the importance of teamwork and how teamwork leads to success.

I would like to thank the rest of my committee members, Dr. Karakouzian and Dr. Chen for their guidance. I don't think I could ever thank them for their time and support. It amazed me how much knowledge and experience each one of them had in my prospectus defense. What made me feel so lucky is that each one of them wanted me to be successful. I hope one day I will become like them. I wish I had the words to thank them.

I would like to thank Dr. Novikov and his team for their collaboration. They provided so much guidance and advice on the research project.

I also would like to thank my mom and dad. They have always believed in me and told me to go after my dreams no matter what. Honestly, I don't know what I would have done without them. No matter what, they supported me in everything and always had my back. They were always there to remind me that I am capable of anything. My parents were always proud of me no matter what. They inspired me to dream big, work hard, and never give up. I am truly blessed to have such amazing parents in my life. I love them more than anything in the world.

I would like to thank my sister, Sarah. She was there for me in the middle of the nights and sat with me through the sweat and tears. Sarah always reassured me that everything will be okay. I not only have an amazing sister who I can count on, but also a best friend.

I would like to thank my entire family, especially my two grandfathers who passed away. My grandfathers only saw the tears, but now I am achieving a huge milestone, they couldn't see me. I hope I made you guys proud. Also, my entire family has always been so supportive in everything that I have done.

I would also like to thank my dog, Billy. He isn't here to see me graduate, but he made a huge difference in my academics and life. Every day was so special because of him. Billy was so full of life and always was there when I needed someone most. It breaks my heart that my best friend is not with me when I graduate.

Dedication

To my mother and father

Table of Contents

List of Tables

List of Figures

xiv

Chapter 1: Introduction

1.1 Motivation for Study

Sensing of radiological and nuclear materials plays a significant role in environmental security and radiation safety of nuclear facilities and nuclear power plants (NPP) in a normal operation regime, nonproliferation tasks, and accidental situations such as the Fukushima NPP disaster. Radioactive materials can be released into the environment as a result of technical accident at the facilities or natural cataclysms. After the Fukushima NPP accident, expert teams involved in the accident analysis called for a need of easily implementable sensors with wireless control and data transmission so that extensive measurements could be conducted without being dependent on the NPP infrastructure that might be affected by the disaster. Remote radiation sensing allows for the evaluation and monitoring of radiological contamination in hazardous and hard to reach areas where the contamination is unknown for the personnel and the public. In addition, remote sensing technologies can be used to locate lost, displaced or stolen sources, which cause contamination of infrastructure and risking irradiation of the people. Radiation monitoring technologies based on robotic platforms equipped with navigation tools are necessary for the assay of unsafe zones. The use of remote sensing capabilities is increasing rapidly. There has been a need to collect radiological information over a large area without risking exposure to personnel, and a surge deployment of monitoring tools.

To address these needs, the remote radiation sensing technology was developed. The goal of the project is to provide a robotic based solution for radiation sensing capabilities. The main priority of remote sensing is safety and a quicker method of inspection of wide areas. Gamma-ray and neutron sensors were integrated onto the robotic platforms for remote measurements in the field conditions. Radiation data were automatically processed onboard of the smart sensor

1

(segregation of photon and neutron signatures, gamma spectra analysis) and fused with the GPS data. Robotic systems allow for the radiation sensors data to be dynamically tracked enabling further analysis of the radiation flux in the temporal and spatial domains. In order to increase the situational awareness of the personnel, robotic platforms can be used for the mapping of unsafe areas and prognostics of radiological situation.

Two types of ambient temperature radiation sensors were studied. Cadmium Zinc Telluride (CZT) detectors have been a promising solution to the increasing demand for detection of x-rays and gamma rays. CZT detectors are widely used as high-resolution gamma ray spectrometers. This semiconductor converts photons into charged carriers. Due to its high atomic number, it has a high stopping power for photons of high energies when compared to other semiconductors. Its large band-gap energy allows for the operation at room temperature. Compared to Sodium Iodide (NaI) detectors, CZT detectors have a greater linear attenuation coefficient. They are able to process more than ten million photons per second. The thicker the CZT crystal, the higher is the energy that can be measured. Some of the main advantages of CZT detectors are the direct conversion of x-ray or gamma rays into electron hole pairs, the energy resolution, low dead space, high spatial resolution, its operation at room temperature, and its stable performance. Its energy range is from 30 keV to 3 MeV. The energy resolution was measured to be less than 2% at 662 keV, which is essential for identification of gamma emitters. The CZT detector operates as follows. The gamma radiation deposits energy into the CZT crystal. Then, electron hole pairs are created, moving in the electric field. The resulting electric current signal is sent to a preamplifier, where a voltage pulse is generated. The shaping amplifier converts this signal to a Gaussian shaped waveform. Lastly, the MCA produces the photon spectrum.

Another type of detector studied in this project is the scintillation detector. Scintillators convert the energy that is deposited in the detector medium by the ionizing radiation into an optical output, or pulses of scintillation light. The ionizing radiation can be alpha particles, beta particles, neutrons, x-rays, or gamma rays. The scintillating material emits pulse of light that can be detected by a photomultiplier tube (PMT). The photocathode of the PMT converts the photons into photoelectrons. An electric field accelerates the photoelectrons towards the dynodes of the PMT. Hence, each scintillation signal generates an electric current pulse on the anode for the PMT. Scintillation detectors can be utilized for measurements of energy of different particles. The $Cs_2LiYCl_6:Ce^{3+}$ (CLYC) scintillation sensor was used for simultaneous neutron and photon measurements by a single sensor cell.

The scintillation properties of elpasolites enable gamma-ray spectrometry. CLYC is able to produce 20 thousand scintillation photons under the incident gamma rays per 1 MeV. By $^6Li(n,\alpha)^3H$ nuclear reaction, neutrons are detected by with the emission of energetic charge particles, which 70 thousand scintillation photons are generated in the crystal per one thermal neutron. Due to the different decay times after neutron and photon excitations, CLYC makes it possible to segregate signals caused by these two radiations using the neutron/photon pulse shape discrimination (PSD) techniques. CLYC can be used as a fast neutron sensor via $^{35}Cl(n,p)^{35}S$ reaction with the Q-value of 615 keV: the emitted proton's energy equals 615 keV plus the incident neutron's energy. Hence, the neutron energy can be gathered from the measured full energy proton peak value.

1.2 Dissertation Outline

There are three objectives in this dissertation. Each objective holds three tasks. Objective one is the integration of the ambient-temperature radiation sensors onto the robotic platform. The first task in this objective is to have the radiation sensors integrated with the platform using Robot Operating System (ROS). ROS is an open source software suite used in many robotic applications and is utilized for the processing of data from sensors and components of robotic platforms. ROS operates using independent nodes by exchanging information between them. A node can publish to a topic or subscribe to a topic, or both. The second task involves the 'plug-and-play' (or 'plug-and-fly' for aerial drones) operation of the detectors to be designed. This works by the operating system detecting and configuring the internal and external devices. It supports 'hot plugging' and 'hot unplugging' of the detectors to the UAS meaning that the operator does not need to set the component's parameters and tune the sensors. When the radiation sensor is plugged into the robot's onboard computer via the USB interface, the operating system recognizes the device. The final task of this objective is to have the operating system process and analyze the sensor data onboard in the 'smart sensor' approach and then publish the results forming a message. The measurements contain real time kinematic (RTK) GPS data and a timestamp. The analysis of the measured sensor's data should be carried out using an onboard computer while taking into account its limited data processing capabilities.

The second objective is to develop the source-search method using a single platform and multiple platforms. The first task of this objective is to develop onboard data analysis methods: (a) to use PSD technique to segregate gamma and neutron signatures (for the CLYC sensor), and (b) to use the Mariscotti technique for the automatic identification of gamma-ray peaks in the presence of background (for both CLYC and CZT sensors). PSD allows for the identification of

signals produced by a gamma ray or a neutron. This is found by the difference of the total integration time and the partial integration time divided by the partial integration time. Neutrons and gamma rays produced slightly different signals in scintillation materials. The gamma peak identification approach assumes that these peaks are described by a Gaussian and the background is described by a linear function within a small energy range (i.e., several peak widths). The peak centroid was determined as the center of the Gaussian, and then the intensity of the peak was calculated. After the data analysis, the peak's energy values and intensities are used by ROS for further data fusion. The sources were identified using this technique. The second task of this objective is to use Maximum likelihood estimation (MLE) technique. This technique is employed to locate the position of the radiation source based on the measured peak intensities. This is achieved by the measurements of three or more locations by a single UAS or simultaneously by multiple UAS. The detectors are assumed to have an omnidirectional signal acceptance and the $1/R^2$ signal strength dependence, R represents the distance from the source to the detector. The probabilities of a source being present in an area with an unknown intensity were calculated at each of the point of the area under scrutiny. The intensity was evaluated using the position of the source and the detected counts. The third task of this objective is to use Monte Carlo N-Particle Transport Code (MCNP6) for high fidelity modeling of a radiation field. The source seeking and contour mapping algorithms were tested using these radiation field data.

The third objective is to evaluate radiation damage in electronic components of robots. The estimation of radiation damage of the robotic platform is important in order to optimize the robot's operational lifetime while it is irradiated. Displacement per atom (DPA) represents the displacement damage on materials incurred by the radiation, which affects the macroscopic crystal defects. DPA depicts how many times atoms have been displaced from their lattice sites,

representing the damage-based exposure unit. This unit is directly related to the number of Frenkel pairs. The displacement is induced by a primary knock on atom (PKA) caused by the elastic scattering of incident particles. The first task of this objective is to determine the DPA on the electronic components of the robotic platform. The FLUKA code was used to calculate the DPA using the Kinchin - Pease damage model. Photons and neutrons interacting with the crystalline materials result in the development of lattice defects. The electronic components are affected the most while under irradiation, which has a consequence of affecting the platform's operational time. The SRIM/TRIM code was used to analyze the ions transport processes in the UAS components. This program is used to analyze energetic processes of ion-solid interactions and has a high accuracy of the energy loss/transfer and collision processes. The second task would be to determine the operational time of the robotic platforms under various irradiation conditions. For the protection of the robotic platforms from damage, there are three possible options: to minimize time at the contamination zone, to keep distance from the contaminated zone, or to utilize shielding so that the electronic parts are protected. The third task of this objective is to determine the packaging of the components and the shielding design so that there would be an increase in the robot's lifetime in areas where radiation dose levels are high.

Chapter 2: Literature Review

2.1 Introduction

Matter is anything that has a mass and space. This includes solids, liquids, gases, and plasma. Atoms are the building blocks of matter and consist of subatomic particles, which are protons, neutrons, and electrons. Protons (nucleons) and neutrons form the center of the atom called the nucleus. A cloud of electrons orbits the nucleus, carrying a negative charge. The cloud has a 10,000 times larger radius than the nucleus [1]. Protons and neutrons have nearly the same mass, while the electrons are very lightweight. There is an equal number of protons and electrons in atoms. The atomic number is based on the number of protons and the type of element. The number of neutrons sometimes varies with the number of protons, making it into a different isotope.

Material is considered to be radioactive if it contains an unstable nuclei and releases protons or neutrons in attempt to reach a stable state. The particles that are being emitted during the radioactive decay are called radiation. The radioactivity refers to the rate of the emitting of radiation. There are types of ionizing radiation: alpha, beta, gamma, x-ray, and neutron particles. All types of ionizing radiation are affected by unstable atoms.

Alpha radiation undergoes radioactive decay typically of heavier elements, such as heavier than lead. Alpha particles consist of two protons and two neutrons that are strongly bound. The emission of the particle reduces the atomic number by two and the atomic mass by four. They are relatively slow compared to other forms of radiation, traveling at 5 to 7 percent of the speed of light. Alpha particles cause multiple ionizations in a short distance and can be blocked after traveling about 1.2 inches of air, about 0.008 inches of water, or even human skin or a piece of paper. The alpha particle decay is described by Equation 1.

$$\begin{smallmatrix} A \\ Z \end{smallmatrix} M \rightarrow \begin{smallmatrix} A-4 \\ A-2 \end{smallmatrix}(Z-2) + \begin{smallmatrix} 4 \\ 2 \end{smallmatrix}\alpha \qquad\qquad\qquad \textbf{Equation 1}$$

Where *A* is the atomic mass, *Z* is the atomic number, *M* is the atom before the decay, and α is the alpha particle. Common alpha emitters include radium-226, uranium-238, and plutonium-239.

Beta particles are high energy electrons or positrons that are emitted from the nucleus by radionuclides by beta decay. Beta decay is when atoms emit beta particles. This occurs when a nuclear has too many protons or neutrons. There are two types of beta decay, which are positive beta decay and negative beta decay. Positive beta decay is when a positron and a neutrino is released; Negative beta decay is when an electron and an antineutrino is released. Beta particles can be stopped after traveling in about 10 feet of air, about 2 inches of water, or a thin layer of glass or metal. Equation 2 shows negative beta decay and Equation 3 shows the positive beta decay.

$$\begin{smallmatrix} A \\ Z \end{smallmatrix} M \rightarrow \begin{smallmatrix} A \\ Z+1 \end{smallmatrix}N + \beta^- + \bar{v} \qquad\qquad\qquad \textbf{Equation 2}$$

$$\begin{smallmatrix} A \\ Z \end{smallmatrix} M \rightarrow \begin{smallmatrix} A \\ Z-1 \end{smallmatrix}N + \beta^+ + v \qquad\qquad\qquad \textbf{Equation 3}$$

Where *A* is the atomic mass, *Z* is the atomic number, *M* is the atom before to decay, *N* is the atom after the decay, β^- is the electron, $\bar{v}$ is an antineutrino, β^+ is positron, and v is a neutrino.

Gamma rays are a form of electromagnetic radiation. They are the most energetic form of electromagnetic radiation, having a wavelength of less than one-tenth of a nanometer. Electromagnetic radiation is referred to as photons. Photons are massless particles that travel in a wavelength at the speed of light. Gamma ray photons have the highest energy in the electromagnetic radiation spectrum, while having the shortest wavelengths. They can pass through any kinds of materials. Dense materials, such as lead, can be used as shielding to slow or stop gamma ray photons. The nucleus in the excited state is able to give off one or more photons.

The emission does not affect the neutrons or the photons in the nucleus; however, it moves the nucleus from a higher to a lower energy state making is stable. Typically, the gamma ray emission follows beta decay, alpha decay, or other nuclear decay processes. Common gamma ray emitters include cobalt-60, cesium-137, and americium-241. Gamma rays interact with matter by three processes: Compton scattering, photoelectric absorption, and pair production.

The photoelectric absorption occurs when the gamma ray interacts with an electron bounded to the atom. Then, the gamma ray disappears, and one of the electrons is ejected from the atom. The atom has very little kinetic energy when it recoils. The ejected photoelectron has the same kinetic energy to the energy of the photon; however, it has less binding energy of the electron. The Compton effect, or Compton scattering is the elastic scattering of a photon by an electron, energy and momentum are conserved. The recoiling electron obtains kinetic energy; therefore, the energy of the scattered photon is less. Many difficult problems arise from the Compton scattering when being shielded. The reason is that the photon does not disappear and is free to interact with another part of the system. Pair production is the process where gamma ray interacts with the nuclear, and then the photon disappears. This creates an electron pair of a positron and a negatron.

X-rays are also a form of electromagnetic radiation, having no rest mass and no charge. Just like gamma rays, they have a high frequency (thus, a short wavelength). X-ray wavelengths are typically longer than gamma rays. It is defined that x-rays are emitted in atomic electron transitions and gamma rays are emitted by the nucleus. X-rays interact with matter by three processes: photoelectric effect, Compton scattering, and Rayleigh scattering. X-rays have penetrating matter and must be shielded by dense materials. Rayleigh scattering is a low energy limit of the Compton effect. The kinetic energy of the particle and the frequency of the photon so

9

no change from the effect of the scattering. It occurs from the result of the interaction of the incoming photon and electron. The binding energy is greater than the incoming photon.

Neutrons are electrically neutral and have a capability to penetrate materials. Neutrons are able to travel great distances in air. They are often stopped or slowed down in a medium containing hydrogen-containing material, such as water or polyethylene. Neutrons can make other objects radioactive (neutron activation). Neutron activation is the process where neutrons incite radioactivity to other materials. The nucleus captures neutrons and enters the excited state with the following de-excitation that leads to emission of radiation.

2.2 Radiation Detection Fundamentals

Radiation detectors are instruments used for detection and measurement of radiation which are caused by subatomic particles. They enable measuring ionization and generating an output. Semiconductors are typically used as a type of detector. Radiation detectors are chosen based on the sensitivity of the detector, the energy resolution, time resolution or pulse-resolving time, and the efficiency. Semiconductors are solid state devices that are similar to ionization chambers. In a semiconductor radiation detector, the incident radiation interacts with the detector material. The semiconductor then creates hole-electron pairs. The charged electrodes collect the hole-electron pairs by the migration of the electrons to the positive electrodes and the negative electrode's holes. This creates an electrical current pulse [2]. Typically, each pulse contains information such as the type, energy, event timing, and the number of particles arriving per unit time. The energy is required to produce electron-hole pairs is very low compared to the energy required to produce paired ions in gas detectors.

There has been an increasing demand for the detection of hard to find x-rays and gamma rays. CZT detectors have been a promising solution to that problem. Due to its high atomic number, it has a high stopping power for energies when compared to other semiconductors [3]. Its large band-gap energy allows for the operation at room temperature. Compared to Sodium Iodide (NaI) detectors, CZT detectors have a linear attenuation coefficient. They are able to process more than ten million photons per second per second. An important characteristic is the CZT crystal. The thicker the crystal, the higher the energy is measured. Some of the main advantages of the CZT detectors are the direct conversion of x-ray or gamma rays into electron hole pairs, the energy resolution, low dead space, high spatial resolution, it operates in room temperature, and its stable performance [4].

11

One of the most beneficial characteristics of the CZT detector is its relatively low dead space [5]. There is a minimum amount of time that is necessary so that the two separate events are recorded at two separate pulses, due to the response time of the electronics or the processes in the detector. The dead space is the minimal time separation that is required. The is a change that a true event is not recorded since the separate events occur too quickly after one another. Another benefit of the CZT detector is the spatial resolution.

The distance between the target being imaged and the platform determine a crucial role with the information that is obtained [6]. When sensors far away, precise detail is not obtained. Spatial resolution refers to the size of the smallest feature that has been received. It depends on their Instantaneous Field of View (IFOV). The IFOV is the cone of visibility of the detector, showing the area of what the detector inspects at a given altitude, the size that is determined from the IFOV by the distance, and the resolution cell and the determination of the maximum spatial resolution.

The CZT energy resolution is the ability for the detector to distinguish the peaks of gamma rays with close energies. A system is not able to accurately determine what energy a subatomic particle has hit the crystal, so therefore, it is vital to determine the range of values of the energy of radiation that is being detected. The full width half maximum (FWHM) is the width of the of the peak captured in an energy spectrum. The smaller the FWHM, the better energy resolution. Due to the good spectrometric characteristics and simple operation, the CZT detectors are convenient for dosimetry in remote detection situations [7].

The efficiency of the detector depends on several parameters. One parameter is the absolute efficiency, which it the ratio of counts obtained by the detector to the number of gamma rays emitted from the source. Intrinsic efficiency is the number of electric pulses recorded to the

number of gamma rays incident to the radiation detector. Lastly, there is the full-energy peak efficiency. This is the ratio the counts in the full energy peak corresponding to the energy to the number of photons emitted from the source. Experimental full energy peak efficiency is determined by Equation 4.

$$\varepsilon_{meas} = \frac{P}{A \cdot Y \cdot t}$$ **Equation 4**

Where P is the net peak area, t is the measurement time, A is the activity of the radionuclide, and Y is the yield of photons per nuclear transition. Lastly, there is the geometrical efficiency, which is the radio of photons emitted towards the detector to the number of photons emitted [8].

Another type of detector is called the scintillation detector. Scintillators convert the energy that is lost by the radiation into pulses of light [9]. The ionizing radiation is in the form of alpha particles, beta particles, x-rays, or gamma rays. The scintillating material produces pulse of light which is detected by an optical readout - a PMT or a solid-state silicon photomultiplier (SiPM). The photocathode of the PMT converts the incident photons into photoelectrons. The process in the scintillation detector is the following. The ionizing radiation encounters the scintillation medium. This gives off photons of visible light. The photons go through the crystal and strike the photocathode, which leads to the light entering the PMT. An electron is ejected from the photocathode since the photon hits the photocathode. The electron is then accelerated by the voltage and then strikes out other electrons [10]. This is where the electron multiplication process takes please. As a result, the scintillation produces a charge pulse on the anode of the PMT. Analysis of scintillation signals provides the capability to determine the energy of a particle or a photon.

13

When the diameter of the scintillation detectors increases, the solid angle of the detector also increases. The solid angle of the detector is important because it is what the detector 'sees.' This is an important factor in which it increases the detection efficiency, in addition to the thickness of the scintillator.

There are two types of scintillators: inorganic and organic scintillators [11]. In inorganic crystal lattices, the electrons occupy selected energy bands. Organic scintillators contain organic molecules that have symmetry properties based on the electron structure.

The elpasolite CLYC is coupled with a PMT and a miniature eMorpho digitizer equipped with a high voltage generator [12]. It has a density of 3.31 g/cm^3 and a refractive index of 1.81. The emission spectral range is from 275 nm to 450 nm with the peak being at 370 nm. The scintillation light yield is 20,000 photons per 1 MeV for gamma rays and 70,000 photons per one thermal neutron. The neutrons are detected by the CLYC via ^{6}Li(n,α)^{3}H reaction. The elpasolites have appropriate gamma spectroscopy capabilities [13, 14, 15, 16],　The photon energy of CLYC resolution is about 5% at 662 keV.

This elpasolite material exhibits neutron-gamma pulse shape PSD properties [17, 18]. The CLYC undergoes a fast CVL de-excitation with a 1-ns decay constant, which is then followed by a prompt Ce^{3+} decay with a 50-ns time constant. After a neutron event, the CLYC decays slower via the (Ce-STE) process with a 1-µs decay constant. The time differences allow for the separation of neutron and gamma induced signals.

2.3 Robotic Platforms

Robotic platforms are capable of doing many tasks they are programmed to do. They are utilized in many areas of industry. Emergency situations, such as the Fukushima Nuclear Power Plant disaster, are difficult to assay because of the risk of exposure to the operator. In addition, unforeseen factors can arise [19, 20, 21, 22]. Autonomous radiation mapping is a solution to locate hazardous areas where the contamination is unknown.

Robotic platforms equipped with radiation sensors are able to fulfil multiple tasks automatically without affecting human life. However, each robotic platform has its own weaknesses and benefits. Ground robotic platforms may have differential steering, meaning that the wheels on either side of the platform turn are different speeds. In addition, turning of the platforms may be different in areas where there is rough terrain. However, this type of configuration is simple to control. This robotic platform has high speed stability and efficiency.

The PhantomX AX Metal Hexapod MK-III by Interbotix Labs [23] , shown in Figure 1, an open platform of a 'spider robot' with a top deck that enables attachment of sensors and cameras, was utilized. It carries a 1 cm^3 CZT detector and a video camera that operates with an OmniVision OV5640 CMOS image sensor with a focal length of 3.6 mm [24]. This hexapod was chosen because of its idle mobility, robustness, and versatility. It controls six legs with three degrees of freedom for each leg and achieves superior mobility. This robot is able to adjust when the legs begin to fail.

Figure 1: PhantomX AX Hexapod MK-III in a desert terrain.

There are 18 AX-18A Dynamixel actuators [25] in the hexapod platform. The actuators are connecting joints of the robot enabling their versatile movements. It has the capability to track the speed, strength, position, and voltage. The microcontroller supports the position control. The Dynamixel actuator specifications are shown in Table 1. Each leg of the robot contains three actuators. The ArbotiX-M Robocontroller [26] manages the actuators, thus controlling the movement and direction of the robot. The actuators have the ability to move each of the legs separately. The robocontroller contains the AVR microcontroller, 2.4 GHz Xbees, dual motor drivers, and 3 pin servo headers for the input and output. The AX-18A Dynamixel actuator and the ArbotiX-M Robocontroller are shown in Figure 2a and Figure 2b, respectively.

Table 1: Dynamixel Actuator Specifications

Description	Data
Operating Voltage	12 V
Stall Torque	15.3 kg·cm
Weight	55 g
Size	32 mm × 50 mm × 40 mm
Resolution	0.29°
Operating Angle	300° or continuous turn
Internal Operating Temperature	-5°C to ~ 70°C
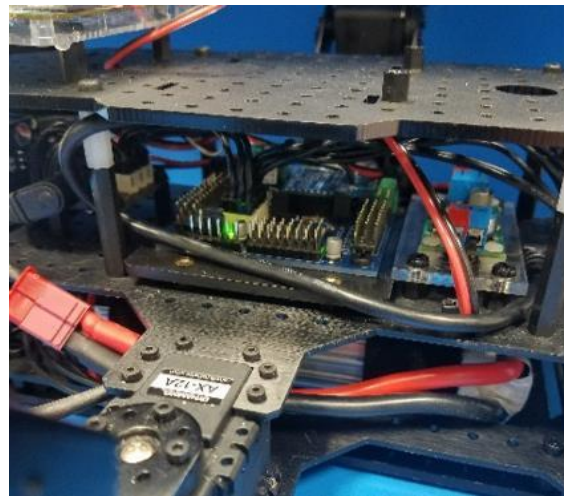
(a)   (b)

Figure 2: (a) AX-18A Dynamixel actuator; (b) ArbotiX-M Robocontroller.

The DJI S1000+ octocopter [27] was also used in this study as an unmanned aerial system (UAS) platform. The UAS is shown in Figure 3. This platform is powered by 6S Lithium polymers batteries. It has a takeoff weight of up to 11 kilograms and is estimated to fly 15 minutes. The landing gear is able to be raised which creates at 360-degree visibility. This octocopter was chosen due to its large, stable payload capacity, wide range of angles, and reduced vibrations for a camera resolution. The DJI S1000+ specifications are shown in Table 2.

Figure 3: DJI S1000+ Octocopter Platform [27].

Table 2: DJI S1000+ Octocopter Specifications

Description	Data
Diagonal Wheelbase	1045 mm
Frame Arm Length	386 mm
Weight	4.4 kg
Maximum Power Consumption	4000 W
Working Temperature Range	-10°C ~ +40°C
Propeller Diameter	380 mm

Another robotic platform used is a Jackal Unmanned Ground Vehicle (UGV) by ClearPath Robotics (Figure 4) [28]. This UGV is an efficient and fast-paced research platform, which is powerful and compact. Multiple sensors, cameras, and other accessories can be added to its mounting platform. In addition, the internal area is accessible to additional computing power or storage. The Jackal is made from an aluminum chassis prepared with a high torque 4×4 drivetrain for terrain operations. The weatherproof casing makes it possible to operate from -20°C to 45°C. The specifications of the Jackal are shown in Table 3.

Figure 4: Jackal by Clearpath Robotics [28].

Table 3. ClearPath Robotics Jackal

Description	Data
External Dimensions	$508 \times 430 \times 250$ mm
Internal Dimensions	$250 \times 100 \times 85$ mm
Weight	17 kg
Maximum Payload	20 kg
Max Speed	2.0 m/s
Run Time	4 hours

A Pixhawk 2.1 [29] was used as the flight controller of the UAS. The built-in inertial measurement unit (IMU) heating system will function under extreme temperatures that are below 0°C. In addition, it has robust interface connecters so that the shock and resistance would be improved. It contains an isolated and dampened IMU. It reduces interference to the sensors with the separate IMU and flight management unit (FMU) system. In addition, it reduces the vibration by reducing noise. There is an Intel carrier board that connects to the companion computer. The Pixhawk controller is shown in Figure 5.

Figure 5: Pixhawk 2.1 Flight Controller [29].

The CZT GR1-A module by Kromek [30] was integrated into the robotic platforms. This ambient temperature sensor allows for high resolution gamma-ray spectrometry. The module with a 1 cm^3 CZT crystal has (2.5 × 2.5 × 6.1) cm^3 volume; its weight is 49.2 grams. A USB interface was used to send signals to the onboard computer and to power the module, therefore there is no need for an external power supply. The power consumption of the CZT sensor is 250 mW.

2.4 Work Up to Date

Current technology allows for the remote detection of radioactive materials. Robotic platforms are able to surpass the number of tasks that could be achieved by humans. With this technique, humans are not exposed to high levels of radiation. Regulatory requirements require human radiation exposure to be "As Low as Reasonably Achievable," so therefore, robotic platforms are very important. After the Fukushima NPP accident, expert teams involved in the accident analysis called for a need of easily implementable sensors with wireless control and data transmission so that extensive measurements could be conducted. The use of remote sensing capabilities is increasing rapidly. However, in recent works, the current technologies have been less effective in respect since the radiation detection are not efficient while being measured. In addition, payload has become an issue, which influences the complexities and the capabilities of the detector that is being used [31]. In this case, a helicopter with a low budget radiation detector is used. This paper examined the use of the radiation detector with different algorithms to provide information regarding the area. One of the algorithms used was the Hough transform algorithm. The output produced a long list of source locations. In addition, it is very sparse and outputs an irregular map of the data. Figure 6 shows the helicopter being used and the outputs.
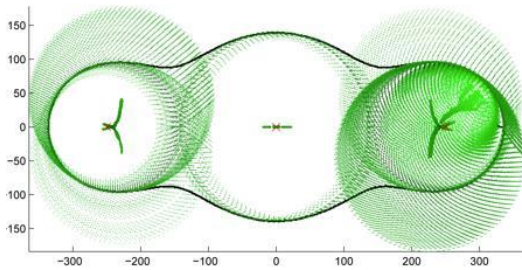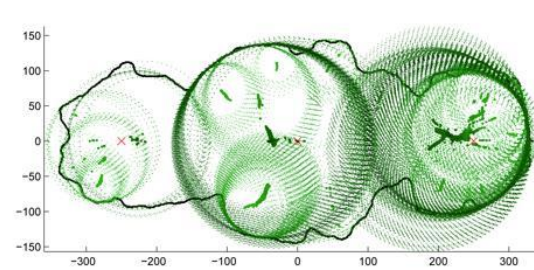
(a)
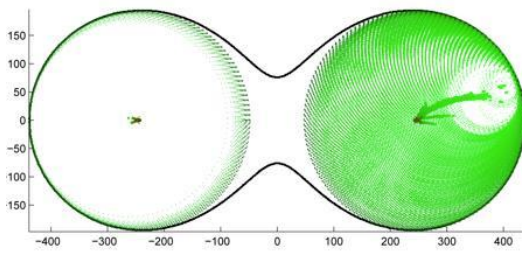
(a) Two Equal Sources—Ideal
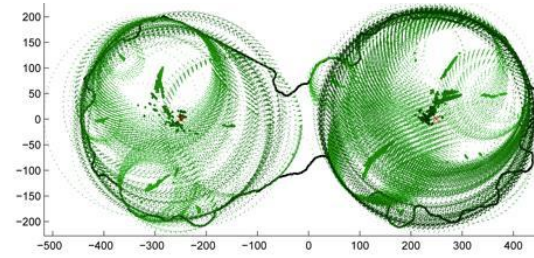
(b) Two Equal Sources—Stochastic

(c) Three Unequal Sources—Ideal

(d) Three Unequal Sources—Stochastic

(b)

Figure 6: (a) Helicopter used in [31], (b) Output Reproduced in Reference [31].

23

Another method is applied called the spatial deconvolution method in order to resolve the distribution and that it would determine a point source location. However, a helicopter is not idle because it would not be able to fit in narrow areas where there are dangerous levels of radiation.

In the paper [32], it addresses the capabilities of autonomous radiation detection systems using a BriLanCe 380 lanthanum bromide detector. The goal of this research is to improve the capabilities of the robotic system in the detection of gamma rays. The robotic system is able to achieve routine radiation surveying, radiation assay of objects, and close-in visual inspections. However, the system has constraints in order to improve its surveying capabilities. First, the system must perform a full sweep of the area. Second, the system must detect anomalous reading made by specialists. The instrumentation must be mounted so that it will be able to move around. Finally, the algorithm must be developed so that radioactive sources can be located. The paper is focusing on algorithms to improve the localization of sources. The algorithm is based on the recursive Bayesian estimation. The model is shown in Equation 5.

$$P\left(z_j \middle| I^j\right) = Poisson(\sum_{i=0}^{m} D(\hat{r})(\frac{I_j}{r_{ij}^2}))$$ **Equation 5**

The unit vector from the detector to the source is shown by $\hat{r}$. D is the directionality of the detector.

According to the research, two variables affect the detector count rates, which are the solid angle and crystal thickness. With a greater solid angle, there is an increased likelihood of interaction between the source and the detector. Areas where there is less thickness have a lower probability of interaction with the gamma ray.

In the paper [33], difference scenarios using multiple Unmanned Ground Vehicles (UAV) based on source seeking strategy in order to determine the position of a signal field, in addition to the contour mapping in circular formation flight. An existing source seeking algorithm is used

and improved for an enhanced signal source location. In order to achieve contour mapping of the signal field, the algorithm is modified. A formation control strategy is used and simplified so that the UAVs formation flight during the detection will stabilize. This paper addressed that the future work is to improve the combined controller for a cooperative contour mapping so that it could execute a better formation flight. The results are shown in Figure 7.
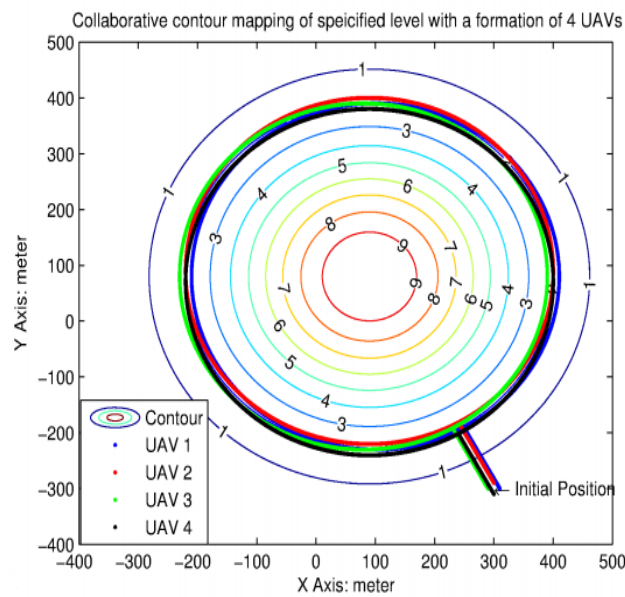
Figure 7: Contour mapping of Levels with a Formation of UAVs Reproduced from Reference [33].

In the paper [34] , the location of the monoenergetic and multi-energetic neutron is determined by algorithms developed by neutron time-of-flight (TOF). The monoenergetic neutron source's location is evaluated by the TOF variance and the gains at the minimum. The Maximum Likelihood method is used so that time-correlated measurements can be made. The way that the time-correlation is accomplished is by the neutron detectors and acquisition system. In addition,

this research addressed that the TOFs are achieved from time-correlation measurements by using three neutron detectors. This surrounds the area of the neutron source. The monoenergetic source location is acquired from the TOF using three detectors. The Maximum Likelihood method makes it possible to determine the location of the location along with the possible distributions for multi-energetic neutron sources. It is verified the maximum likelihood method is much more effective than other methods in this paper.

Radiation damaged caused by different radiation sources have been widely studied. This is of great importance since it affects the properties of the materials. In the paper [35], radiation damaged was calculated by the estimation of displacements cross sections. There were two methods studied in this case. First, the Monte Carlo assisted Classical Methods (MCCM) was used. This method replaced the distributions in particles with materials by those obtained by the Monte Carlo simulation of radiation transport. This would define the total number of atom displacements per volume unit. The next method used was the Cahn method. This considered three processes of gamma interaction with secondary electrons, which were Compton scattering, photo effect, and pair production. The results were then compared with the theoretical calculations. The MCCM method introduced the realistic treatment for gamma and electron transport. Results from this paper are shown in Figure 8. This shows MCCM's calculation and Cahn's estimation for Silicon using two values of displacement energy. There is an overestimation for the displacement energy at 15 eV and 30 eV. This shows that the estimation would decrease for higher gamma energies and lower displacement energies.
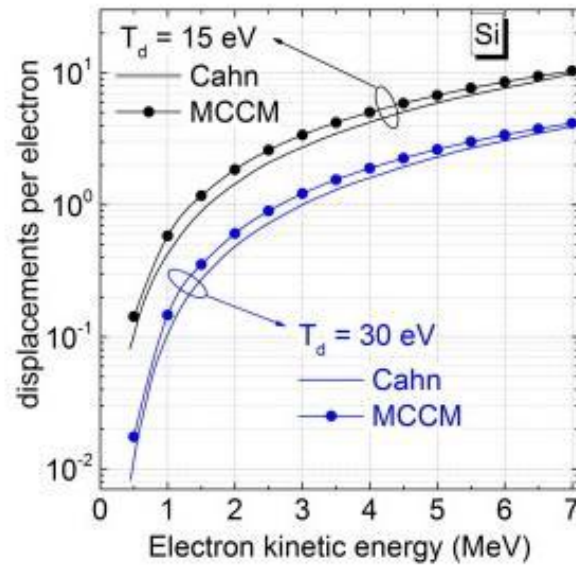
Figure 8: Silicon DPA Representing Cahn's Estimation and MCCM Calculation for Displacement Energy [35].

In the paper [36], the DPA was calculated using the SRIM Monte Carlo code. The DPA calculations were analyzed using simulations from the code. From this paper, it was observed that the SRIM package is a suitable tool for the simulation of a beam interaction with a solid, ion, and radiation defects. A disadvantage of SRIM is that it only uses neutral atoms, and charge effects are not taken into consideration.

Chapter 3: Radiation Detectors for Robotic Platforms

3.1 Radiation Sensors Integrated onto Robotic Platforms

Technologies of gamma ray sensing in radiation zones are vital for environmental safety and radiation safety. Hazardous radiological wastes can be a result of large nuclear projects; radiological materials can be displaced, lost, or smuggled [37, 38, 39, 40]. Additionally, they can be released into the environment due to man-made accidents or natural disasters. One example is the Fukushima Daiichi nuclear power plant disaster [41] that led to radiological contamination of the plant's infrastructure and territory adjacent to the plant. The use of Unmanned Aerial Systems (UAS) allows for the remote radiation sensing, mapping, and wide area search operations while keeping users away from the risk of exposure [42]. Small scale, multiuse UAS platforms equipped with navigation and radiation sensing capabilities permit for the surveillance in hard to reach, hazardous areas while allowing for the measurements to be dynamically tracked and mapped. The measured data could be used for situational awareness and further analysis of radiation fields in temporal and space domains [43]. Furthermore, based on the cooperative sensing algorithms, the UAS swarm can be programmed to search for unattended radiation sources [44]. In order to accomplish radiation monitoring tasks using UAS, gamma ray sensors should be integrated into a robotic aerial platform. The sensor's data analysis should be automated and carried out onboard taking into account limited computational resources of flight computers [45].

Since UAS has weight and size limitations for onboard components so that the flight efficiency is not reduced due to the payload, the choice of radiation sensors is important. Radiation sensors should be swappable (attached and detached from the robotic platform) in the field conditions [46]. The sensors should have low power requirements so that the integration into

the platform does not affect the battery power. The data processing limitations should be also considered. To address this necessity, two types of flight ready ambient temperature radiation sensors were developed: a CZT semiconductor sensor for high-resolution gamma spectrometry and the elpasolite scintillation sensor CLYC for neutron and gamma measurements. Both sensors were designed as plug-and-play interchangeable modules.

CZT detector technology has been a promising solution for the detection of gamma rays and x-rays [47]. This semiconductor material was chosen for gamma ray spectroscopy because of its high energy resolution and stable performance. A CZT module GR1A by Kromek was used. This $(2.5 \times 2.5 \times 6.1)$ cm^3 module weighing 49.2 grams contains a 1 cm^3 CZT crystal. This CZT detector has an energy range of 30 keV to 3 MeV. Its operating temperature range is from 0°C to 40°C. Its FWHM photon energy resolution is less than 2% at 662 keV.

The Kromek GR1A has a spectroscopy software in order to interpret the signals, called the MultiSpect Analysis [48]. This software is designed only for the Kromek's range of radiation detectors on Windows based computers. It is a specialized gamma ray spectroscopy software for the analysis of complex samples for the radionuclide identification. The acquisition from radiation detectors are analyzed and displayed. A spectrum is shown in Figure 9. Measurements were carried out using ^{22}Na, ^{60}Co, ^{133}Ba, and ^{137}Cs photon sources with known activities. Spectral data was recorded in 20-minute intervals and processed using the MultiSpect Analysis software provided with the detector. Figure 10 shows a comparison of sample spectra produced by ^{22}Na, ^{60}Co, and ^{137}Cs sources. The spectrum is displayed on an energy axis so that a more efficient comparison of data can be visualized.
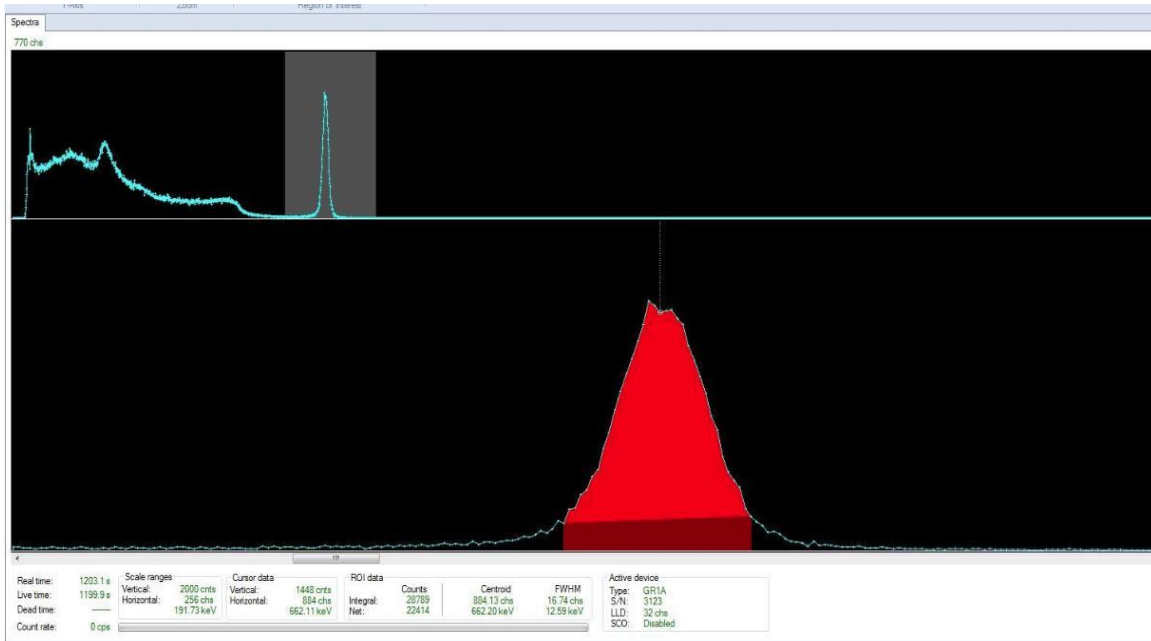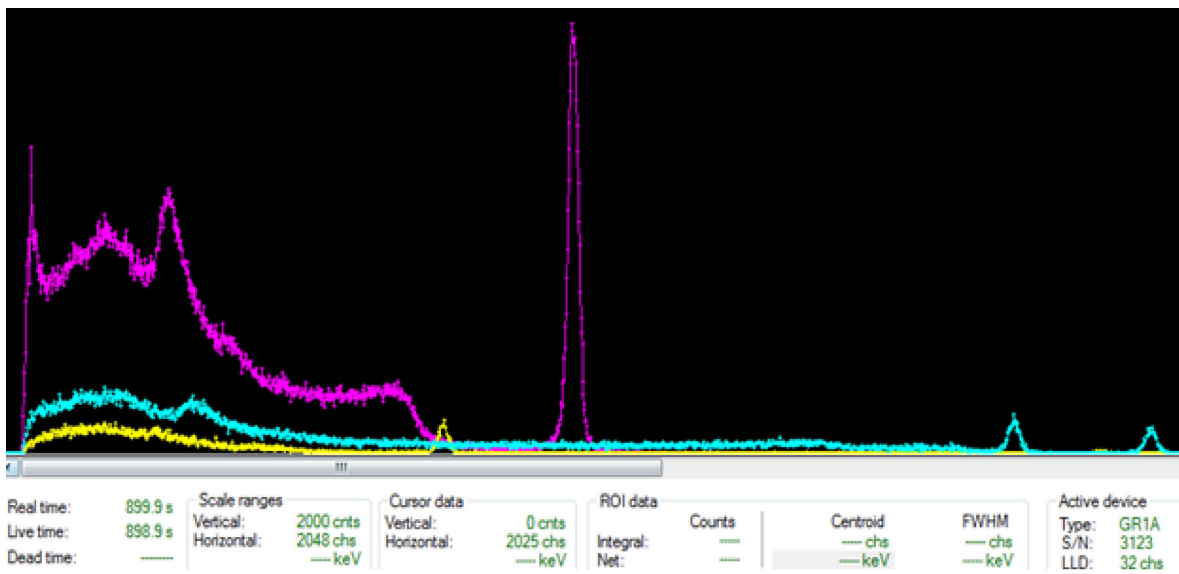
Figure 9: MultiSpect Spectra.

Figure 10: Comparison of Spectra of Multiple Sources using MultiSpect.

The CZT module contains a built-in amplifier, shaper, HV supply, pulse height analyzer, and a baseline restorer. A USB cable was used for powering the CZT module, for transferring the measured detector data to an on-board computer (a Linux based Odroid minicomputer) and for controlling the module. The power consumption of the module is 250 mW; thus, the Odroid's USB port was employed while the Odroid was powered from a battery on the platform. The sensor operates as follows. When radiation comes in contact with the CZT crystal, electron-hole pairs are created, producing an electric signal at the preamplifier. The preamplifier then produces a voltage pulse that is proportional to the energy of the incident radiation. This pulse is converted to a Gaussian waveform by the shaping amplifier. Finally, the 4096-channel multichannel analyzer generates a spectrum stored in an array. The data acquisition time can be set by an operator or by a control algorithm. The spectrum from the CZT module sensor is then sent to the Odroid via USB.

The CZT detectors improves the accuracy and precision of the detection. The UAS allows the operator to fly the UAS at an optimal height from the radiation source. When the radiation source is higher off the ground, the UAS should be flown higher to stop the detector from saturation. When radiation sensors are integrated onto a UAS platform, it represents a low risk of structural damage to the infrastructure and even environment during the operation. Remote sensing has many elements to take into consideration when being studied. The first requirement is the radiation source, which becomes the target of interest. From the source, the radiation comes in contact with the environment and atmosphere. The radiation comes interacts with the detector. From the recording of energy by the sensor takes place including the processing and analysis [49].

ROS [50] was used for fusion of the data sent from multiple sensors connected to the robotic platform (radiation sensors and a GPS sensor). ROS is an open source tool, consisting of libraries

used for robot applications. It allows including a number of independent nodes which communicate to each other, using a publishing and subscribing messages to the topics. ROS running on Odroid was used for onboard analysis of the detector's data. ROS operates through the use of independent nodes that can exchange data between them. A node can publish or subscribe to a topic, or both. Various numerical methods are used for spectral analysis, including wavelet-based techniques [51]. For a robotic platform with limited computational capabilities onboard, an approach that allows for quick spectrum analysis is required. A block diagram of the CZT detector is shown in Figure 11 [52].
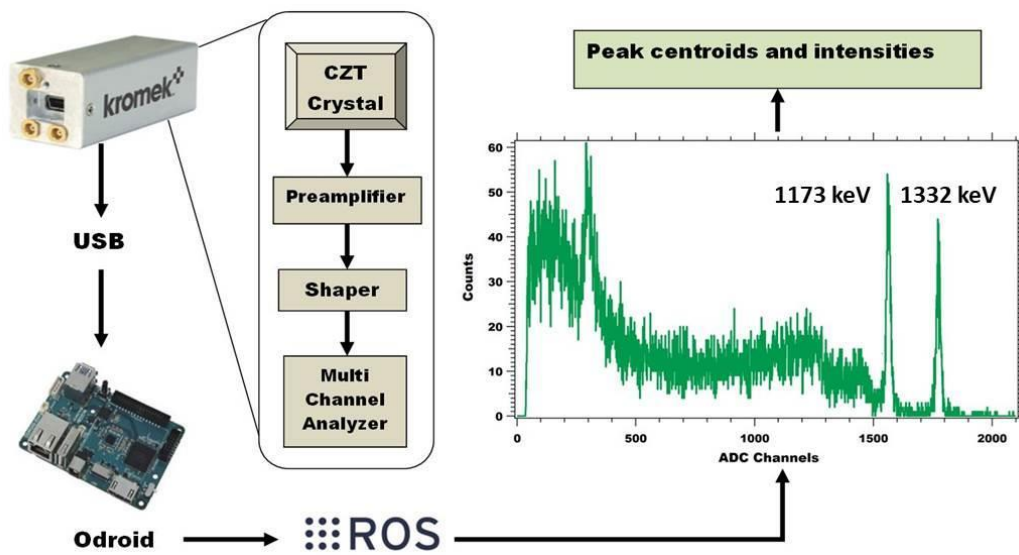

Figure 11: Block Diagram of CZT Detector.

Figure 12 depicts the CZT detector integrated on both the DJI S1000 Octocopter and ClearPath Jackal Unmanned Ground Vehicle. The detector weighs only 49.2 grams, so therefore, it is extremely lightweight and does not affect the payload of the robotic platforms [53].
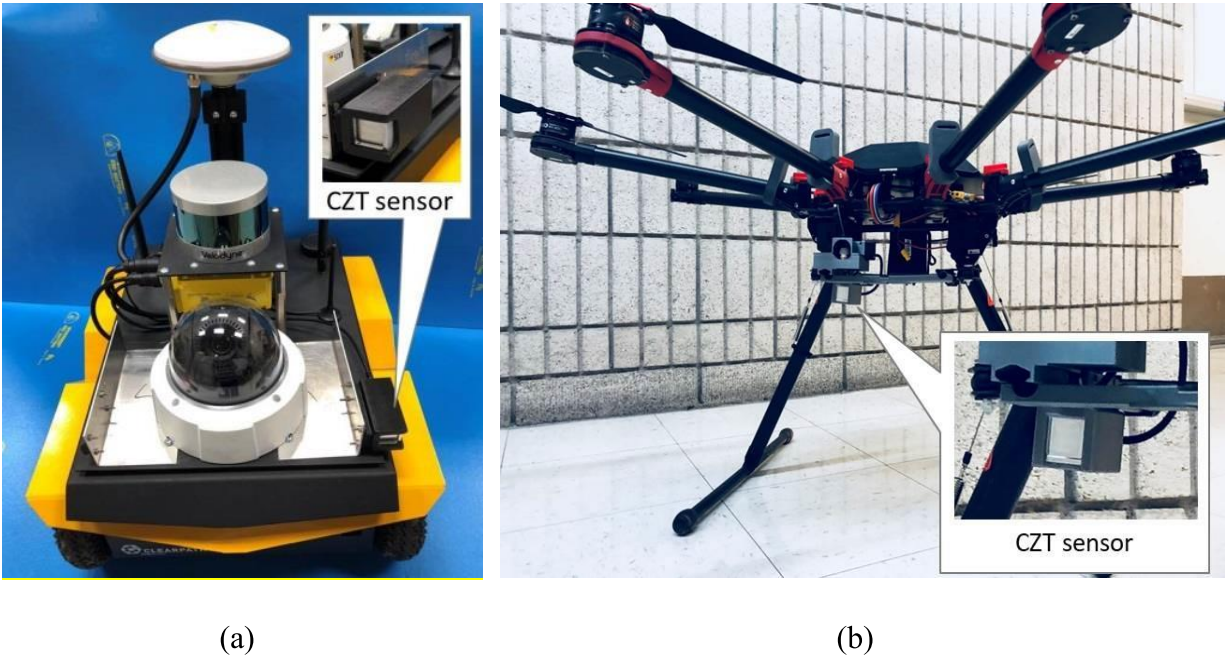
(a)   (b)

Figure 12: The CZT Detector Integrated with (a) UAS Platform, and (b) UGV Platform.

CLYC is a dual-mode scintillator that allows for simultaneous neutron and photon measurements [54, 55]. The scintillation properties of elpasolites enable gamma-ray spectrometry. It produces 20 thousand scintillation photons under the incident gamma rays (per 1 MeV). Neutrons are detected using CLYC via $^6Li(n,\alpha)^3H$ nuclear reaction with the emission of energetic charge particles; 70 thousand scintillation photons are generated in the crystal per one thermal neutron. The excitation of a CLYC crystal caused by a gamma-ray is followed with two decay processes: the CVL decay (1-ns decay constant) and the prompt cerium decay that has 50-ns decay constant. A neutron induced excitation of the CLYC is followed with a (Ce-STE) that has the 1 μs decay constant. Due to the different decay times after neutron and photon excitations, CLYC makes it possible to segregate signals caused by these two radiations using the neutron/photon PSD techniques.

The sensor module was designed using a 2.54-cm diameter, 2.54-cm long cylindrical CLYC crystal coupled with an optical readout - a super bialkali PMT appropriate for the wavelength range of CLYC's scintillation light. A SiPM can be also used for detection of the scintillation. The PMT was equipped with a high voltage generator that was connected to a small-sized emorpho digitizer. The scheme of the CLYC sensor is shown in Figure 13. The components of the sensor were packaged in a plastic housing designed to be easily attached to the UAS. The assembled sensor module is shown in Figure 14.
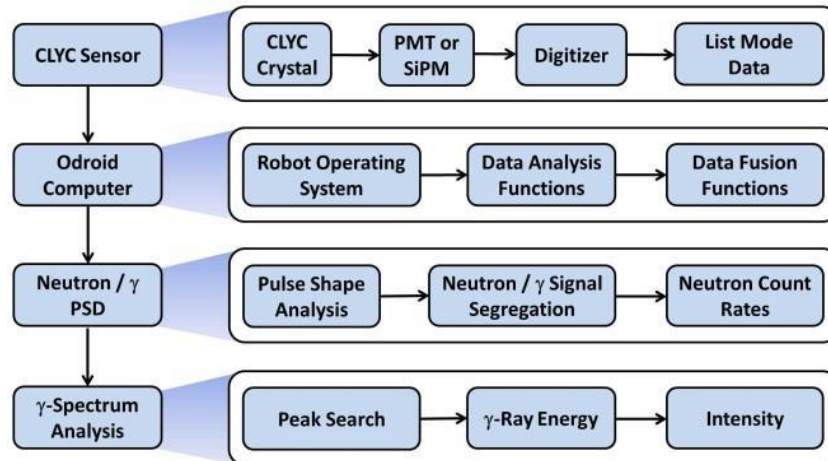

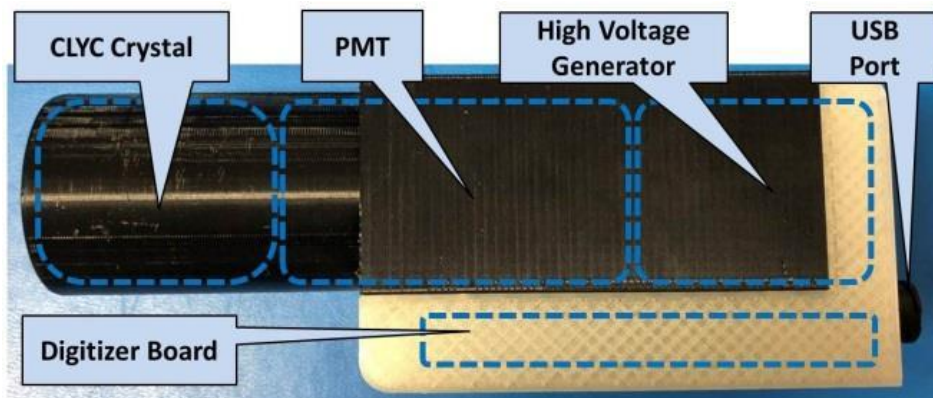**Figure 13:** Block diagram of the CLYC sensor.

Figure 14: CLYC Sensor Module.

After absorption of a CLYC's scintillation photon in the PMT's photocathode, an electron is ejected and directed by the focusing electrode in the direction of a set of dynodes which multiply electrons via the secondary emission. The resultant PMT's current signal is digitized by the emorpho. The recorded waveforms of neutron and photon induced signals of the CLYC sensor are shown in Figure 15. The waveform is processed providing in a list mode the following three values: a timestamp, integral under the signal curve (proportional to the energy of radiation) calculated using the user defined integration time (IT), and integral under the beginning part of the signal assessed using a pre-set partial integration time (PIT). The USB cable was used to connect the digitizer to the UAS computer Odroid-XU4 running Ubuntu Linux and Robot Operating ROS.

The list mode data was used for the neutron/gamma PSD analysis. A PSD value was calculated as a ratio of the areas under the tail part and the front part of the signal. Larger PSD values are associated with the neutron waveforms that exhibit longer tails that the photon waveforms. The PSD value was used to segregate waveforms into two groups (neutron events and photon events).
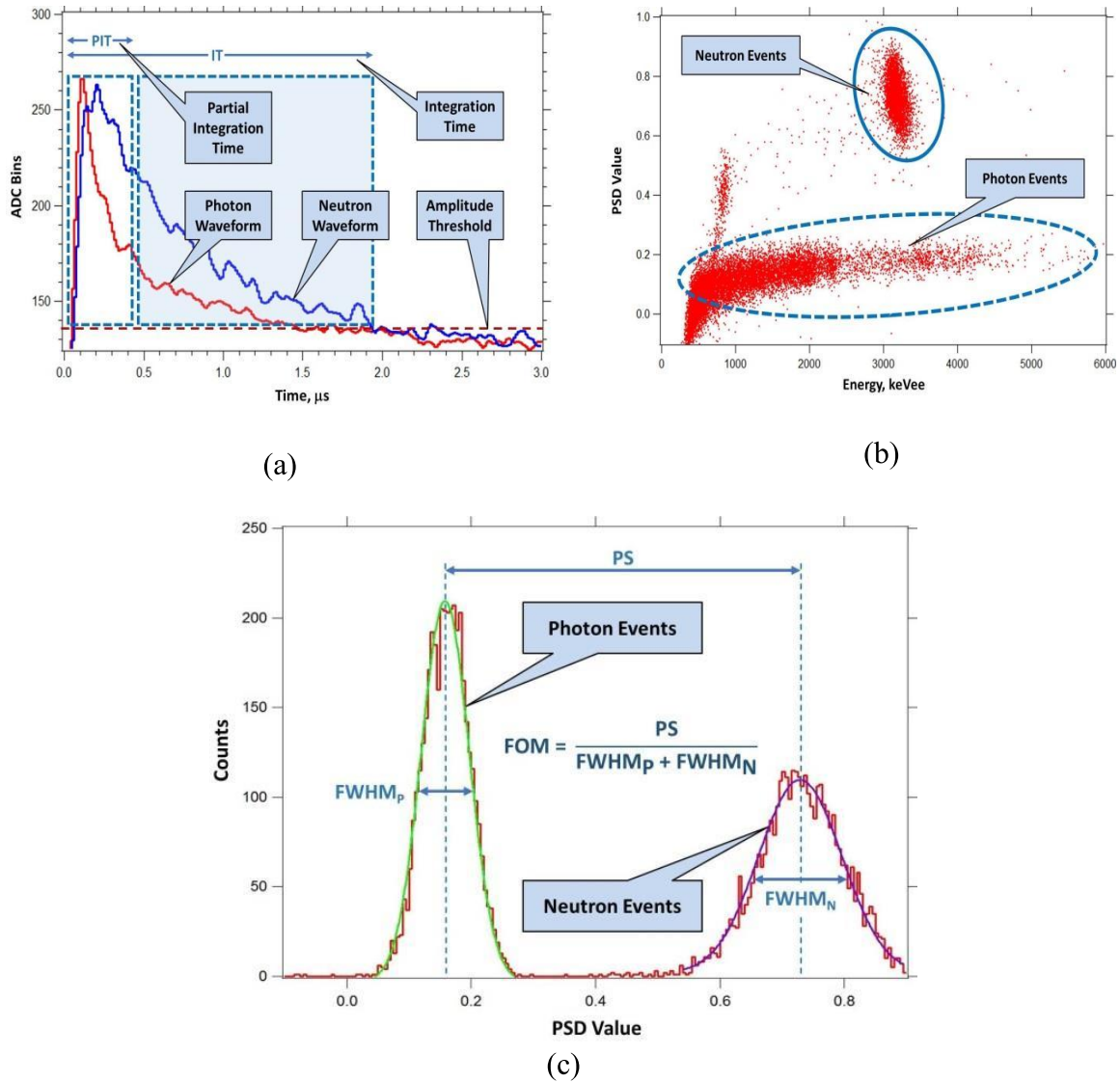
(a)

(b)

(c)

Figure 15: (a) Digitized Waveforms of Neutron and Gamma Ray Induced Signals of the CLYC Sensor; (b) Neutron/Photon PSD Plot; (c) Measurement of the PSD Figure of Merit.

Results of CLYC's neutron/gamma PSD measurements using a PuBe (α,n) source are shown in Figure 15b. The neutron event dots are centered around the 3200 keV value (electron equivalents, keVee). This plot illustrates good separation of neutron and photon events. A PSD figure of merit (FOM) [56] for CLYC was measured using a plot of sensor's counts versus PSD values: the peak separation was divided by the sum of full widths at a half maximum (FWHM)

of neutron and photon peaks yielding a value of 2.3 (Figure 15c). This PSD algorithm was coded using C as a function in ROS.

The gamma-ray signals, segregated from neutron signals, were used to generate a photon energy distribution. The spectrum of photons emitted by a ^{137}Cs source measured using the CLYC sensor is shown in Figure 16. The measured FWHM photon energy resolution of the sensor is 5% at 662 keV, 3.6% at 1173 keV and 3.3% at 1332 keV.
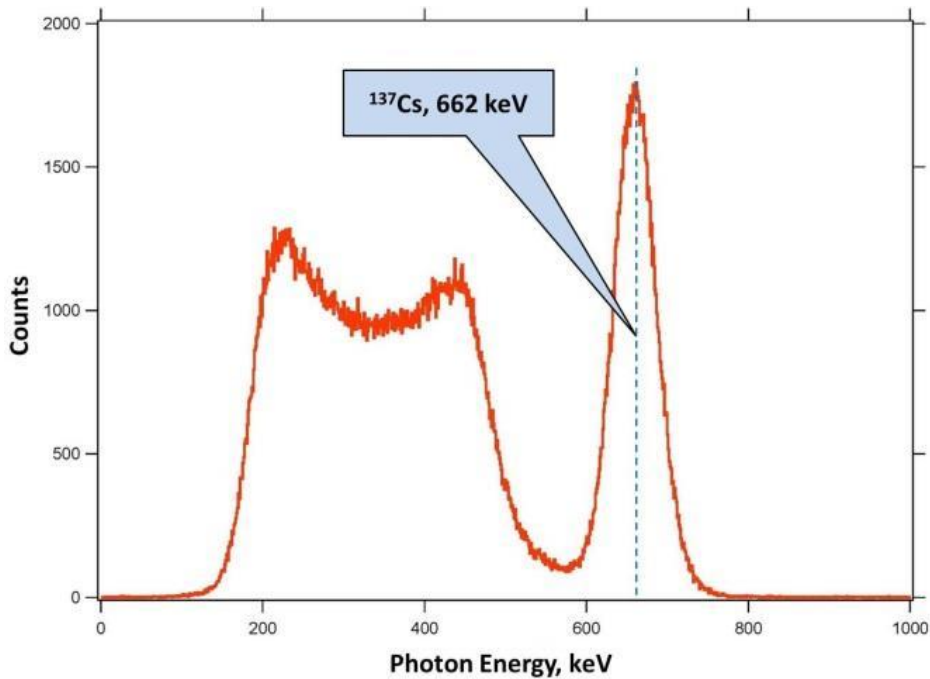

Figure 16: Photon Spectrum of a ^{137}Cs Source Measured using the CLYC Sensor.

3.2 Sensor Integration and Data Fusion using ROS

The sensor integration plays a significant role for the implementation of the robotic platform [57]. There is a need to creating improvements in the automation systems so that challenging of developing new applications can be achieved [58]. Data received from multiple sensors are fused together so that artificial intelligence is accomplished. Artificial intelligence aims on the development and the analysis of algorithms [59] . The robotic system is desired to perform the necessary tasks while interacting and responding with the environment [60]. These robotic systems are able to accomplish many tasks while processing a large number of data. However, the goal is to make is user friendly and to spend the minimal amount of time to configure the device.

The plug-and-play (PnP) concept was used to integrate the radiation sensors onto the UAS and UGV platforms. It allows the operating system to detect and configure internal and external devices. This supports 'hot plugging' of the detectors onto the robotic platform, meaning that the operator does not have to set up component parameters each the sensor is used, which is important in field operations [61]. When the radiation sensor is plugged into the robot's onboard computer via the USB interface, the operating system recognizes the device. The operating system processes and analyzes the sensor and then publishes the results forming a message [62]. This technique also supports 'hot unplugging'. The PnP diagram of sensor operation is shown in Figure 17.
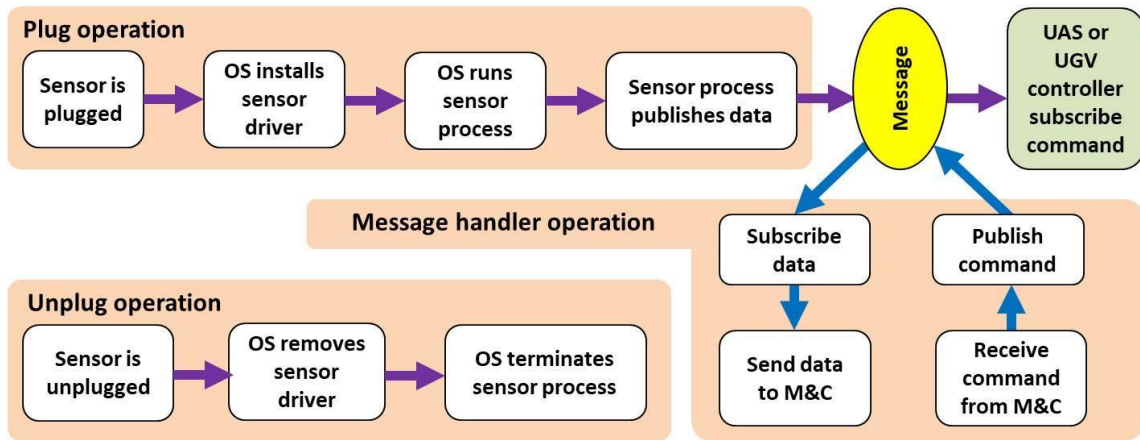
Figure 17: Block diagram of plug-and-play sensor operation

The time and position data were fused with the sensor data processed in ROS. Real-Time-Kinematic (RTK) positioning was used to determine the coordinates the robotic platform. This is a navigation technique improves the precision of position data derived from satellite-based positioning systems. Measurements of the phase of the signal's carrier wave are used and relies on a single reference station to give real-time corrections.

Figure 18 shows the RTK GPS operational block diagram. A base station has a fixed Swift Duro RTK GPS receiver and the known surveyed position coordinates. The correction data to calculate the ionospheric error are transmitted from the base station to each robot's RTK Piksi Multi GPS receiver. The RTK GPS allows raw data measurements up to 20 Hz, and position output up to 10 Hz. The RTK position estimation accuracy is 10 mm horizontally and 15 mm vertically. Experiments using four robotic platforms and a single base station showed the accuracy in position measurements within 1 cm. Such precision of location for multiple robots makes it possible to use this approach in cooperative multi-robot radiation monitoring of wide areas including contour mapping and source search.
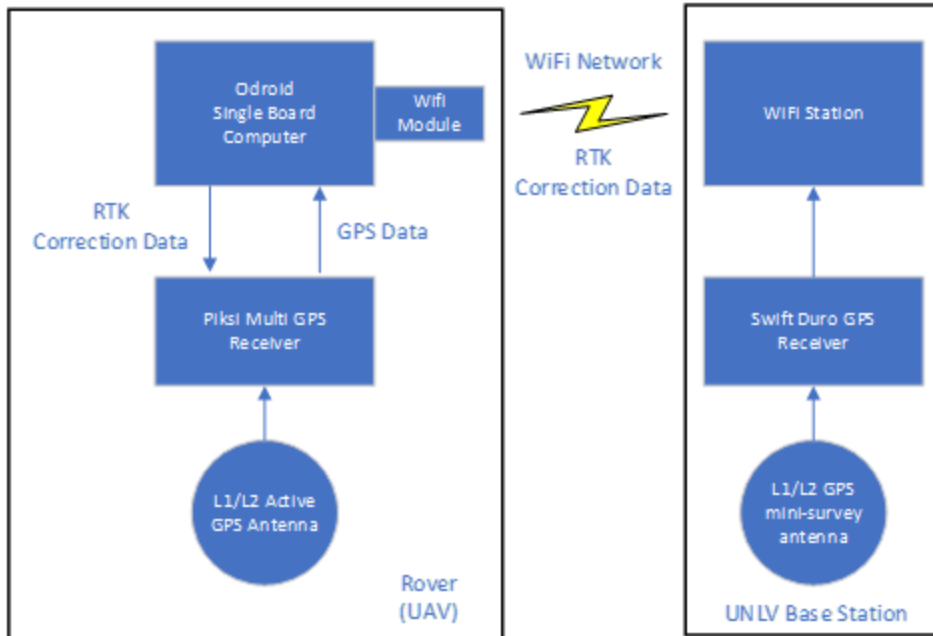
Figure 18: Block diagram of RTK GPS operation.

3.3 Operating System Processes and Analysis of the Sensor Data

The radiation data generated by sensors were time stamped and fused with the UAS's position data based on the RTK GPS positioning technology. The RTK GPS is a navigation technique that enhances the precision of position data derived from satellite-based positioning systems. It is based on measurements of the phase of the signal's carrier wave using a single reference station to provide the real time corrections.

The RTK GPS operational diagram is shown in Figure 19. The base station with surveyed coordinates has a fixed Swift Duro GPS Receiver. The UAS platform carries a single board computer, Piksi Multi GPS Receiver, and L1/L2 GPS antenna. Correction data for ionospheric error calculations was transmitted to the GPS Receiver of the UAS platform from the base station. The RTK GPS has the following characteristics: raw data measurement rates up to 20 Hz, RTK position outputs up to 10 Hz. To test performance of RTK GPS for UAS, the fixed-position base station and four RTK 'rovers' were setup, which is shown in Figure 20.

The RTK GPS antennas of four rovers were equally spaced - 20 cm between the antennas as shown in Figure 21. The Odroid computers were running Ubuntu OS, ROS, and the application programing interface to access GPS data.
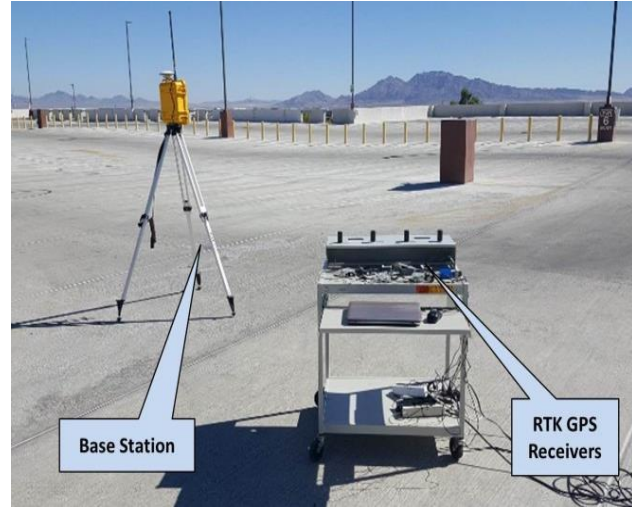
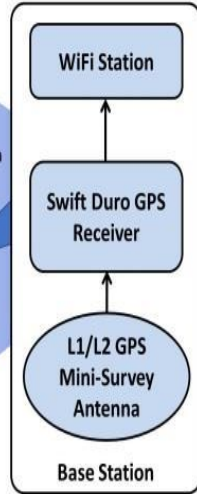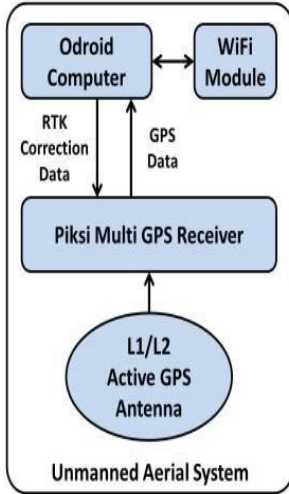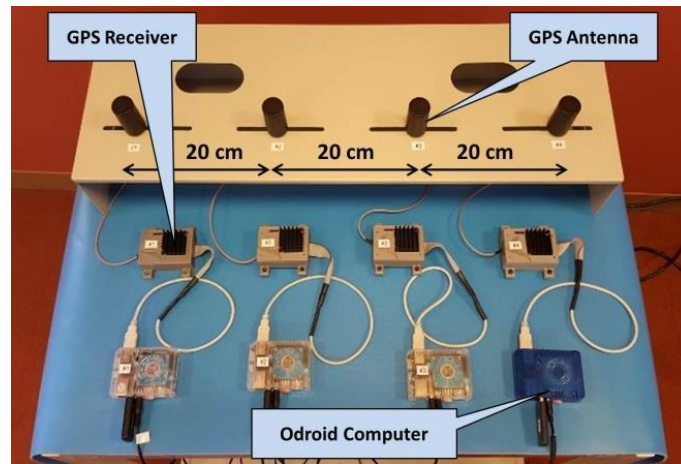**Figure 19**: RTK GPS operational diagram.   **Figure 20:** Position Setup

Figure 21: GPS Antennas and Receivers Connected to Computers.

The measured GPS position data with RTK correction are shown in Table 3: GPS Position Data with RTK (scale: mm). The baseline position is related to coordinates of the base station. Standard deviation σ (68% probability) of the position of four GPS units was estimated as 2.5

mm, and 5.5 mm for the altitude. The UAS position and altitude data measured using the RTK GPS technology with such accuracy enables high fidelity mapping of sensor's radiation data and allows using it in cooperative sensing scenarios that involve multiple UAS.

Table 3: GPS Position Data with RTK (scale: mm).

GPS	Baseline North Average	Baseline East Average	Baseline Altitude Average	Baseline North St. Dev. σ	Baseline East St. Dev. σ	Baseline Altitude St. Dev. σ
1	889.09	5,066.99	981.11	2.59	2.03	5.11
2	833.62	5,252.15	989.15	2.38	2.07	5.02
3	775.81	5,448.22	982.77	2.66	2.66	5.67
4	724.63	5,637.97	988.67	2.36	2.44	5.94

The data fusion function programmed in C within ROS, adds the UAS coordinate and altitude information at the time of measurement to the time stamped CLYC or CZT sensor data. Figure 22 illustrates plug-and-play operation of the CZT sensor. When the sensor is hot plugged via the USB cable in the single board Odroid-XU4 computer running Ubuntu and ROS with custom data analysis and fusion functions, the OS starts the CZT sensor's driver process shown in the process status window. The sensor records the radiation data that are captured. The captured raw data from the CZT sensor for a measurement using a ^{137}Cs gamma source are then plotted to display the gamma-ray spectrum.

The captured raw data are processed using the data analysis functions within ROS, segregating neutron and photon counts (CLYC sensor) and extracting the gamma peak energy and intensity data (CLYC and CZT sensors). Figure 23 illustrates data fusion for the CLYC sensor.
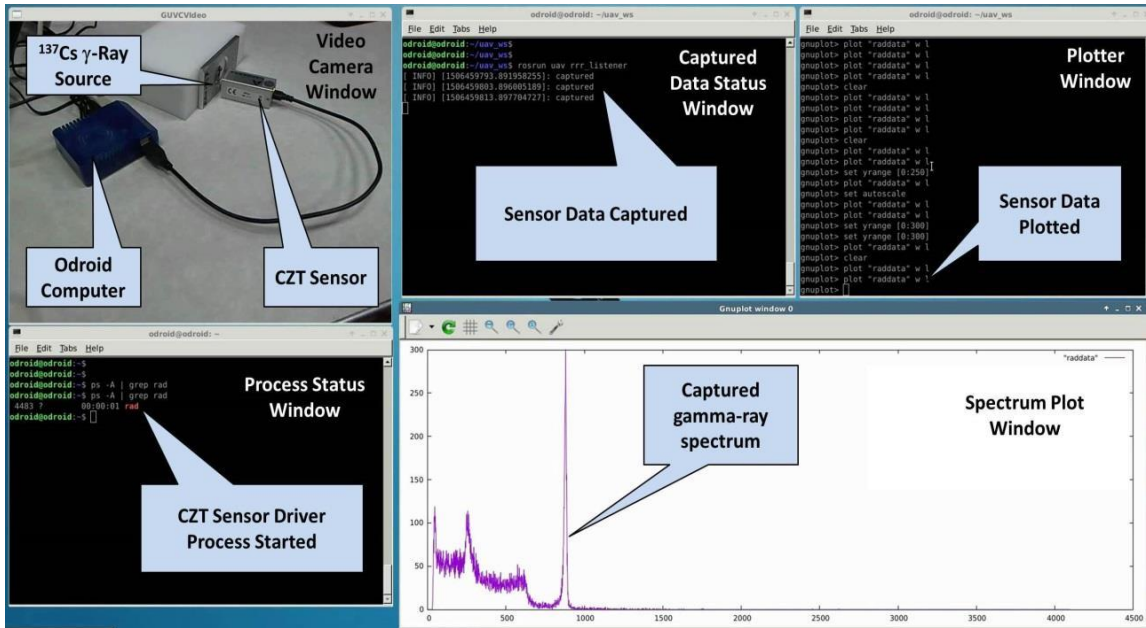
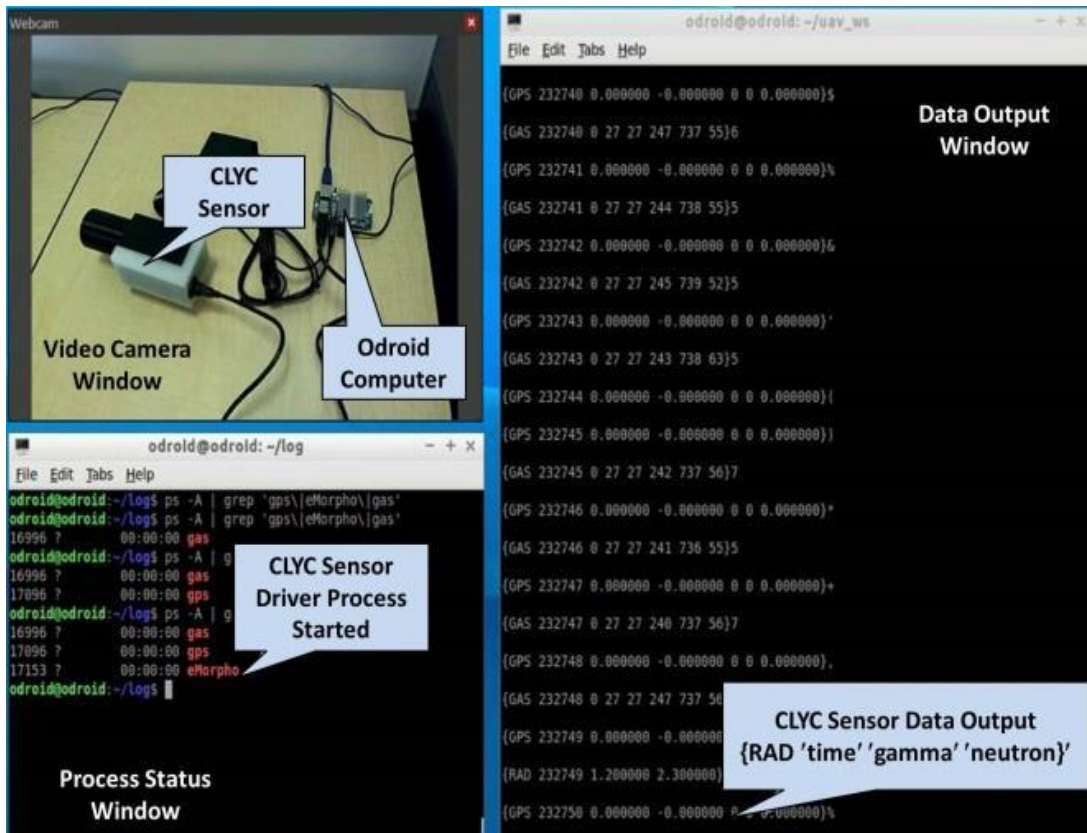**Figure 22:** Testing of Plug-and-Play Operation of the CZT sensor.

Figure 23: CLYC sensor: The Data Fusion.

Chapter 4: Source Search Methods using a Single Platform and Multiple Platforms

4.1 The Mariscotti Technique for the Automatic Identification of Peaks in the Presence of Background

The Mariscotti technique [63] was used for the CZT sensor's data processing. A function written within ROS was used for the automatic identification of photo peaks, with high precision, in the presence of background. $S(x)$ represents the number of counts as the function of the channel number i. The approach is based on the assumption that these peaks are described by a Gaussian and the background is described by a linear function within a small energy range (i.e., several peak widths) shown in Equation 6 [64].

$$S(i) = Gauss(i) + A + B \cdot i \qquad \textbf{Equation 6}$$

where $Gauss(i) = I \cdot exp(-(i - i_0)/(2\sigma^2))$ is a Gaussian (zero if there is no peak) with the intensity I at channel i_0, and σ is associated with full width at half maximum of a peak as $0.4246 \cdot FWHM$. Constants A and B characterize the background. Peaks are found in regions where the second derivative of $S(i)$ is not zero. In the numerical algorithm, the second derivative of $S(i)$ is replaced by the second difference:

$$S''(i) = [y(i + 1) - 2y(i) + y(i - 1)]/h^2 \qquad \textbf{Equation 7}$$

where $y(i)$ represents the counts in channel i and h is the channel width. The measured spectral data carry statistical errors. To resolve weaker peaks in a spectrum with statistical errors, a 'smoothed' form of $S(i)$ was utilized to reduce the standard deviation of the statistical errors. The smoothing was achieved by averaging the $S(i)$ value over m neighboring channels around i, repeated k times. Parameters m and k are set to achieve a desired minimum value of I that can be resolved.

The generalized second difference was programmed as:

$$S_i^{smooth}(k, m) = \sum_j F_{ij}(k, m) S_j \qquad \textbf{Equation 8}$$

where coefficients F_{ij} are weighting factors. Its standard deviation is $\sigma(k, m) = \sqrt{\sum_j F_{ij}^2(k, m) S_j}$. Different spectrums were obtained as shown in Figure 24. The standard deviation is important so that the influence of the statistics is taken into account. The peak centroid was determined as the center of the Gaussian, and then the intensity of the peak was calculated, shown in Figure 25. After the data analysis, the peak's energy values and intensities are used by ROS for further data fusion.
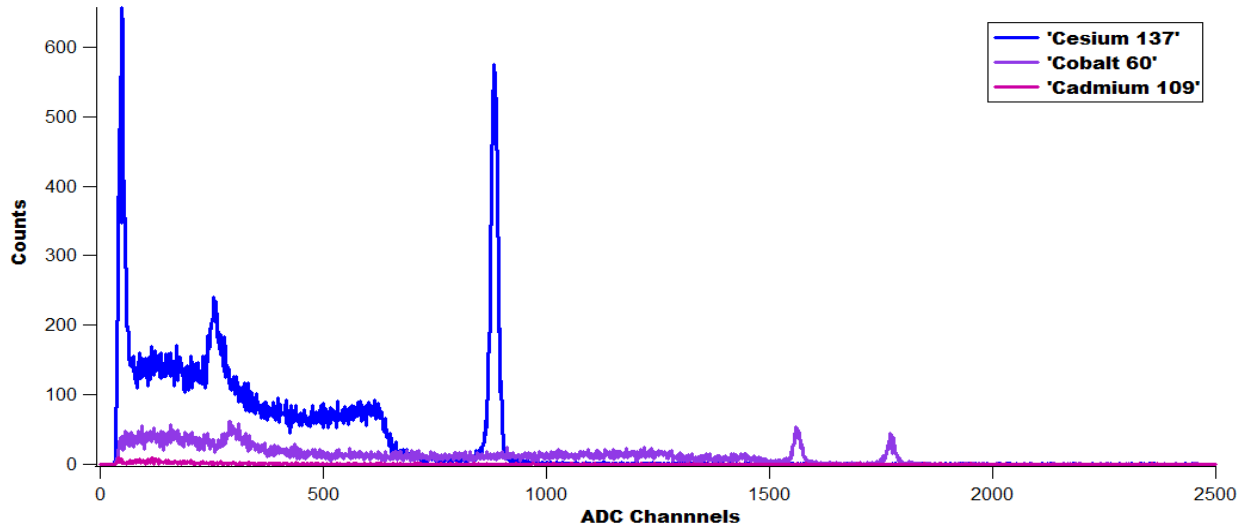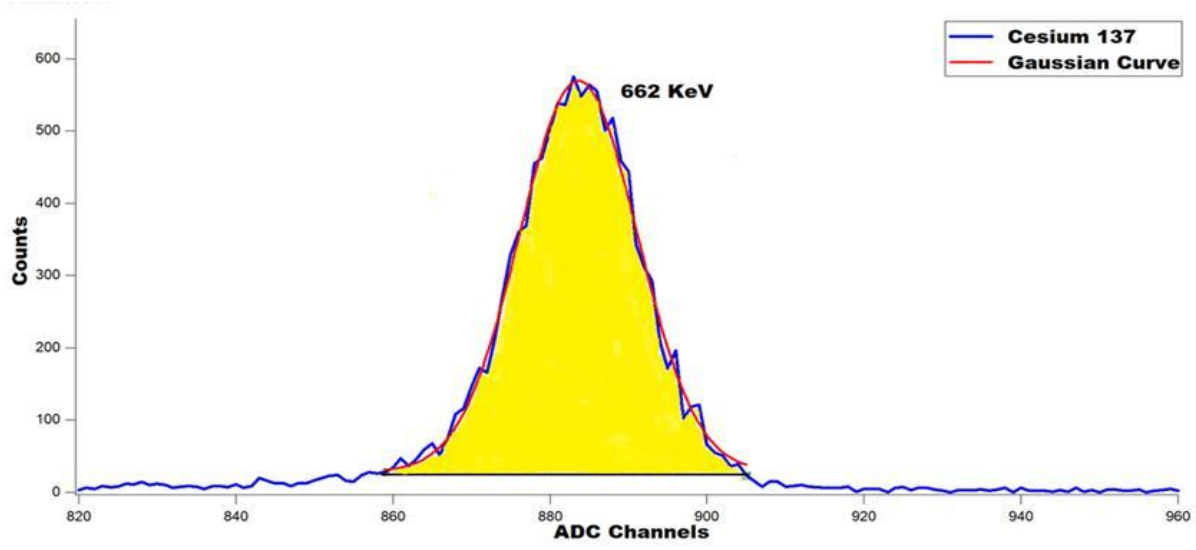

Figure 24: Spectrum Obtained.

Figure 25: Peak Identification.

4.2 Maximum Likelihood Estimation (MLE)

Following the Fukushima Nuclear Power Plant Disaster, there was a need for ubiquitous sensing capability from the release of radioactive materials. The nuclear disaster caused the power plants to lose their ability to cool the spent fuel pools, which had the possibility of the spent fuel release into environment causing radiological contamination across a much wider area. This event called for the understanding that safety is linked with security [65]. Not only for disasters, it is also important for normal plant operations by observing for possible radiological releases into the environment from authorized activities. Therefore, safe control of NPP is vital. In order to address this need, aerial platforms equipped with radiation detectors so that remote radiation sensing capabilities are made possible for the facilities of NPP. Multiple unmanned aerial systems (UAS) with detectors allow for cooperative radiation sensing over a large area. Currently, technologies provide integration options for robotic platforms and allow for high resolution of gamma spectroscopy [66]. Spectral analysis is performed with the on-board computer. The data is supplied with a time stamp and GPS information making it possible to develop algorithms that fuse UAS dynamics with radiation mapping methods. The MLE method was used for the study of cooperative radiation sensing and source localization. The MLE method allows for the construction of a probability density function depending on possible intensity and coordinates of a radiation source in 3D [67].

The MLE technique was utilized to locate the position of a radiation source based on the measured signal's intensities that were time and location stamped. This was achieved by the measurements in three or more locations by a single UAS or simultaneously by multiple UAS located in different points. In the algorithm, the UAS-based detectors were assumed to have an

omnidirectional signal acceptance and the $1/R^2$ signal strength dependence, where R is the distance from the source to the detector [68].

The probability of presence of a source of an unknown intensity was calculated for each point in the scanned space. The points that had the probabilities above the preset value were used to drive the position of the point-like radiation source. The source yield was then evaluated using the MLE for a position of the source and the measured count rates. The probability density function ψ depends on a possible intensity and coordinates of the radiation source (x_s, y_s) is shown in Equation 9.

$$L\left(x_s, y_s, I_0 \mid \{N_i\}_{i=1}^n\right) = \frac{1}{(2\pi)^{n/2} \prod\limits_{i=1}^n \sigma_i} \times \exp\left(-\sum_{i=1}^n \frac{\left(N_i - {I_0}/{R_i^2}\right)^2}{2\sigma_i^2}\right) \qquad \textbf{Equation 9}$$

where $R_i = \sqrt{(x_i - x_s)^2 + (y_i - y_s)^2}$ is the distance from the i-th detector to the source, $\{N_i\}_{i=1}^n$ is the data set of n detector's signals that were recorded with the accuracy σ_i, and I_0 is the intensity of the source. The most likely position of the source along with its intensity can be evaluated by determining the averages of this distribution. The 2nd moment of the normalized likelihood function ψ represents the spatial resolution of the system:

$$\bar{x}_s = \int x_s L\left(x_s, y_s, I_0 \mid \{N_i\}_{i=1}^n\right) dx_s dy_s dI_0$$

$$\bar{x}_s^2 = \int x_s^2 L\left(x_s, y_s, I_0 \mid \{N_i\}_{i=1}^n\right) dx_s dy_s dI_0 \qquad \textbf{Equation 10}$$

The accuracy of the source localization increased with the number of aerial drones or as the number of independent measurements increased using a single UAS in multiple locations. This is illustrated in plots of Figure 26 (a, b, c). Based on this approach, the probability density maps were calculated for a ^{60}Co gamma-ray source that was placed inside the scan space with dimensions of 100×100 units. The source that is marked on the plots with a star was placed at a point (50, 50). Two, three, and five detector measurement locations were used for the MLE estimations within the scan space. The areas on the plots where the radiation source can be found with the maximum probability are shown in red. The MLE algorithm makes it possible to locate multiple sources by treating each source as a separate source using the data of the spectral analysis. Figure 27 illustrates how the predicted position of the source and the localization error depend on the number of measurements in different locations.
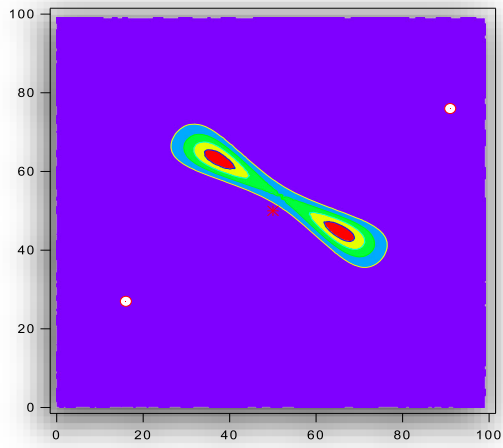
(a)
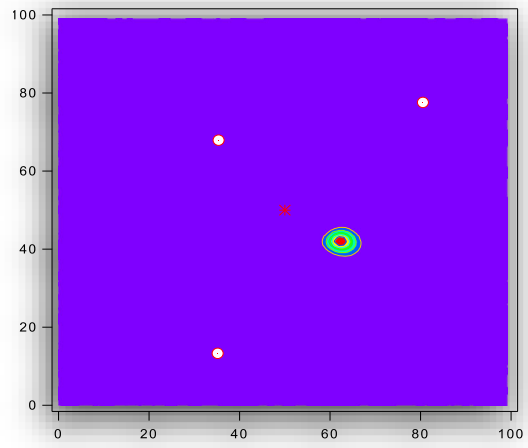
(b)
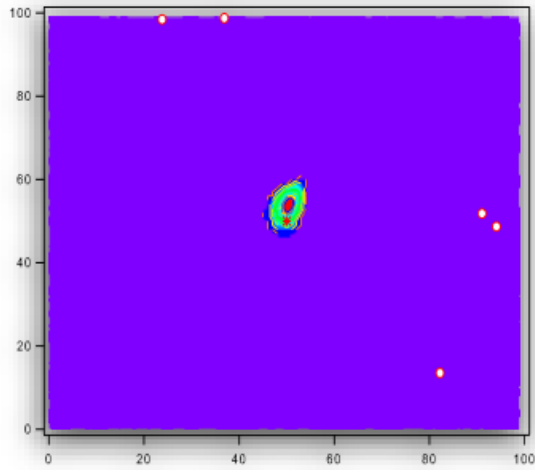
(c)

Figure 26: MLEM Localization of the Radiation Source using (a) Two, (b) Three, and (c) Five Measurement Points. Detectors are Shown in the Scan Space as the White Circles.
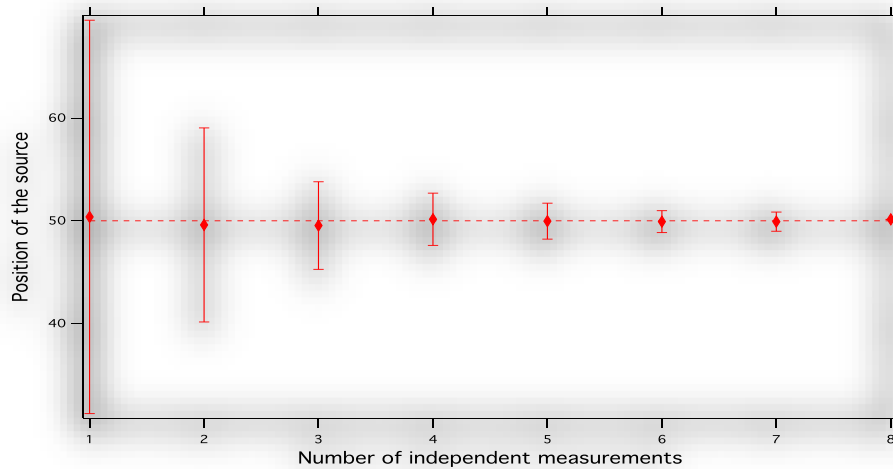
Figure 27: MLE Algorithm: Source Seeking.

The MLE method estimates the parameters by determining what values maximize the likelihood. This method provides the framework for a predictive modeling. It is an analytical maximization procedure. The MLE algorithm was studied in conjunction with the UAS dynamic model [69] enabling feedback control functions based on the measured radiation data. This information also allows planning operations of a robotic platform in the radiation area reducing the dose on its electronics components.

Different scenarios of mapping were studied. A source was placed at 0 x 0 and a single UAS was used. The scenario for 2 sensing points (Figure 28a), 3 sensing point (Figure 28b) , 4 sensing points (Figure 28c), and 5 sensing points (Figure 28d) were evaluated. The way that the MLE estimation method was calculated was by the single UAS going towards the source.
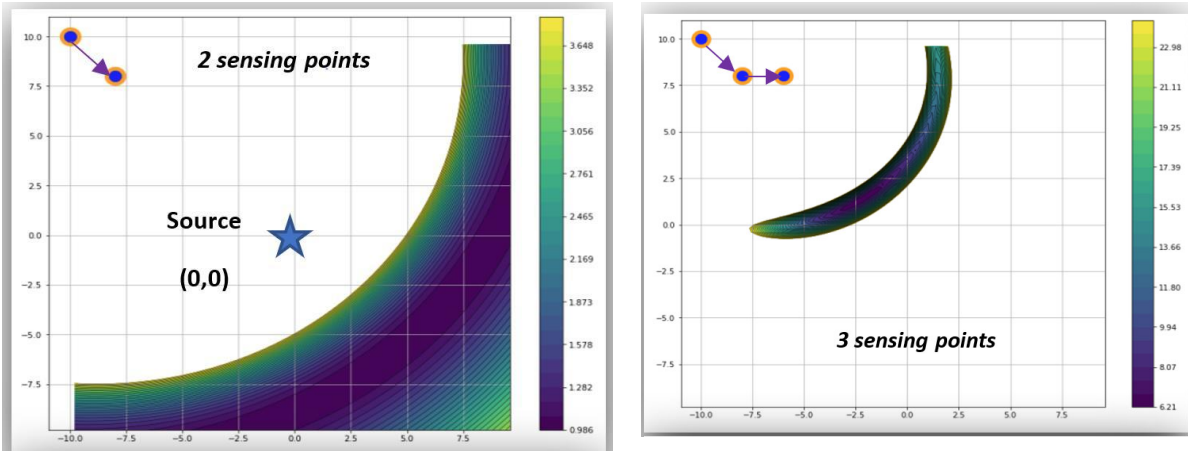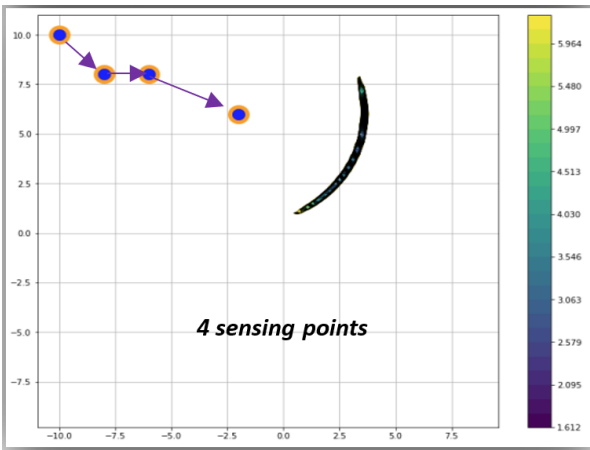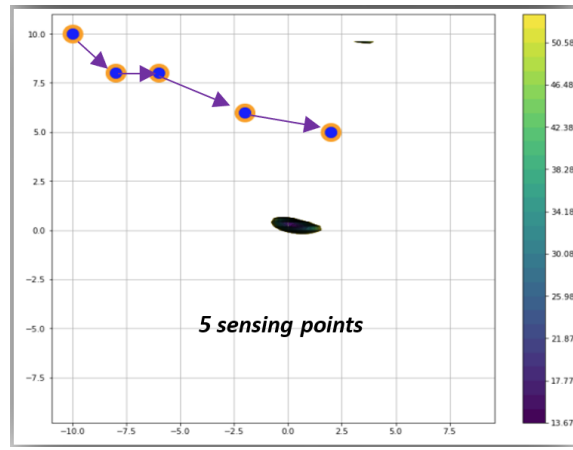
Figure 28: Single UAS Flight (a) 2 Sensing Points, (b) 3 Sensing Points, (c) 4 Sensing Points, (d) 5 sensing Points.

As the number of sensing points increases, the location of the source becomes more evident. Locating the nuclear source is the key purpose of radiation detection. In order to obtain the probable location, the likelihoods are calculated in the alleged areas. This is shown using six sensing points shown in Figure 29.
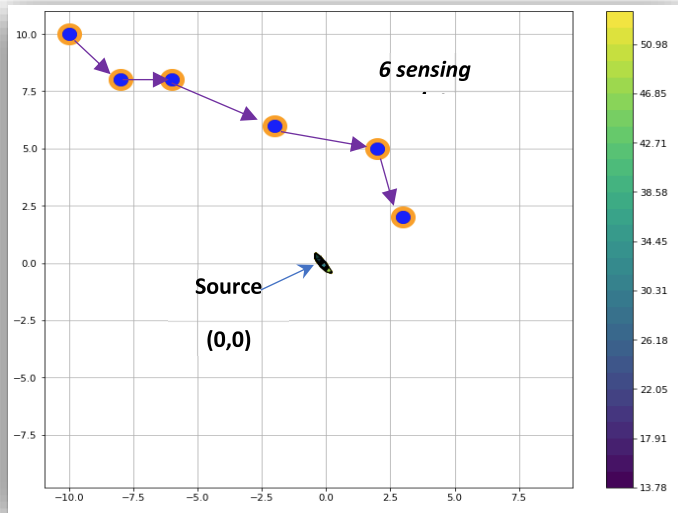
Figure 29: Single UAS Flight using 6 Sensing Points

The next scenario that was evaluated is using multiple UAS platforms. The first case starts with two UAS platforms using just two points in different areas. The source is located at 0 × 0. Then, two sensing points are added in each plot.

Figure 30 shows plots the accuracy of where the source is located increases as the number of individual sensing points is increased.

Figure 30: Two UAS Flight (a) 2 Sensing Points, (b) 4 Sensing Points, (c) 6 sensing Points, (d) 8 Sensing Points, (e) 10 Sensing Points, (f) 12 Sensing Points, (g) 14 Sensing Point

55

Another method that was used was three UAS formation flight. The goal was to improve the precision of the algorithm by obtain the most accurate position information. From the three UAS, it was demonstrated that more accurate results could be obtained. From 3 sensing points, there was a wide area of where the possible source was, shown in Figure 31a. When each of the three UAS has two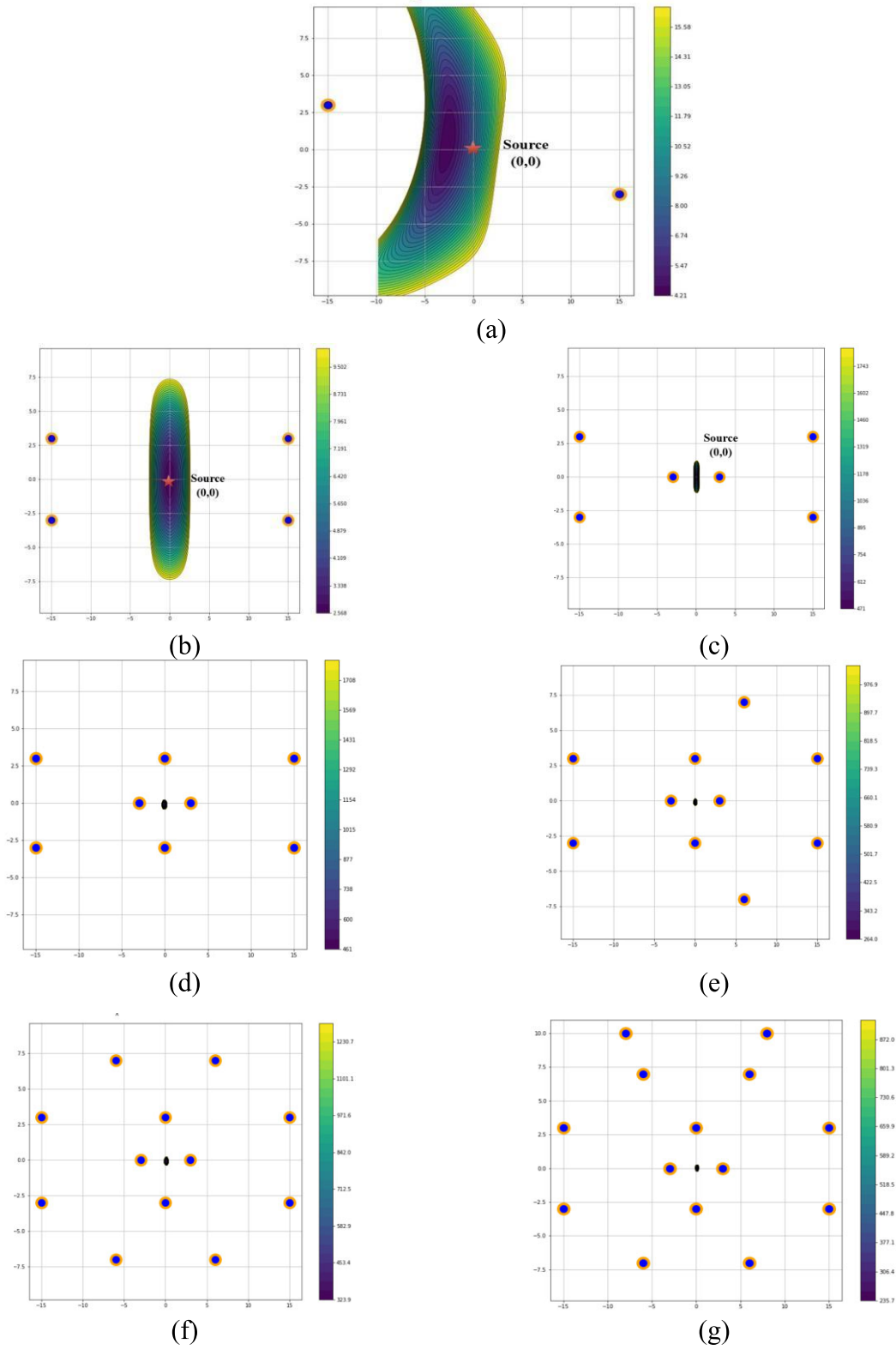 sensing points, with a total of six sensing points, the area of the probable source reduces drastically, shown in Figure 31b. Using a total of nine sensing points, with the UAS going towards the source, the probable area becomes even smaller, shown in Figure 31c. Finally, a pine point of where the actual source is located is shown with 12 sensing point, shown in Figure 31d.

(a)   (b)

(c)   (d)
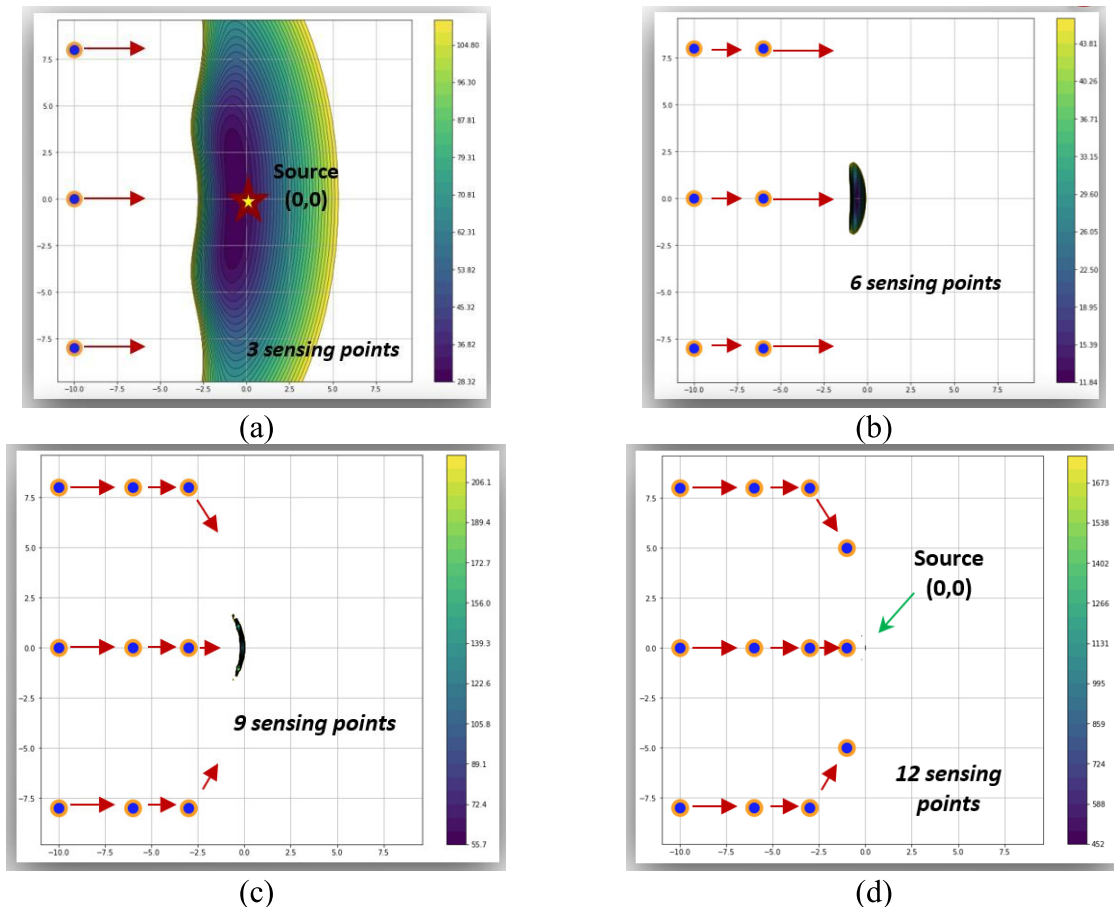
Figure 31: Three UAS Formation Flight (a) 3 Sensing Points, (b) 6 Sensing Points, (c) 9 Sensing Points, (d) 12 Sensing Points

56

Another technique that was studied was a rotation swarm with three UAS. This technique showed to be the most precise. The way that the swarm operated was by forming a circular formation. It was observed that using three sensing points (Figure 32a), the area of the probable source is much better than using a single UAS or three UAS formation flight. Then, using 6 sensing points, the area of the probable source is reduced.

(a)   (b)

Figure 32: Three UAS: Rotating Swarm (a) 3 Sensing Points (b) 6 Sensing Points

4.3 Radiation Field Data

The ability to fly at very low altitude while avoiding collisions with obstacles and terrain in clustered environments such as the NPP is a challenge [70]. Figure 33 shows a schematic diagram of the Westinghouse AP1000 nuclear power plant where three low-altitude UAVs undertake a circular formation flight for radiation contour mapping and source searching.
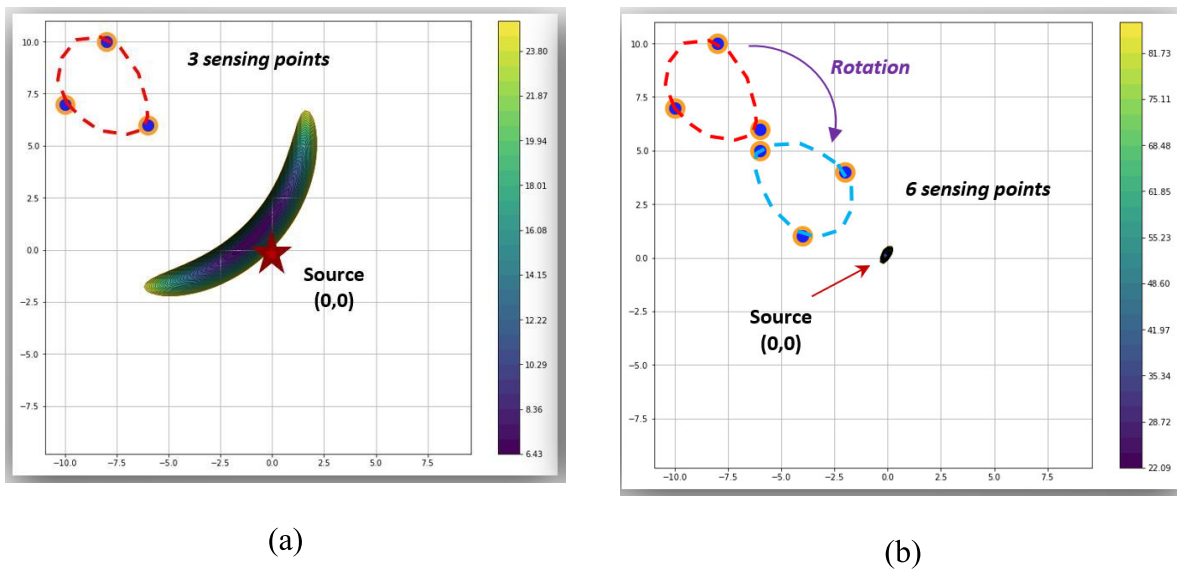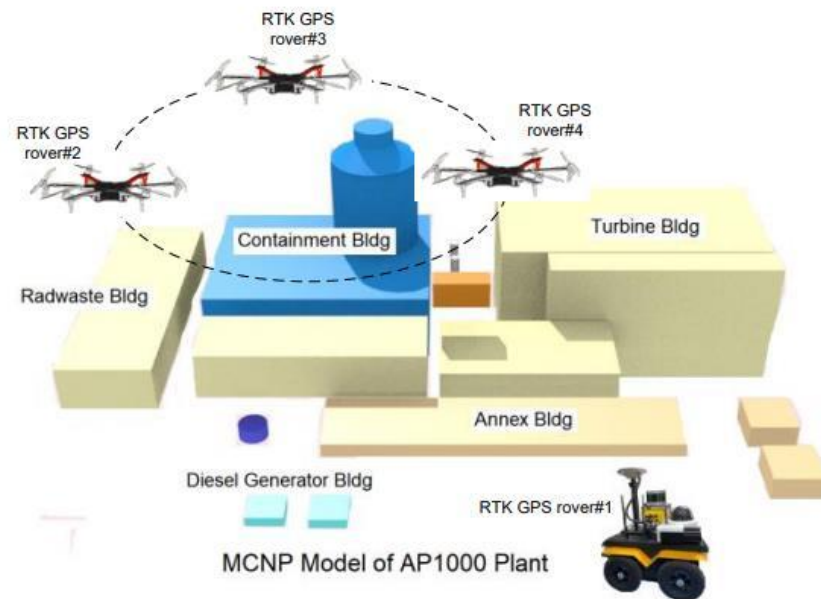

Figure 33: Schematic of Cooperative Operation of UGV and UAVs in the AP1000 NPP

The UGV supports the formation flight of three UAVs from the ground using its high computational power, high-resolution camera, and a 3D scanning Lidar sensor. There are two key roles of the UGV on the ground. One is to measure directly the poses of three UAVs for accurate formation required for radiation mapping. The other is to detect potential obstacles for safely flying at a very low altitude in the clustered environment of the NPP. The Jackal UGV made by Clearpath Robotics shown in Figure 34 is an autonomous ground vehicle equipped with a

Velodyne VLP16 3D laser scanner, an Axis pan-tilt-zoom (PTZ) camera, and the SwiftNAV RTK

GPS. The VLP16 is a 16-beam 3D Lidar. It has a ±15° vertical field of view (FOV) with a 360°

horizontal FOV. Total scans are programmable for reporting at 5 - 20 rotations per second and

the high-definition real time range data allow detecting objects at 100 m away, which can be used

for providing a collision free air space as well as traversability of terrain for a very low altitude

flight of aerial UAS in a nuclear facility. Figure 35 Lidar (Velodyne VLP-16) visualization using

RViz and the Axis PZT Camera Output

Figure 34: Jackal Ground UAS by Clearpath Robotics
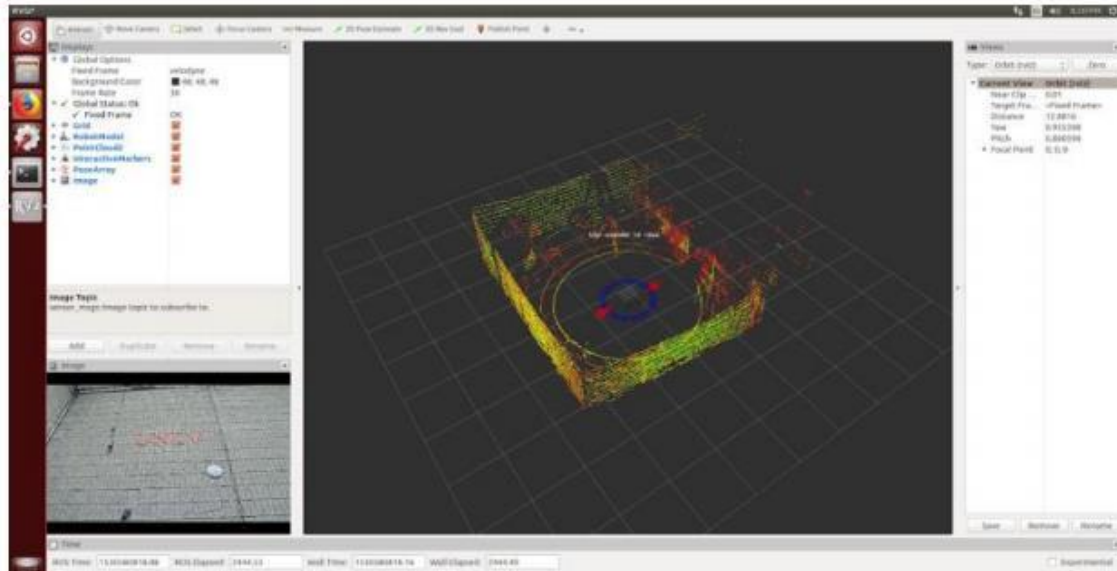
Figure 35: Lidar (Velodyne VLP-16) Visualization using RViz and the Axis PZT Camera Output

In order to keep track of the robotic platforms, Mavelmind robotics GPS [71] was used. This GPS unit contained multiple beacons and a modern. There were two HW variants for the systems, one at 433 MHz and the other at 915 MHz. This system proved a precise, less than 2 cm, location data to the robotic platform. The distance between the beacons could reach up to 50 meters. It has 1-3% location precision to the beans. The beacons were lightweight, which was 59 grams. A diagram of the dashboard is shown in Figure 36, representing the robot management.
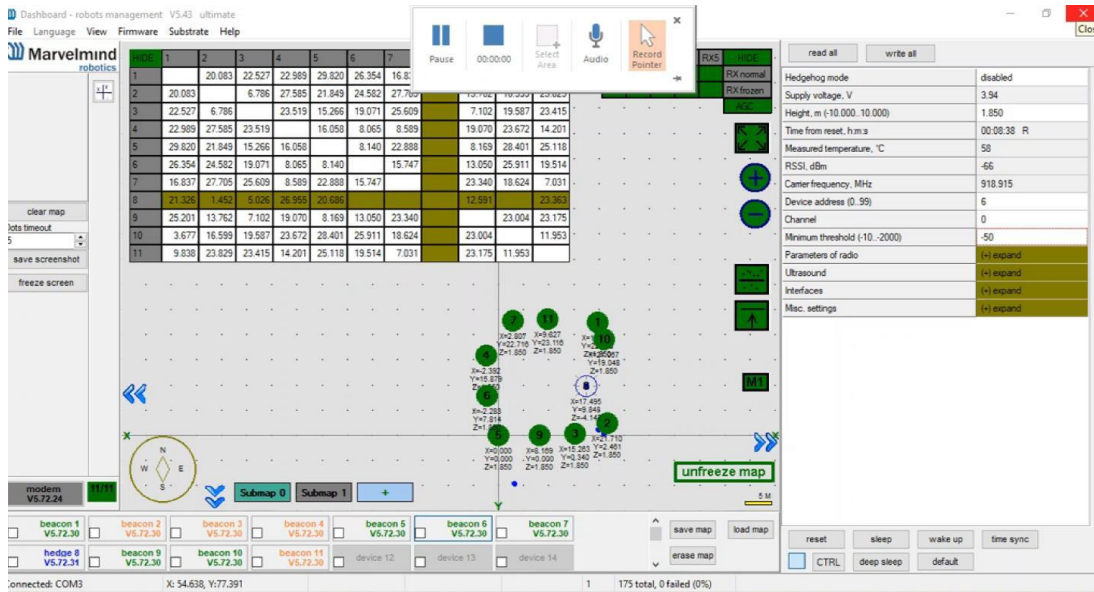
Figure 36: Marvelmind GPS Dashboard

To validate the proposed contour mapping algorithms, the radiation field containing physical obstacles and multiple sources computed with MCNP6 [72] was used. The MCNP6 is a general-purpose code applied to the neutron, photon and electron transport in complex geometry. MCNP6 merges MCNP5 and MCNPX capabilities. An important development in MCNP6 is that it has the ability to transport more particles at an extended energy range [73]. MCNP has the ability to track and tally neutrons and photons within MCNP's constructive solid geometry.

The NPP model was then created in Gazebo. Gazebo is an open source 3D simulator. This simulator makes it possible to test algorithms, design robotics, and train scenarios [74]. The NPP Gazebo model is shown in Figure 37.
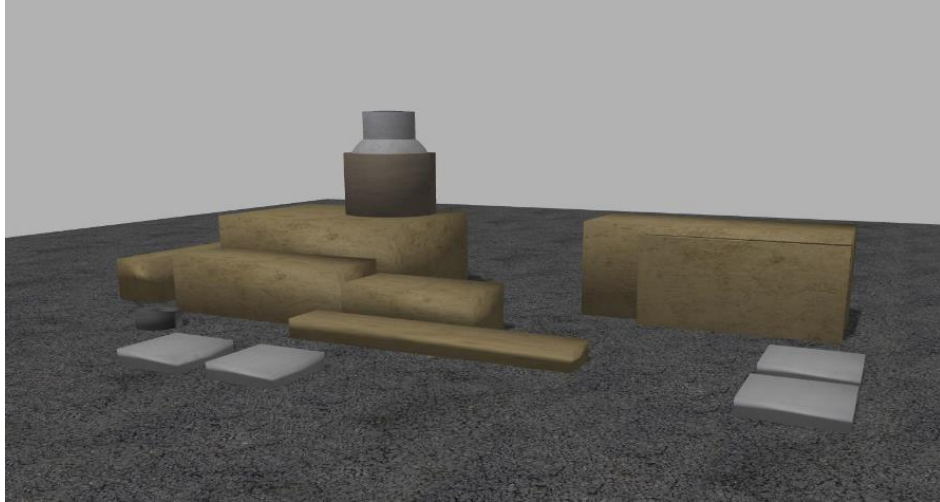
(a)
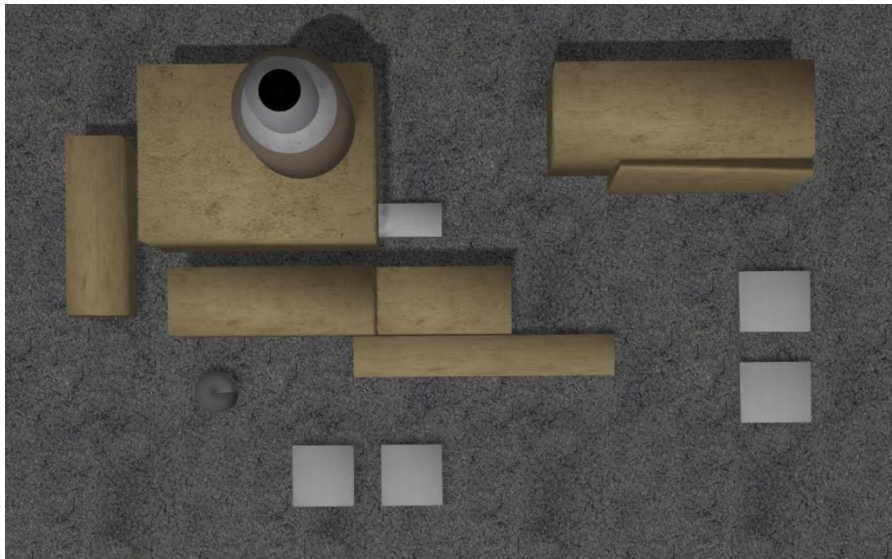
(b)

Figure 37: Gazebo Simulation of NPP.

Data obtained from MCNP6 was plotted. A source was placed onto a building to see what effect it would have. The collided and uncollided data were both plotted. This is shown in Figure 38.
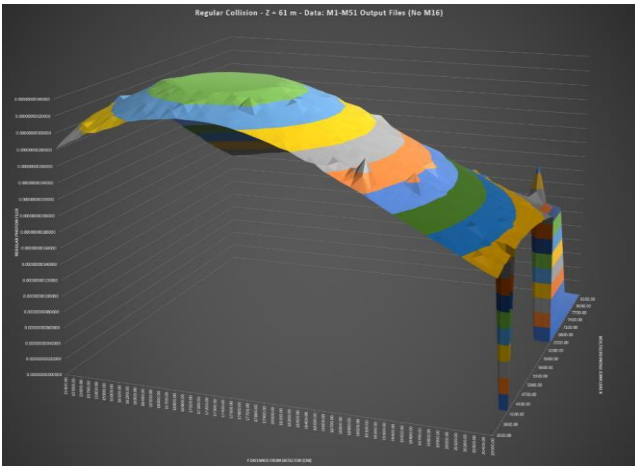
(a)
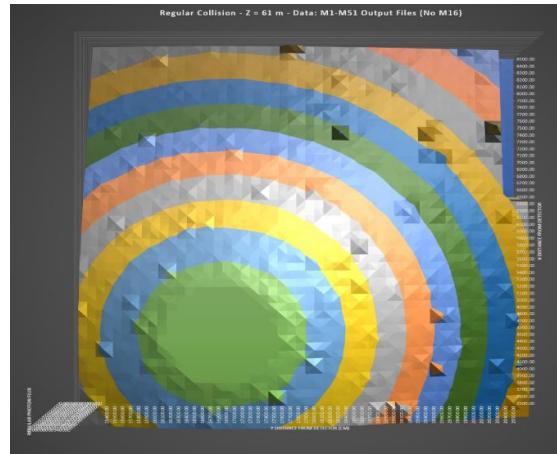
(b)
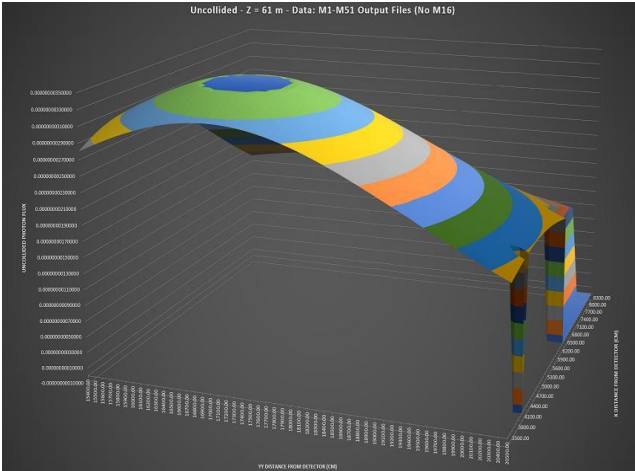
(c))
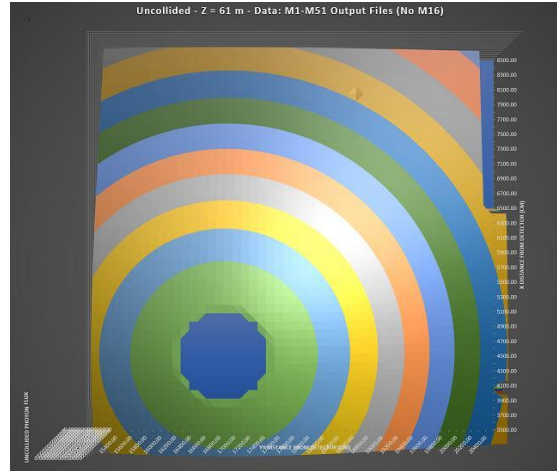
(d)

Figure 38: Radiation Data from NPP; (a) 3D plot of Collided Data, (b) 2D Plot of Collided Data, (c) 3D plot of Uncollided Data, (d) 2D plot of Uncollided Data.

The data for the flux levels at 61 meters above the ground and at the ground. The goal of this plot was to see the contour plots at different heights. It could be seen that the radiation levels are higher above the ground. The contour plot is shown in Figure 39(a). In addition, the area where the radiation level is the highest at 61 meters above the ground is also shown in Figure 39(b).
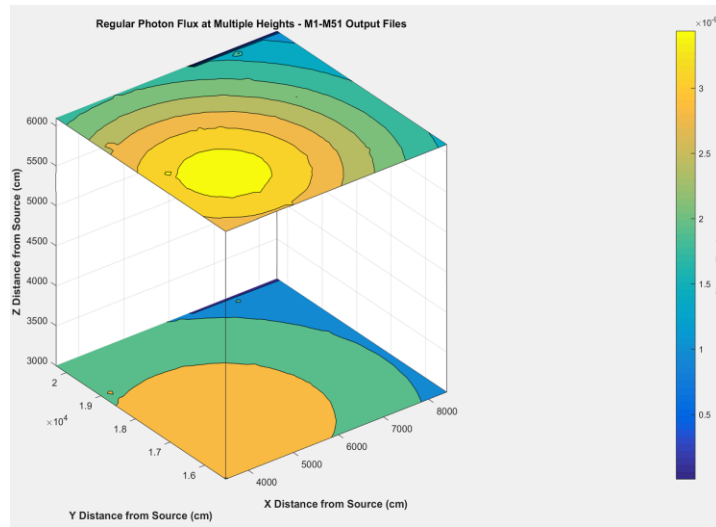
(a)
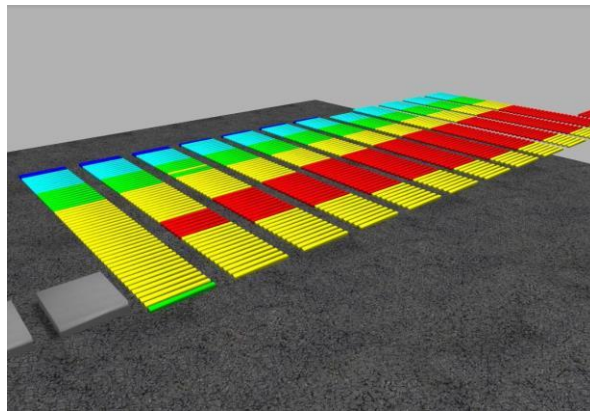
(b)

Figure 39: Plot from Radiation Data obtained from NPP; (a) Photon Flux at Multiple Heights, (b) Plot of 60 meters above the Ground

The radiation data was then inserted into the NPP environment. This is shown Figure 40.
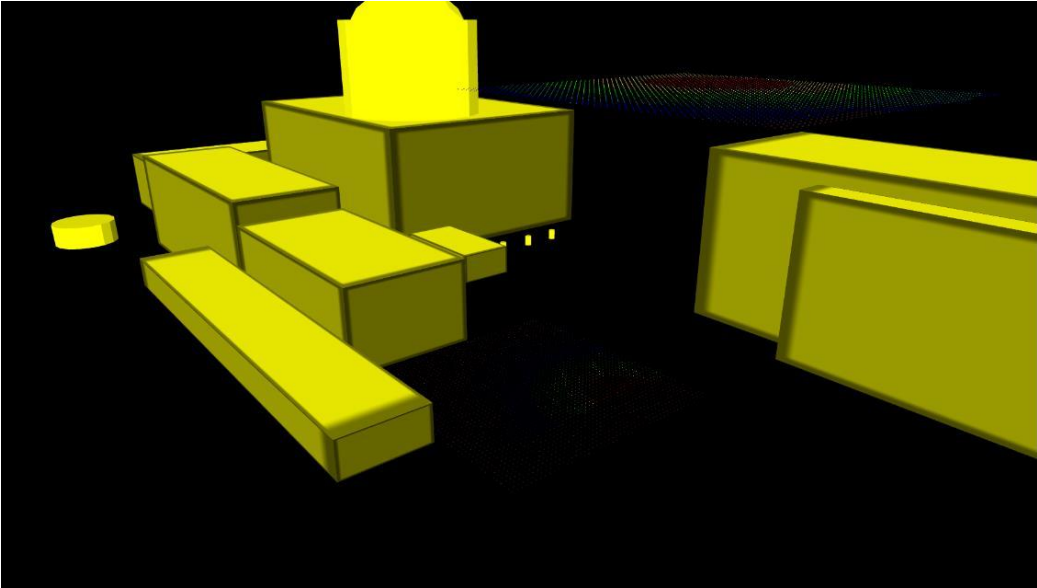
(a)
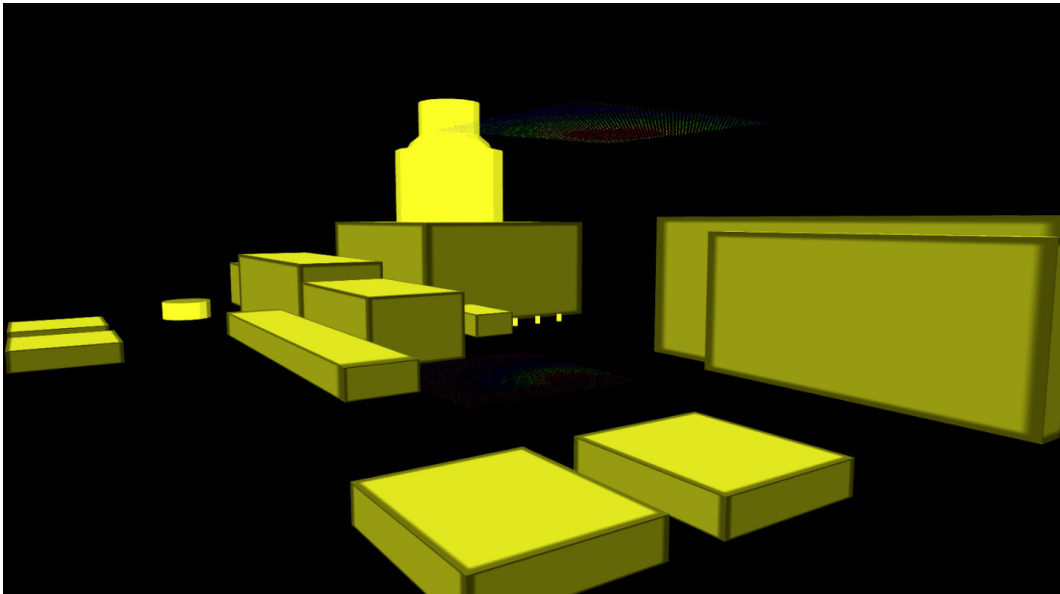
(b)

Figure 40: Radiation Data in the NPP Environment.

The Jackal is simulated into the NPP environment with the odometry navigation. The velocity commands were generated using the information from the Jackal's odometry, laser scanner, and goal pose. The jackal was simulated to create a map. Figure 41 represents the jackal be driven, and a map being recorded.

Figure 41: Jackal's Exploration.

The UGV is also equipped with a portable high-powered Wi-Fi base station which can be used in the field as a long-distance wireless access point for communicating with the Jackal platform. The base station comes with a Real-Time Kinematic (RTK) GPS system. Its global GPS position can be determined with the 1.5 cm accuracy with a NovAtel SMART6 using the phase of the signal's carrier wave and relies on a single reference station to provide real-time corrections to multiple rovers with highly accurate local and global positioning as well as topological precision in remote applications [75]. A long-range base station ensures communications at up to 1 km. Figure 42 and Figure 43 show the sample RTK GPS results for four rover units.
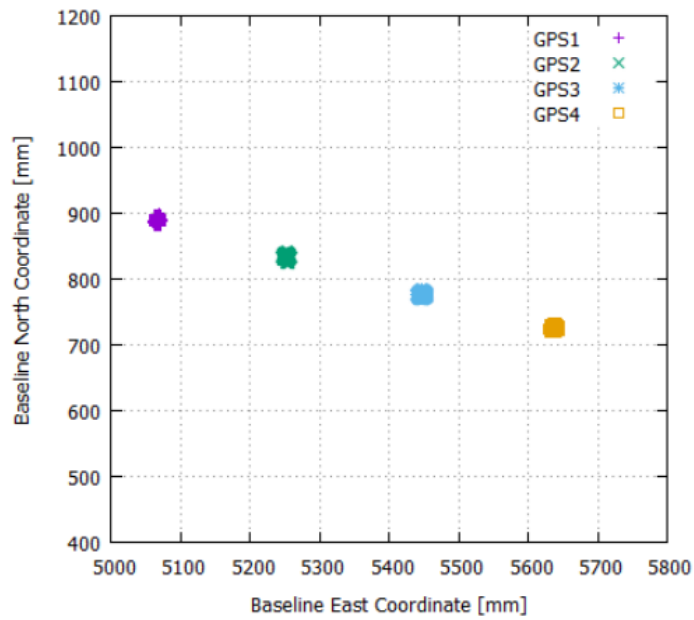
Figure 42: Baseline Coordinates of four RTK enabled GPS units.
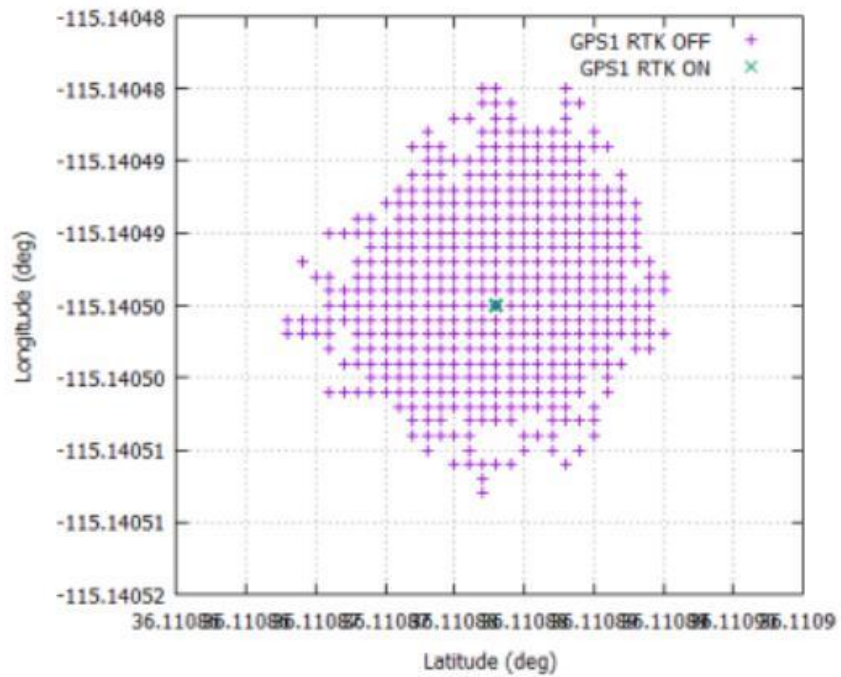
Figure 43: Longitude and Latitude of GPS #1 With and Without the RTK Correction.

67

The Jackal UGV has well-developed simulation and driver support in the ROS and MATLAB. Demonstrations such as this one offer high customizability in shaping terrain, adding obstacles, or modifying the Jackal's performance. Indeed, all sensors can be simulated and customized within the clustered environment such as the NPP. In Figure 44(a), it should the aerial view of the jackal in Gazebo. The Lidar data is shown in red. Figure 44(b), represents the three aerial UAS with a Jackal ground UAV in the simulation environment of the Gazebo.

<table>
<tr><td>(a)</td><td>(b)</td></tr>
</table>
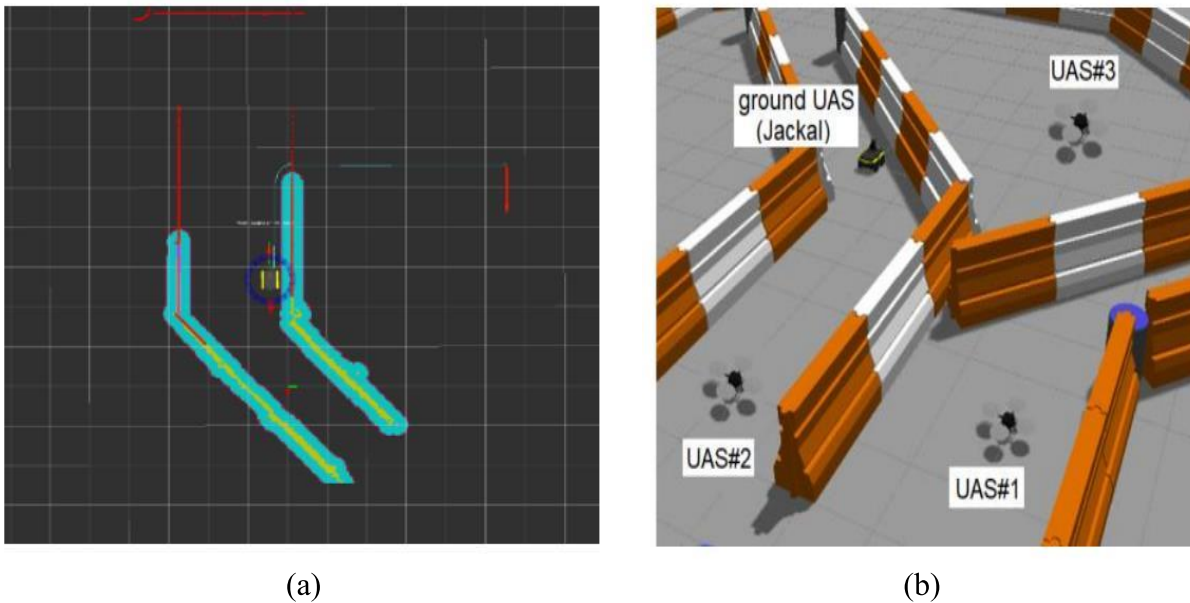
Figure 44: (a) Aerial view of the Jackal in Gazebo; Lidar Data are Visualized in Red, (b) Three Aerial UAS with a Jackal Ground UAS in the Simulation Environment of Gazebo.

Another model was designed in MCNP for comparision to view what effect it would have with multiple sources. This city model had different obstatles for the ground UGV and UAS. The model is shown in Figure 45.
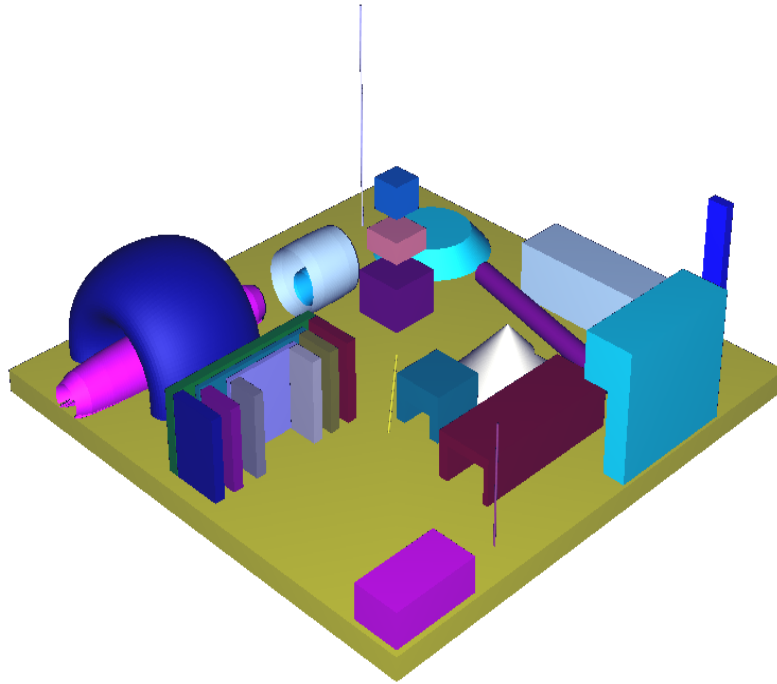
(a)
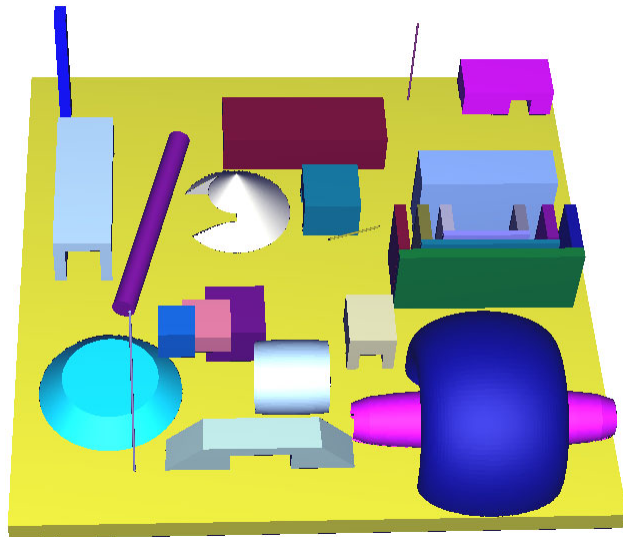
(b)

Figure 45: MCNP City Model

A top view of the city model is also shown in Figure 46. The blue represents the air and the red represents the concrete.
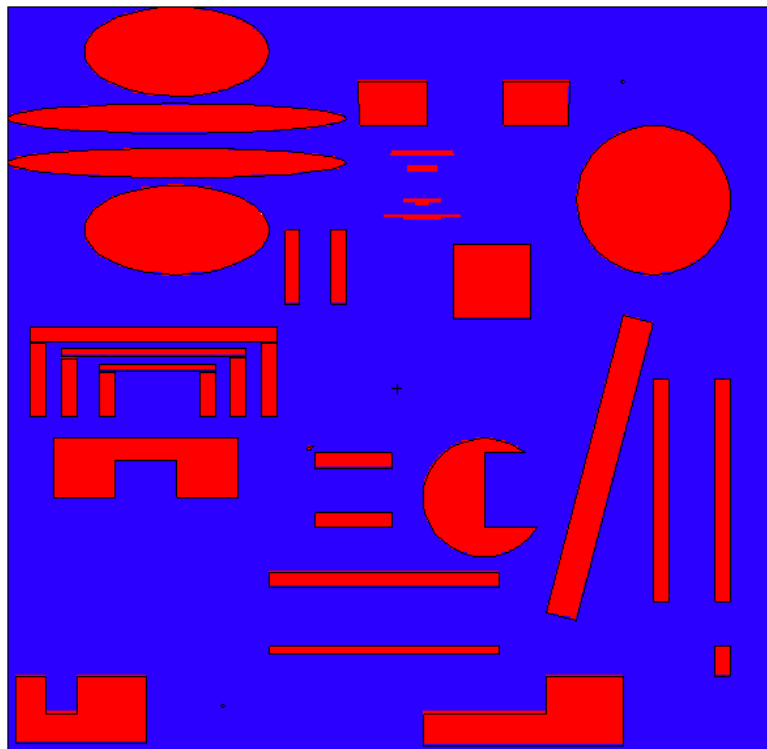
Figure 46: Top View of City Model.

The model was calculated by the z-axis variation. This city model was 50 m $\times$ 50 m $\times$53 m. A more detailed diagram is shown in Figure 47 on how the model was being calculated. The x-axis and y-axis would stay the same and then the z-axis would be varied.
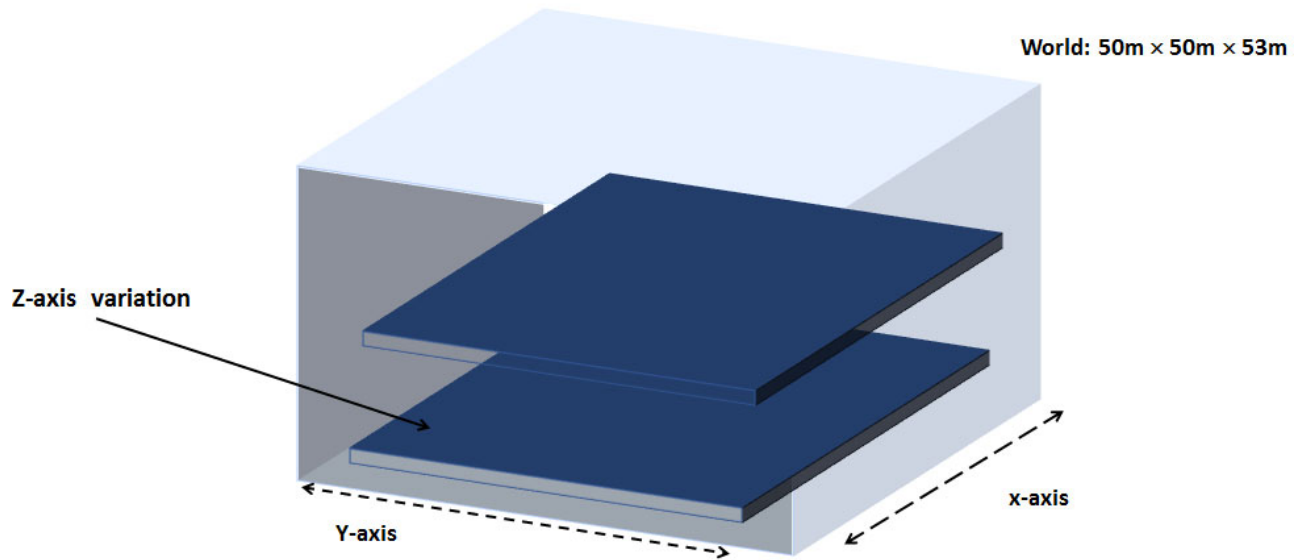
Figure 47: City Model Calculation Diagram.

The data obtained from MCNP shows that the Cobalt 60 source could be differentiated. Figure 48 shows the spectrum obtained. The spectrum contains two peaks, one at 1173 KeV and the other at 1332 KeV, corresponding to Cobalt 60.
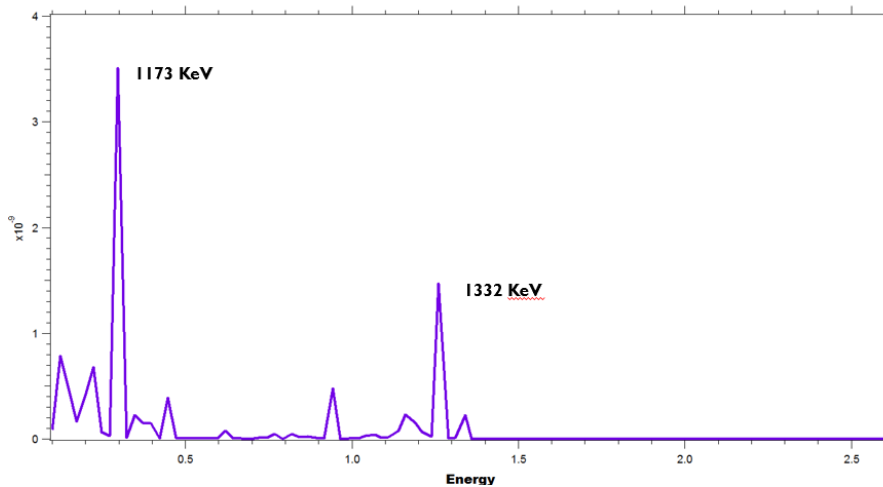
Figure 48: Cobalt 60 Spectrum Obtained from MCNP.

In order to see what affect the source would have on the rest of the city model, the levels of the flux were recorded in different areas. This is shown in Figure 49. The source was placed in a bulding. It could be seen that the location of the source is where the peaks of the Cobalt-60 source is more defined. As the location gets further away from the source, the levels of the flux decrease. In order to anaylsis the city model further, a Cesium-137 source was placed in the model. It could be seen in Figure 50 that the is one peak when the location is near the source. As it gets further away, the levels of the flux decrease.
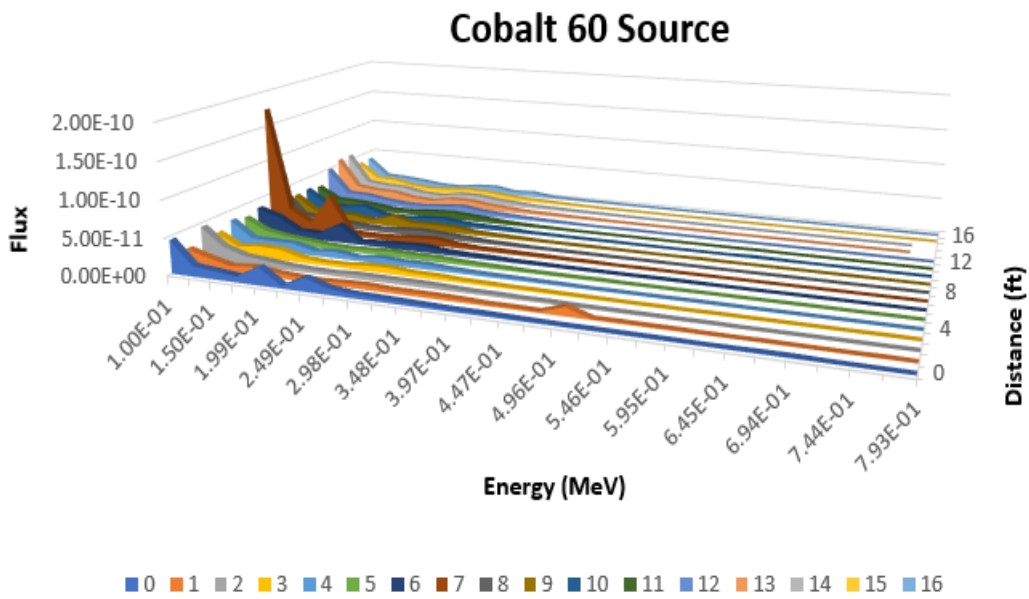
Figure 49: Cobalt 60 Source in City Model.
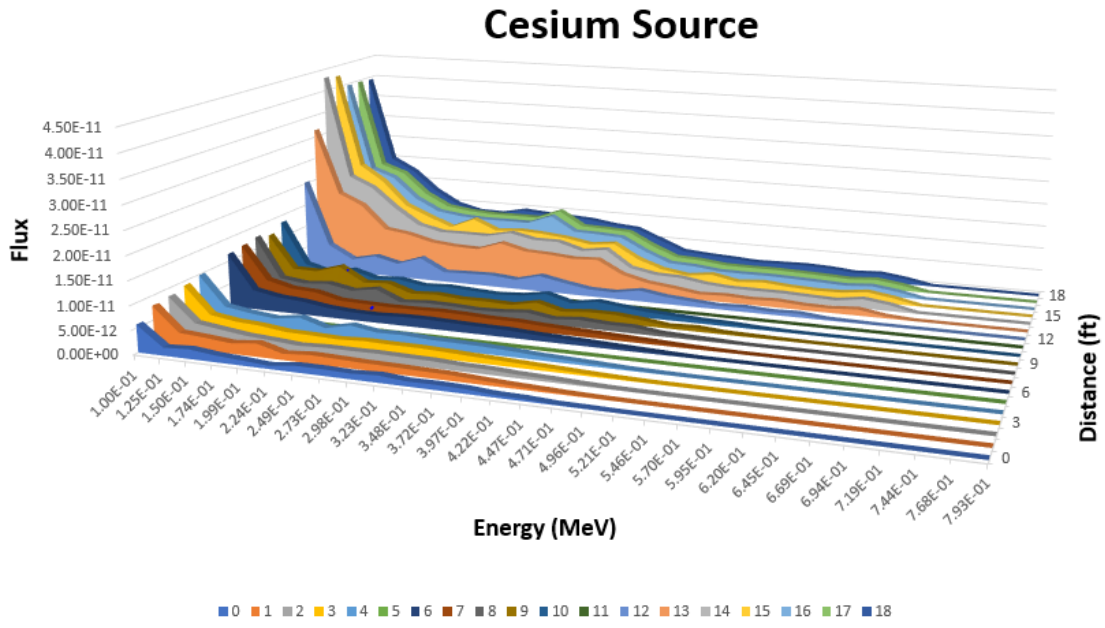
Figure 50: Cesium Source in City Model.

Chapter 5: Radiation Damage

5.1 DPA in Electronic Components of the Robotic Platform

Radiation measurements are necessary for a routine monitoring of nuclear facilities [76, 77] and during emergencies such as the Fukushima Daiichi nuclear power plant accident. Radiation monitoring provides necessary information regarding radiation doses in the environment, minimizing the risk of exposure to the workers or to the public [78]. Gamma-ray and neutron measurements can provide a safe boundary of a contaminated area for human exploration in case of a nuclear emergency. Robotic platforms are utilized to carry radiation sensors to allow for remote sensing and sampling [79], and offer a solution for the waste cleanup tasks [80].

However, the robots might be exposed to high levels of radiation which limits their operational time. The irradiation causes microscopic defects in devices and components of the platform, especially electronic parts, leading to loops, voids, defects, or even to the termination of the robot operation. The goal is to achieve completion of the scheduled tasks during the operational time of the robot. In order to allow this, the electronic components should be shielded, and radiation hardened. It may lead to an increase of the platform's weight and a decrease of the robot's operational capabilities. Therefore, the prediction of radiation damage in electronic components of the robotic platform is important.

Radiation damage in materials is characterized by the DPA. DPA is the number of atoms displaced from their lattice sites. The Monte Carlo code FLUKA [81] was used to calculate the DPA in the robot's electronic components. Two robotic platforms were used in the study: the PhantomX hexapod (a ground platform) and the DJI S1000+ octocopter (an aerial platform). Both platforms carry a CZT radiation detector [82] and a video camera. The packaging of electronic

74

parts and the shielding design were determined so that the robot's lifetime under high levels of radiation could be increased while keeping the optimal payload.

The PhantomX AX Metal Hexapod MK-III by Interbotix Labs, an open platform of a 'spider robot' with a top deck that enables attachment of sensors and cameras, was utilized. It carries a 1 cm^3 CZT detector and a video camera that operates with an OmniVision OV5640 CMOS image sensor with a focal length of 3.6 mm. The robot's components are shown in Figure 51a. This hexapod was chosen because of its idle mobility, robustness, and versatility. It controls six legs with three degrees of freedom for each leg and achieves superior mobility. This robot is able to adjust when the legs begin to fail. The hexapod's motion testing in a desert terrain is illustrated in Figure 51b.

There are 18 AX-18A Dynamixel actuators in the hexapod platform. The actuators are connecting joints of the robot enabling their versatile movements. It has the capability to track the speed, strength, position, and voltage. The microcontroller supports the position control. The Dynamixel actuator specifications are shown in Table 4. Each leg of the robot contains three actuators. The ArbotiX-M Robocontroller manages the actuators, thus controlling the movement and direction of the robot. The actuators have the ability to move each of the legs separately. The robocontroller contains the AVR microcontroller, 2.4 GHz Xbees, dual motor drivers, and 3 pin servo headers for the input and output. The hexapod's leg and the ArbotiX-M Robocontroller are shown in Figure 52a and Figure 52c, respectively.
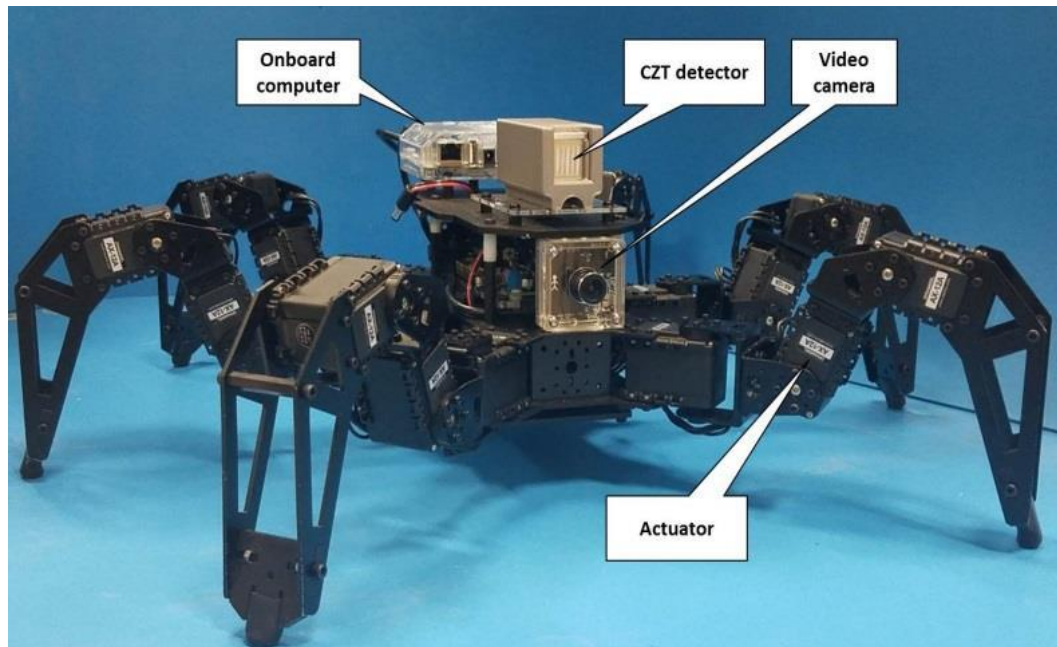
(a)

(b)

Figure 51 PhantomX AX Hexapod MK-III: (a) Components of the Robot; (b) Testing in a Desert Terrain.

Table 4: Dynamixel Actuators Specifications

Description	Data
Operating Voltage	12 V
Stall Torque	15.3 kg·cm
Weight	55 g
Size	32 mm × 50 mm × 40 mm
Resolution	0.29°
Operating Angle	300° or continuous turn
Internal Operating Temperature	-5°C to ~ 70°C
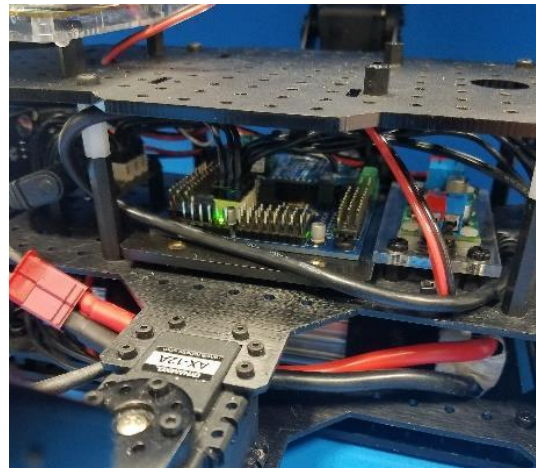
(a)   (b)

Figure 52 (a) Hexapod's Leg; (b) ArbotiX-M Robocontroller.

The DJI S1000+ octocopter was also used in this study as an unmanned aerial system (UAS) platform. A Pixhawk 2.1 (shown in Figure 53) was used as the flight controller of the UAS.
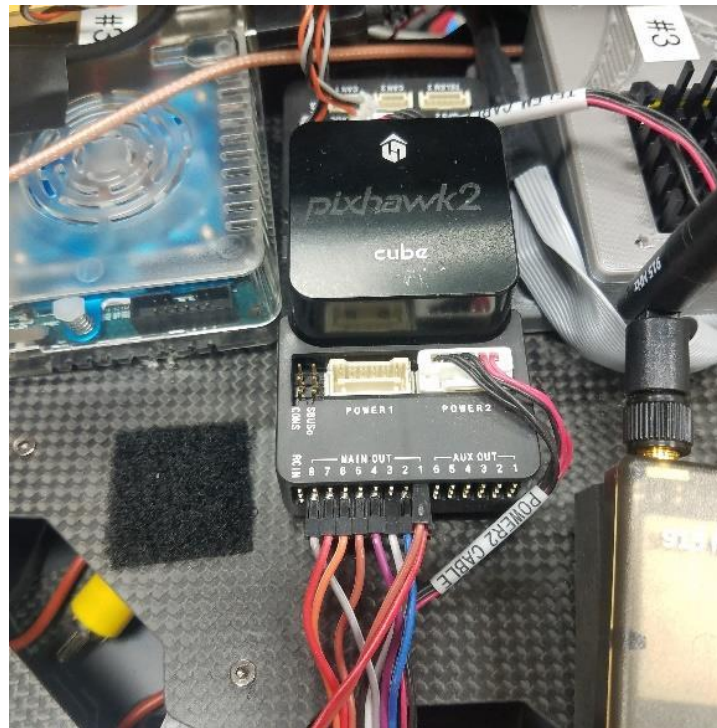
Figure 53: Pixhawk 2.1 Flight Controller.

5.2 Computation Modeling of Radiation Damage

The estimation of radiation damage of the robotic platform is important in order to optimize the robot's operational lifetime while it is irradiated. DPA represents the displacement damage on materials incurred by the radiation, which affects the macroscopic crystal defects. DPA depicts how many times atoms have been displaced from their lattice sites [83], representing the damage-based exposure unit. This unit is directly related to the number of Frenkel pairs. The displacement is induced by a primary knock on atom (PKA) caused by the elastic scattering of incident particles [84]. This is shown in Figure 54.

The Frenkel pairs are a compound crystallographic defect where an atom leaves the lattice sites, creating a vacancy. The atom lodges nearby becoming an interstitial. Hence, Frenkel pairs are vacancy - interstitial pairs. The DPA is calculated as

$$DPA = (A/N_A \rho) \cdot N_F, \qquad \textbf{Equation 11}$$

where ρ is the density in g/cm^3,

N_F is the number of Frenkel pairs,

N_A is Avogadro's number, and A is the mass number.

The FLUKA code was used to calculate the DPA using the Kinchin - Pease damage model modified by Norgert, Robinson, and Torrens. Photons and neutrons interacting with the crystalline materials result in the formation of lattice defects. The electronic components are affected the most while under irradiation, which has a consequence of affecting the platform's operational time. For the protection of the robotic platforms from damage, there are three possible

79

options: to minimize time at the contamination zone; to keep distance from the contaminated zone, or to utilize shielding so that the electronic parts are protected.
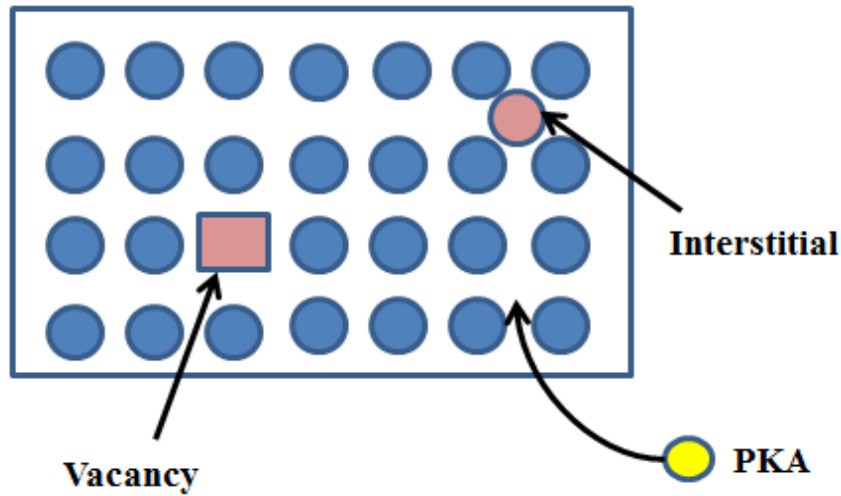
Figure 54: Frenkel Pairs

The PhantomX hexapod carries 18 actuators. The model of the hexapod designed in FLUKA along with 18 actuators. The platform's weight will be affected the most when a radiation shielding is added to actuators, therefore they were studied. For the octocopter, the Pixhawk controller was investigated. The actuators and the Pixhawk were modeled in 3D in FLUKA, shown in Figure 55. The silicon and copper materials in models of these components were taken into consideration. These components were exposed to the neutron and photon beams, varying in energy from 1 MeV to 3 MeV, without shielding to determine the initial DPA per an incident particle or wave. In addition, three cases of shielding were studied: (1) a 55 mm thick layer of polyethylene (low Z material), (2) a 1 mm thick layer of lead (high Z material), and (3) an inner layer of 1 mm of lead and an outer layer of 5 mm of polyethylene.
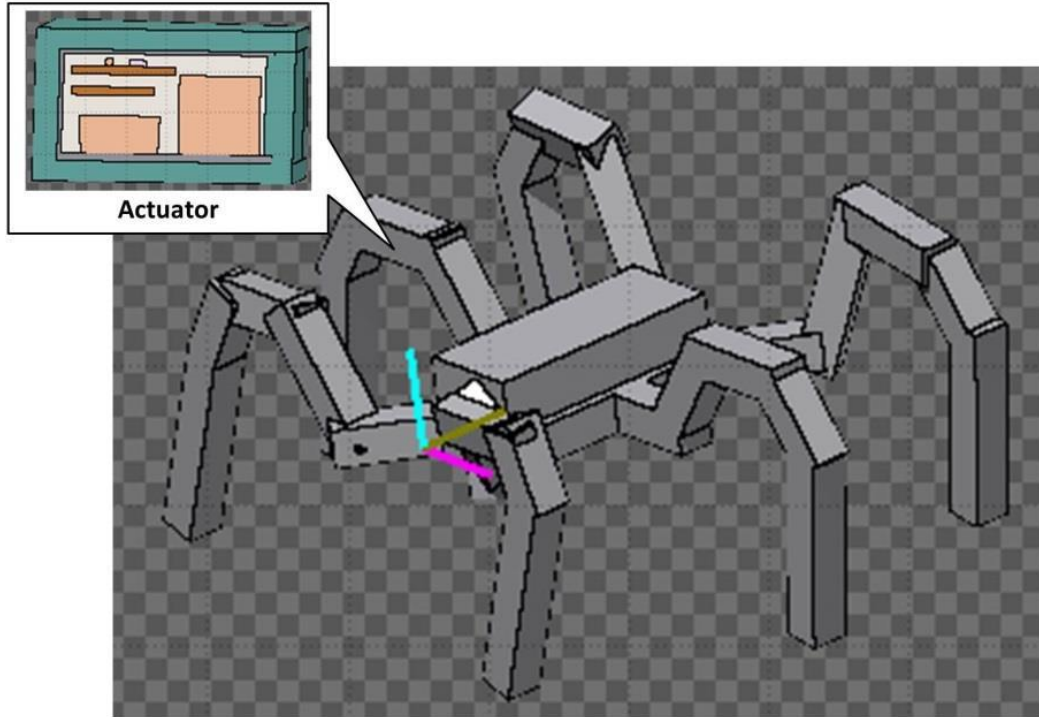
Figure 55: PhantomX Hexapod Design in FLUKA.

The goal is to have the robotic platform completing the required tasks in the set time, while taking into consideration the payload. The FLUKA was used to analyze the DPA using the Kinchin-Pease damage model modified by Norgert, Robinson, and Torrens [85]. Electronic components are the most affected when exposed to high levels of radiation, limiting the platform's operational time. Therefore, electronic components must be shielded. The interaction of photons and neutrons with crystalline materials causes the formation of lattice defects. First, the actuators were exposed to a neutron and photon beam without shielding in order to determine the damage rate as a displacement per atom per second (DPA/s). In the actuator, the components are composed of silicon, plastic, copper, and tin.

Hexapod Actuators

The model of actuators of the PhantomX hexapod was designed in FLUKA. A scheme of shielding layers for the actuator is shown in Figure 56. Different cases of the shielding of thickness t were computed as follows. In FLUKA, the actuators were irradiated by neutron and photon beams. The DPA values induced by these radiations were calculated. The displacement threshold energy was set to 25 eV for silicon and 22 eV for copper. An atom will be displaced if the transferred energy is larger than the displacement threshold energy. The results of calculations are shown in Table 5 for neutrons and in Table 6 for photons.

Case 0: $t_1 = 0\ mm, t_2 = 0\ mm$. No shielding was used for actuators in this case.

Case 1: $t_1 = 0\ mm, t_2 = 5\ mm$. A single layer of a low Z material, polyethylene $(C_2H_4)_n$, was added around the actuator. The density of this polymer is $0.96\ g/cm^3$. The total weight of the polyethylene for 18 actuators added to the robotic platform would be 292 grams. This shielding decreased the DPA/neutron by almost half.

Case 2: $t_1 = 1\ mm, t_2 = 0\ mm$. A single layer of a high Z material, lead, was used to shield the actuator. The density of lead is $11.37\ g/cm^3$. The total weight added to the robotic platform would be 692 grams for all actuators.

Case 3: $t_1 = 1\ mm, t_2 = 5\ mm$. In this case, two layers were used: lead and polyethylene. The weight of the added lead and polyethylene shielding would be 983 grams. This case presented the least DPA/neutron and DPA/photon values; however, it had the most added payload.
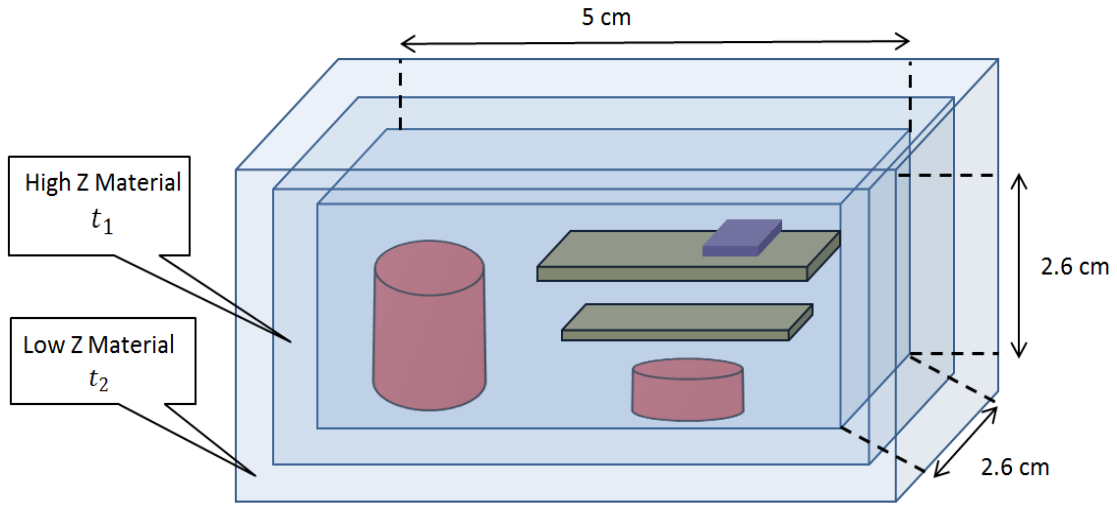
Figure 56: Scheme of the Actuator Shielding.

Table 5: Radiation Damage due to Neutron Irradiation of Actuators

Neutron Energy	1 MeV	2 MeV	3 MeV
Case 0: DPA per Incident Neutron ($\times 10^{-22}$)	4.5	4.6	6.1
Case 1: DPA per Incident Neutron ($\times 10^{-22}$)	0.22	0.24	0.36
Case 2: DPA per Incident Neutron ($\times 10^{-22}$)	0.15	0.18	0.35
Case 3: DPA per Incident Neutron ($\times 10^{-22}$)	0.078	0.045	0.024

Table 6: Radiation Damage due to Photon Irradiation of Actuators

Photon Energy	1 MeV	2 MeV	3 MeV
Case 0: DPA per Incident Photon ($\times 10^{-26}$)	1.2	1.7	4.2
Case 1: DPA per Incident Photon ($\times 10^{-26}$)	0.57	0.93	3.5
Case 2: DPA per Incident Photon ($\times 10^{-26}$)	0.43	0.71	2.2
Case 3: DPA per Incident Photon ($\times 10^{-26}$)	0.18	0.54	0.64

Pixhawk UAS Controller

The model of the UAS controller was designed in FLUKA. A scheme of the shielding layers is shown in Figure 57. The following cases of the controller's shielding were analyzed.

Case 0: $t_1 = 0\ mm$, $t_2 = 0\ mm$. The DPA per incident photon and DPA per incident neutron were calculated without shielding.

Case 1: $t_1 = 0\ mm$, $t_2 = 5\ mm$. A single layer of polyethylene was used. The total added weight of the polyethylene on the robotic platform would be 85.44 grams.

Case 2: $t_1 = 1\ mm$, $t_2 = 0\ mm$. A single layer of lead was used to shield the actuator. The weight of the added lead would be 202.4 grams.

Case 3: $t_1 = 1\ mm$, $t_2 = 5\ mm$. Two layers - lead and polyethylene - were used. The added weight of the two-layer shielding would be 287.8 grams. This case showed the least values of DPA per an incident photon and DPA/neutron. The results are shown in Table 7 for neutrons and Table 8 for photons.
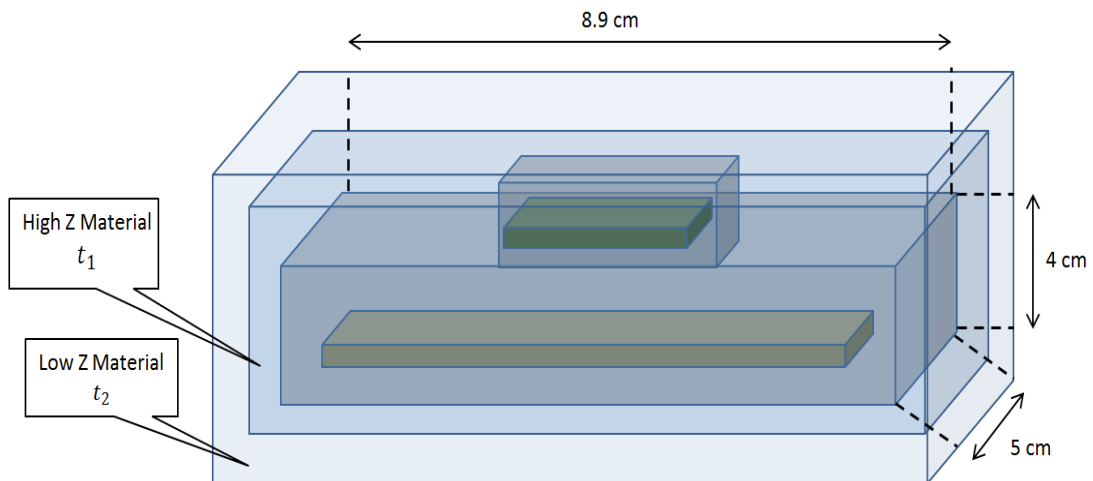
Figure 57: Shielding of the Pixhawk UAS controller.

Table 7: Radiation Damage due to Neutron Irradiation of Controller

Neutron Energy	1 MeV	2 MeV	3 MeV
Case 0: DPA per Incident Neutron ($\times 10^{-22}$)	6.9	8.4	9.5
Case 1: DPA per Incident Neutron ($\times 10^{-22}$)	6.0	6.4	7.3
Case 2: DPA per Incident Neutron ($\times 10^{-22}$)	4.6	5.3	6.8
Case 3: DPA per Incident Neutron ($\times 10^{-22}$)	3.5	4.1	5.3

Table 8: Radiation Damage due to Photon Irradiation of Controller

Photon Energy	1 MeV	2 MeV	3 MeV
Case 0: DPA per Incident Photon ($\times 10^{-25}$)	3.9	26.0	48.6
Case 1: DPA per Incident Photon ($\times 10^{-25}$)	3.0	14.6	38.9
Case 2: DPA per Incident Photon ($\times 10^{-25}$)	0.28	0.47	2.9
Case 3: DPA per Incident Photon ($\times 10^{-25}$)	0.09	0.27	0.35

The FLUKA code was utilized to analyze values of DPA per incident particle (or an electromagnetic wave) in materials. Layers of low density and high-density compounds were used to shield the components so that the DPA values were reduced while keeping a reasonable payload increase due to the added shielding. The shielding with 1 mm of lead and 5mm of polyethylene showed the least DPA/neutron and DPA/photon for both platforms. The case of the 1 mm lead shielding and the case of the two-layer lead-polyethylene shielding will be appropriate. When the shielding is too thick, it may also restrict the actuator's freedom of motion. The tradeoff between the added weight and the operational time of the robotic platform is necessary based on the specific task. The peaks in the graphs correspond to the actuator zones where silicon and copper are present.

In the actuator, the components are composed of silicon, plastic, copper, and tin. Figure

58 shows the DPA/s values along the actuator length for a neutron beam varying in energy from 1 MeV to 3 MeV. Figure 59 DPA/s values along the actuator length for a photon beam varying in energy from 1 MeV to 3 MeV. The peaks in the graphs correspond to the actuator zones where silicon and copper are present.

(a)

(b)
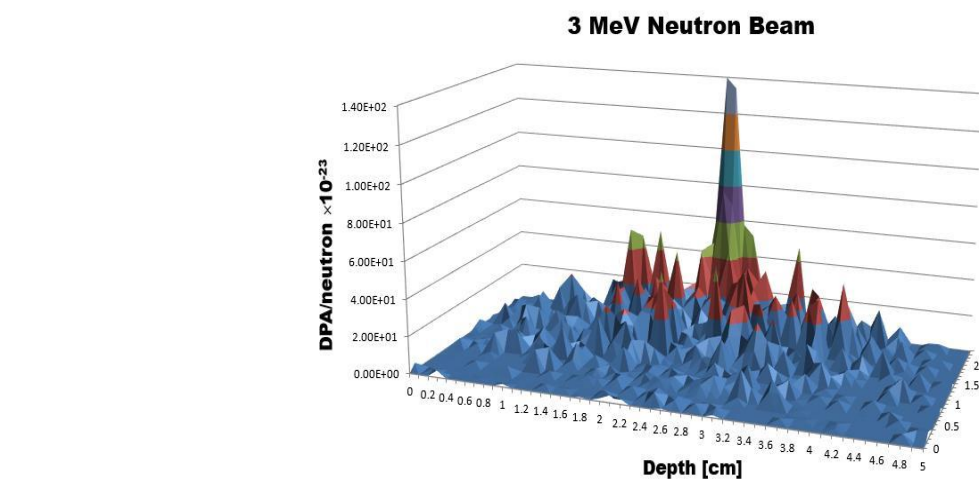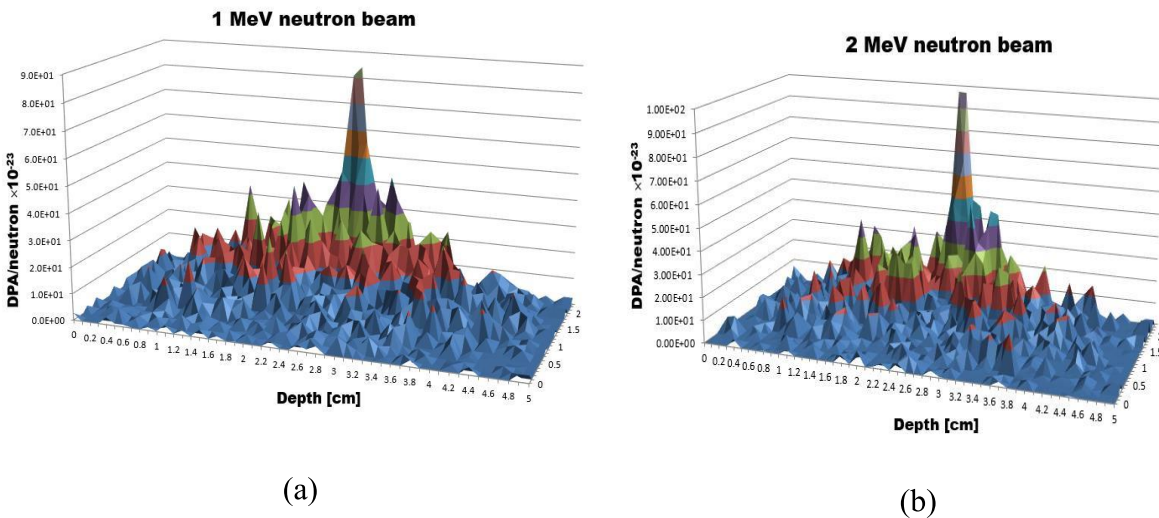
Figure 58: Radiation Damage Data for the Actuator for the Neutron Beam: (a) 1 MeV; (b) 1 MeV ; (c) 2 MeV Beam; (d) 2 MeV Beam.
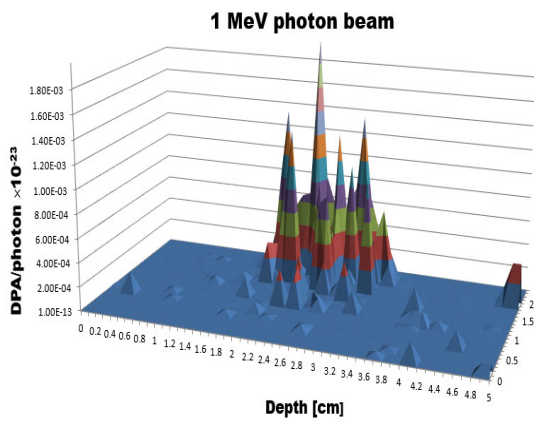
(a)
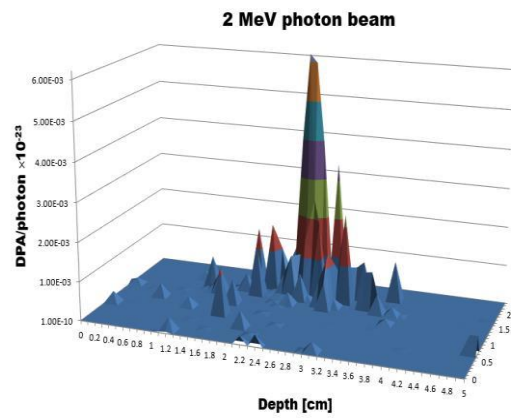
(b)
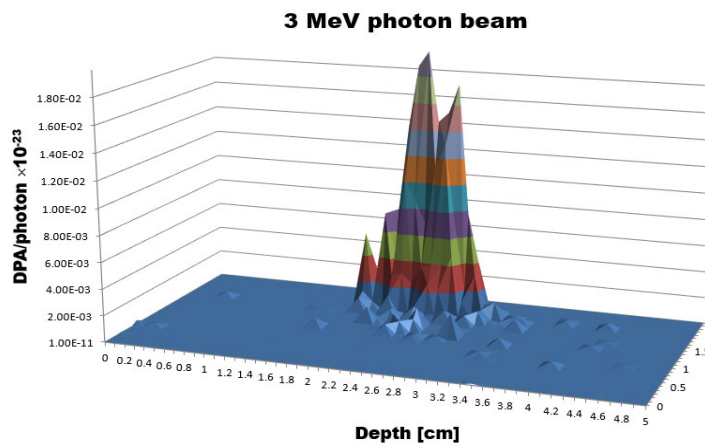
(c)

Figure 59: Radiation Damage Data for the Actuator for the Photon Beam: (a) 1 MeV; (b) 1 MeV ; (c) 2 MeV Beam; (d) 2 MeV Beam.

The minimum energy that is required to form a Frenkel Pair is the threshold displacement energy. This is a very important parameter of the radiation damage from the DPA. For each material, the threshold displacement energy is different. Once the energy of the damage event is above the threshold energy, there will be point defects. Once the DPA is above 10% of the lattice site, the electronic would start to fail.

When the radiation comes in contact with the detectors, a signal is produced. However, what is not taken into consideration is that when these detectors go to areas where the contamination is high, it will affect the detector. The detectors measures the energy incident on the particular area of the detector's volume [86]. A radiation detector is affected by how the detector will be used and where it will be used [87, 88]. Different settings and what the detector is going to be used for affects the radiation detectors. Awareness of the established radioactive zones are extremely helpful. However, when searching and monitoring, the radiation detector goes to areas where the contamination is unknown. So therefore, there is a risk of the radiation detector becoming damaged. The task is to plan accordingly. Radiation detectors need to be highly sensitive, but at the same time, they need to be protected just like other electronic components in the robotic platform.

When robotic platforms are exposed to high levels of radiation, it could lead to microscopic defects, which includes dislocation loops, voids, defects, or termination. Shielding composed of layers of low Z and high Z materials was added around the electronic components to lower the DPA. The shielding with the 1 mm of lead and 5 mm of polyethylene showed the least DPA/s values; however, this case had the most payload.

In FLUKA, the CLYC sintallation detector was modeled in FLUKA to see the affect of the radiation damage. A model of the CLYC is shown in Figure 60. A side view, top view, and 3D

view is shown. The CLYC is shown in the green and a plastic casing was surrounding the CLYC. The beam is located in front of the CLYC detector.

(a)

(b)

(c)
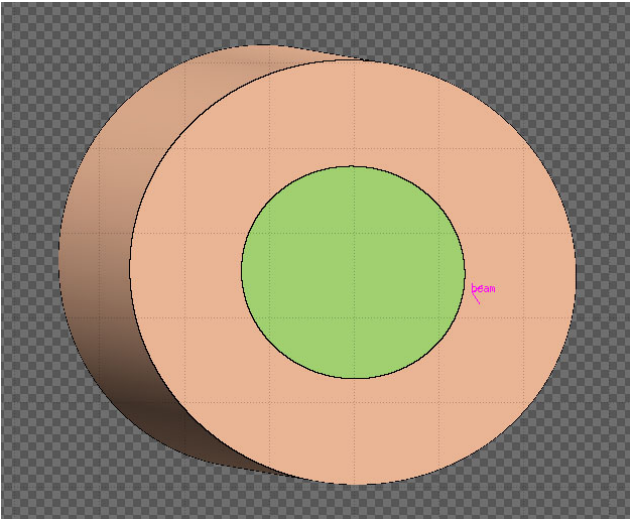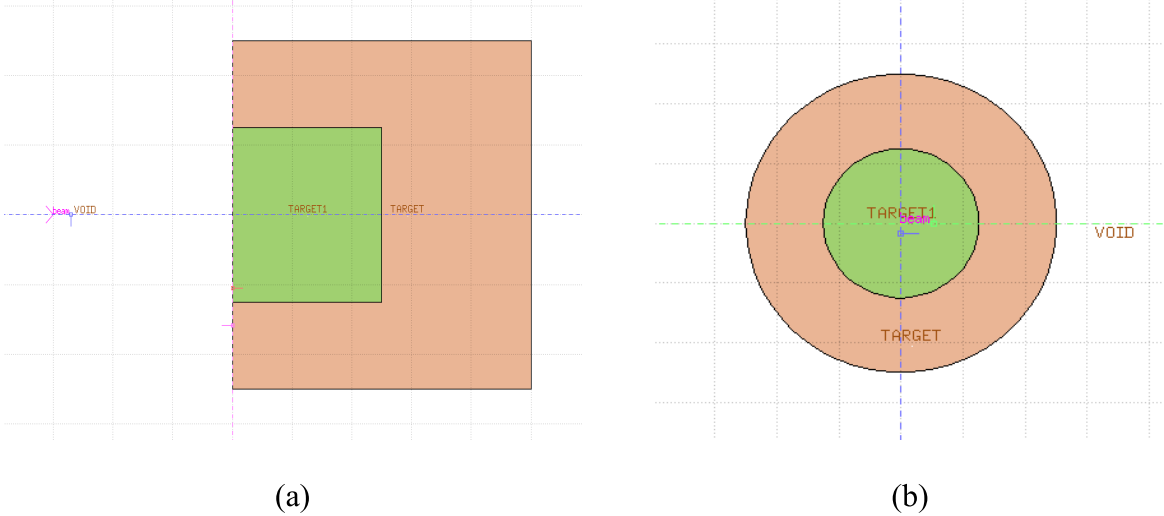
Figure 60: CLYC Scintillation Detector Modeled in FLUKA; (a) Side View, (b) Top View, and (c) 3D View.

A photon and neutron beam were exposed to the CLYC scintillation detector at 1 MeV, 2 MeV, and 3 MeV to see the effect of the detector. Appendix A shows the results of the DPA calculations for the CLYC. The results show the x and y axis of the detector at the point where the DPA values are the most.

Since different detectors have different radiation damage, the CZT detector was also taken into consideration. The CZT detector was modeled in FLUKA to see the affect it would have from the high levels of radiation. The CZT detector was modeled and shown in Figure 61.
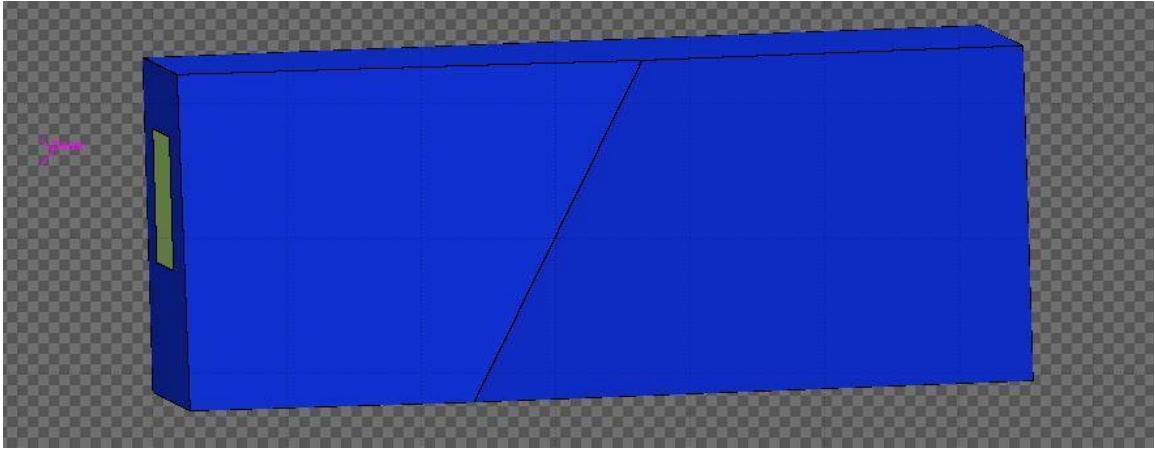
(a)
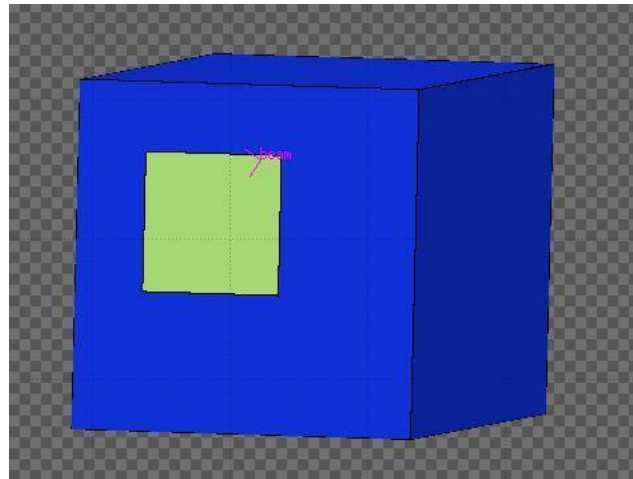
(b)

Figure 61: Model of CZT Detector.

A photon and neutron beam were also exposed to the CZT scintillation detector at 1 MeV, 2 MeV, and 3 MeV to see the effect of the detector. Appendix B shows the results of the DPA calculations for the CZT. The results show the x and y axis of the detector at the point where the DPA values are the most.

The CZT produced more damage. The reason for this is because semiconductor's electronic components are more prone to radiation damage. This is caused by the deterioration of the individual semiconductor layers within the detector.

Next, a SRIM/TRIM code [89] was used. SRIM, Stopping and Range of Ions in Matter, and TRIM, the Transport of Ions in Matter, are used to calculate the stopping and range of ions by using quantum mechanical treatment. This program was used to calculate the target damage. First, the energy loss to ionization and phonons were plotted. The ionization is the energy loss from the target's electrons. The target's electrons absorb the energy from the ions and recoil atoms. It then releases as heat or as the phonons. The phonons are the energy stored in atomic vibrations. It is assumed that the atoms in the crystals are linked. When one starts vibrating, then the others start vibrating as well. Figure 62 shows the energy loss to the phonons, the displacement per Angstrom per ion is shown in Figure 63, and the collision events is shown in Figure 64. The collision events show the target depth and the number of vacancies produced. TRIM allows for the interface mixing and sputtering.
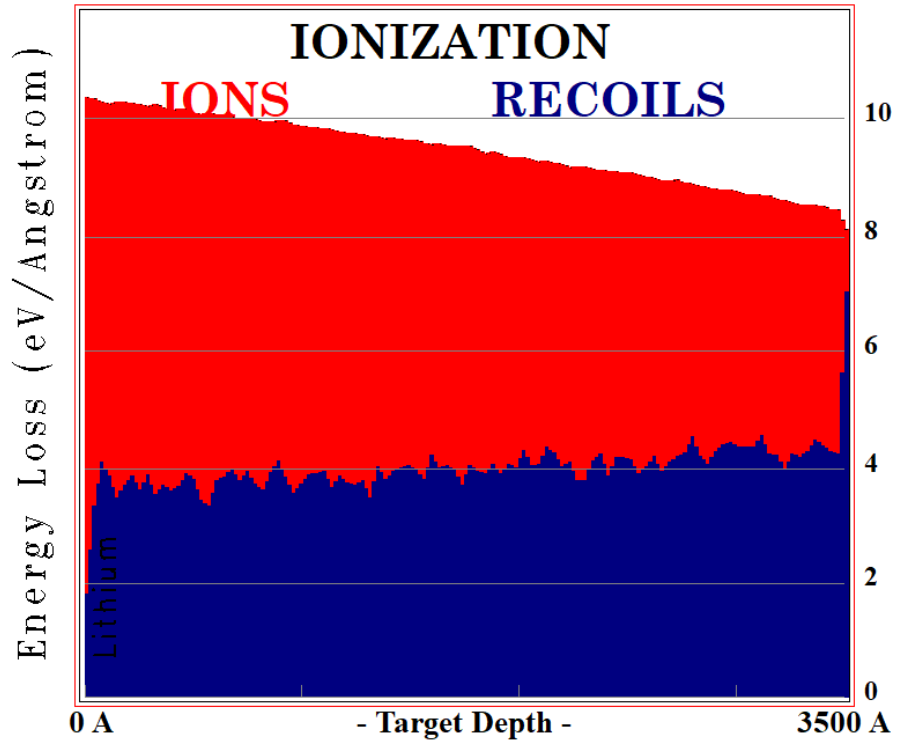
Figure 62: Energy Loss to the Phonons.
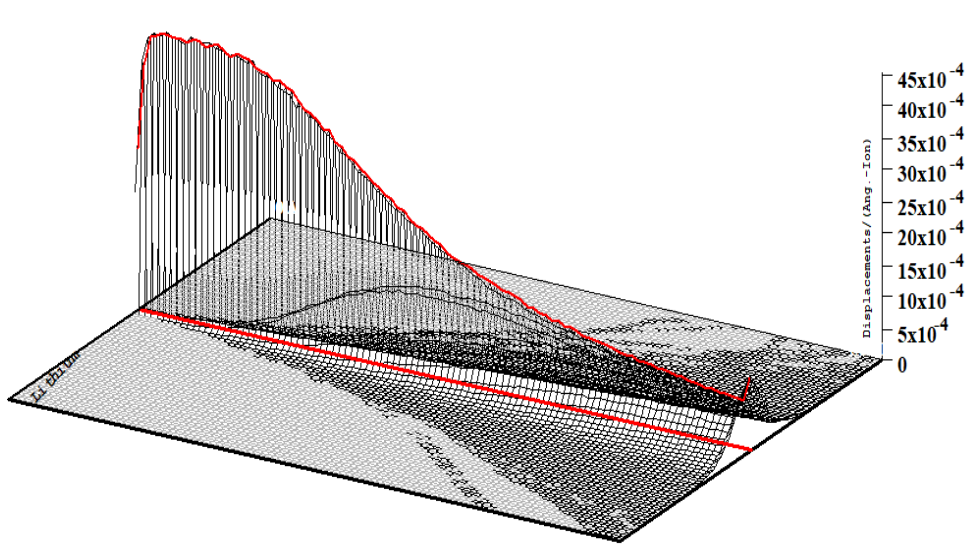
Figure 63: 3D Plot of Displacement per Ion.

93
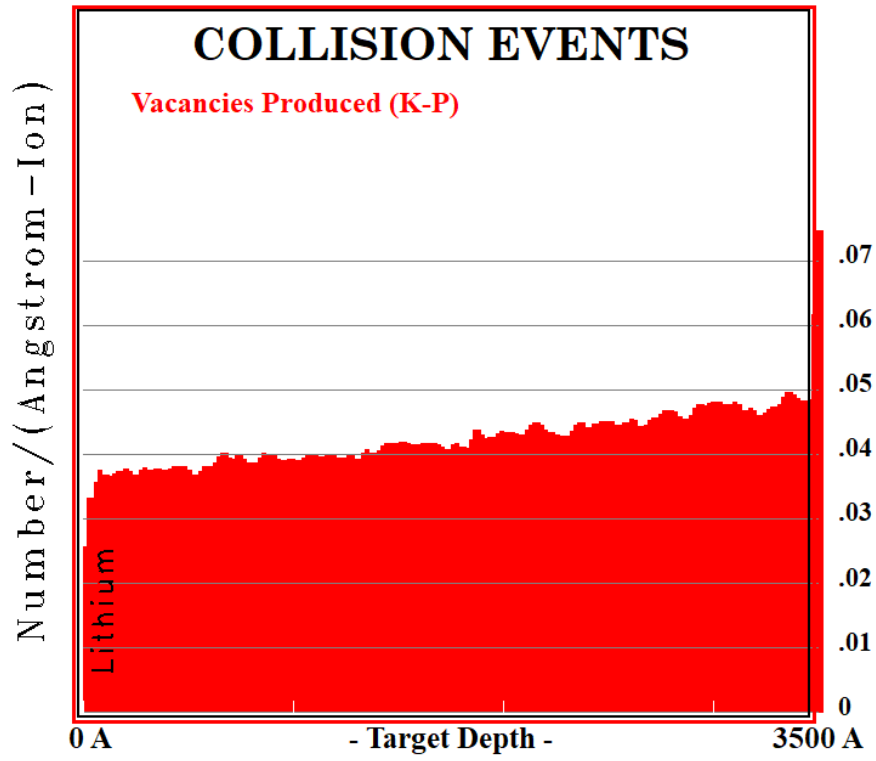
Figure 64: Collision Events Plot.

5.3: Packaging of Components and Shielding Design

From the DPA calculations, a shielding analysis was determined so that the best scenario for shielding was determined. There are three factors that control the amount of radiation. These factors are time, distance, and shielding. By reducing the time, it would reduce the effect of the radiation. Next, by taking into consideration theinverse square law, reducing the distance from the radiation sourse also reduces the amaount of radiaiton. However, in this case, the robotic platfrom should go to the contamination zones to perform the necessary tasks. So therefore, the factor to consider is shielding.

The characterization of the radiation emitted and shield properties were carefully analyzed. In order to determine the best shielding, comprehensive information such as the matieral properties, thermal properties, and structural properties [90]. The goal is to have the minimal wieght, volume, and cost.

Some of the properties and compositions of shielding mateirals are shown in Table 9: Properties and Compositions of Shielding Mateirals. However, the main goal is to protect the electronics of the system so that it could provide the most tasks while in a specified time frame. Gamma rays and x-rays have high energy wave that are able to penetrate materials and travel unlimited distances. These kinds of radiation are usually blocked with few inches of contrete or lead. However, these were shown to have the most weight.

Beta particles also have an ability to penetrate materials. They are able to pass through skin, plastic, or even a sheet of metal.

Table 9: Properties and Compositions of Shielding Mateirals

Material	Melting Point	Boiling Point	Flammability	Density
Lead	327.4 °C	1,740 °C	No	11.29 g/cm^3
Polyethylene	115-135 °C	120 °C -180 °C	Yes	0.88-0.96 g/cm^3
Aluminum	660.3 °C	2,467 °C	Yes	2.70 g/cm^3
Silicon	1,414 °C	3,265 °C	No	2.32 g/cm^3
Iron	1,538 °C	2,862 °C	No	7.874 g/cm^3
Cobalt	1, 495 °C	2,870 °C	Yes	8.86 g/cm^3
Nickel	2,455 °C	2,913 °C	Yes	8.908 g/cm^3

The shielding that was taken into consideration was the one with the least density and the most desnsity so that the resulting DPA can be seen. The Polyethlene has the least amount of weight and the lead has the most amount of weight. The thicker the lead sheild is, the lower the DPA. High density materials are much more effective in reducing the intensity of the radiation than lower-density materials [91]. However, the weight causes the robotic platform to have more payload. So therefore, it would defeat the purpose since more payload on the robotic platform would cause lower operational time of the robot.

It is important to realize the different principles involved in the interations with radiation in order to best determine the choice for shielding. Sometimes even with shielding, an absolute barreier may not be possible.

The life time of the robot depends on the displacement rate, which is shown as

$$\frac{dpa}{s} = \int_0^\infty dE\, \sigma_d(E)\alpha(E,t) \qquad \textbf{Equation 12}$$

Where E is the neutron energy

σ_d is the atomic displacement cross-section

$\alpha(E,t)$ is the flux spectrum of the neutron energy and time

The amount of dpa is obtained by taking into consideration the exposure time

$$dpa = \int_0^{t_e} dt \int_0^\infty dE\, \sigma_d(E)\alpha(E,t) \qquad \textbf{Equation 13}$$

Where t_e is exposure time

It is assumed that the flux spectrum to be constant over the exposure time. So there, the equation is:

$$dpa = t_e \phi_{tot} \int_0^\infty dE\, \sigma_d(E)\alpha(E,t) \qquad \textbf{Equation 14}$$

Where ϕ_{tot} is the time dependent flux intensity

In FLUKA, the DPA is represented as

$$dpa = \frac{A}{V N_A \rho} N_F \qquad \textbf{Equation 15}$$

Where is ρ is the mass density

V is the volume

N_A is the Avagadros number

N_F is the number of Frenkel pairs

After obtaining the FLUKA results, the operational time [92] was determined by

$$\frac{dpa}{s} = \frac{\phi \times d}{A} \qquad \textbf{Equation 16}$$

Where d is the atom dipalcements

A is the atomic density

For each of the calculations, the atomic density would be for the target's materials. The resulting

answer would be in seconds.

Chapter 6: Conclusion and Future Work

Radiation area monitoring and visual inspections became an essential component in many operations such as radiation safety and enviromental security. The automation of monitoring tasks in normal operational regimes of nuclear facilities is vital as well. Nuclear facility workers and first responders face significant challenges during a nuclear accident, and one of the major challenges is acting decisively based on available information from real-time data critical to manage and safeguard personnel and infrastructure. The use of robotic platforms equipped with gamma-ray and neutron sensors enables monitoring of ionizing radiation in hard to reach hazardous zones where the contamination is unknown. To keep personnel away from the radiation exposure by using remote measurement techniques, these sensors were integrated into robotic platforms, and the analysis of sensor's signals should be automated and carried out onboard. Two sensors were integrated into an octocopter aerial platform to address this need: a semiconductor CZT gamma-ray sensor and an elpasolite CLYC scintillator gamma/neutron sensor. To allow easy deployment in the field, both radiation sensors were designed as plug-and-play components using the ROS for onboard processing of the sensor's data and for fusion of the processed data with the RTK GPS information. The evaluation of radiation damage in electronic components of robots is critical. The radiation damage analysis was carried out for robotic platforms. The packaging of the components and the shielding design was determined to increase the robot's lifetime in areas where radiation dose levels are high.

The first objective of this dissertation was the study of the radiation detectors for robotic platforms. The radiation sensors were integrated with the robotic platform using ROS. Next, the plug-and-play and plug-and-fly operation of the detectors was designed. This works by the operating system detecting and configuring the internal and external devices. The final task of this

objective is to have the operating system process and analyze the sensor data and then publish the results forming a message. The measurements contain RTK GPS data and a timestamp. The analysis of the measured sensor's data was carried out using an onboard computer while taking into account its limited data processing capabilities.

The second objective is to develop the source search methods using a single platform and multiple platforms. The Mariscotti technique for the automatic identification of peaks in the presence of background was implemented. The approach assumes that these peaks are described by a Gaussian and the background is described by a linear function within a small energy range (i.e., several peak widths). Next, the maximum likelihood estimation technique was employed to locate the position of the radiation source based on the measured peak intensities. This was achieved by the radiation measurements in three or more locations by a single UAS or simultaneously by multiple UAS. The final task of this objective is to use MCNP for high fidelity modeling of radiation fields. The source seeking and contour mapping algorithms were tested using these radiation field data.

The third objective is the evaluation of radiation damage in electronic components of robots. The estimation of radiation damage of the robotic platform is important in order to optimize the robot's operational lifetime while it is irradiated. The DPA was determined on the electronic components of the robotic platform. Next, the operational time of the robotic platforms under various irradiation conditions was evaluated. For the protection of the robotic platforms from the radiation damage, there are three possible options: to minimize time at the contamination zone, to keep distance from the contaminated zone, or to utilize shielding. The packaging of the components and the shielding was designed so that there would be an increase in the robot's lifetime. The objectives of this dissertation were completed.

Future Work

The following recommendations are provided for the future expansion of this dissertation work. For the robotic platforms, a larger payload platform should be utilized so that more detectors and more instruments could be used, and the longer flight time option should be designed. The 2D MLE method should be expanded to a 3D version (to include the ground robot sensor's data, for example) to provide a more detailed information of where the source is. A hybrid source search method to minimize the time of the search can be developed. This hybrid method can combine the probabilistic search techniques and the gradient-based deterministic search methods. Also, an advanced method of data fusion should be considered taking into account dissimilar sensors and LIDAR data from several sources. Finally, for the radiation damage, the additional shielding versions should be analyzed so that the robotic platform operational time would be optimized in any scenario of the irradiation.

Appendices

Appendix A:

Radiation Damage Data for the CLYC for the Following Incident Beams: (a) 1 MeV Photon Beam; (b) 2 MeV Photon Beam; (c) 3 MeV Photon Beam; (d) 1 MeV Neutron Beam; (e) 2 MeV Neutron Beam; (f) 3 MeV Neutron Beam.

(a)

(b)

Photon Beam: 3 MeV

(c)

Neutron Beam: 1 MeV

(d)

103

Neutron Beam: 2 MeV

(e)

Neutron Beam: 3 MeV

(f)

Appendix B:

Radiation Damage Data for the CZT for the Following Incident Beams: (a) 1 MeV Photon Beam; (b) 2 MeV Photon Beam; (c) 3 MeV Photon Beam; (d) 1 MeV Neutron Beam; (e) 2 MeV Neutron Beam; (f) 3 MeV Neutron Beam.

(a)

(b)

Photon Beam: 3 MeV

(c)
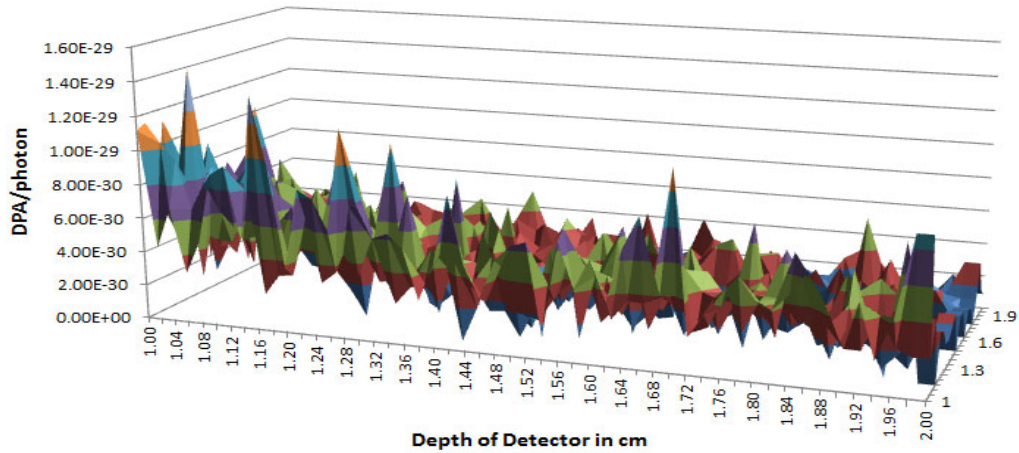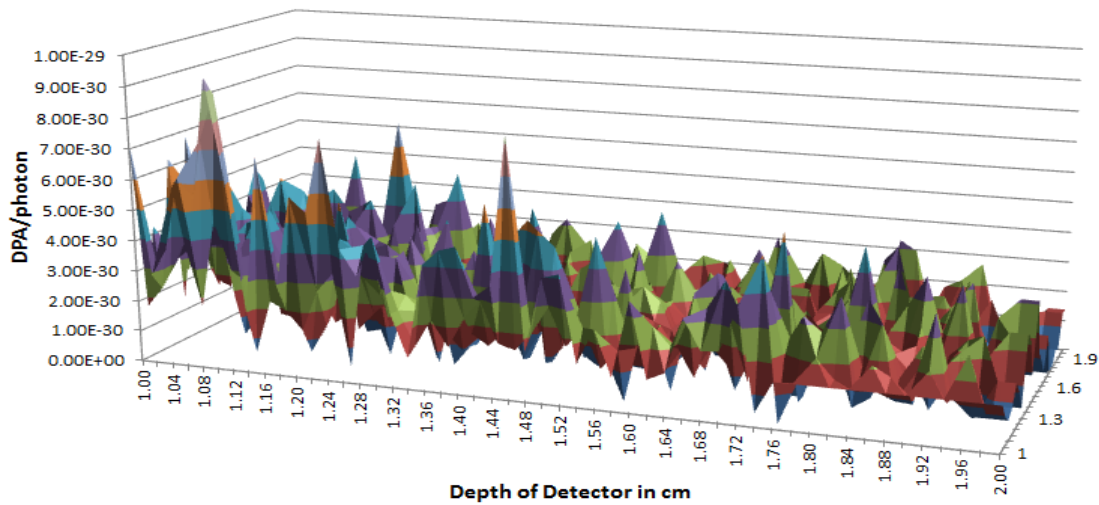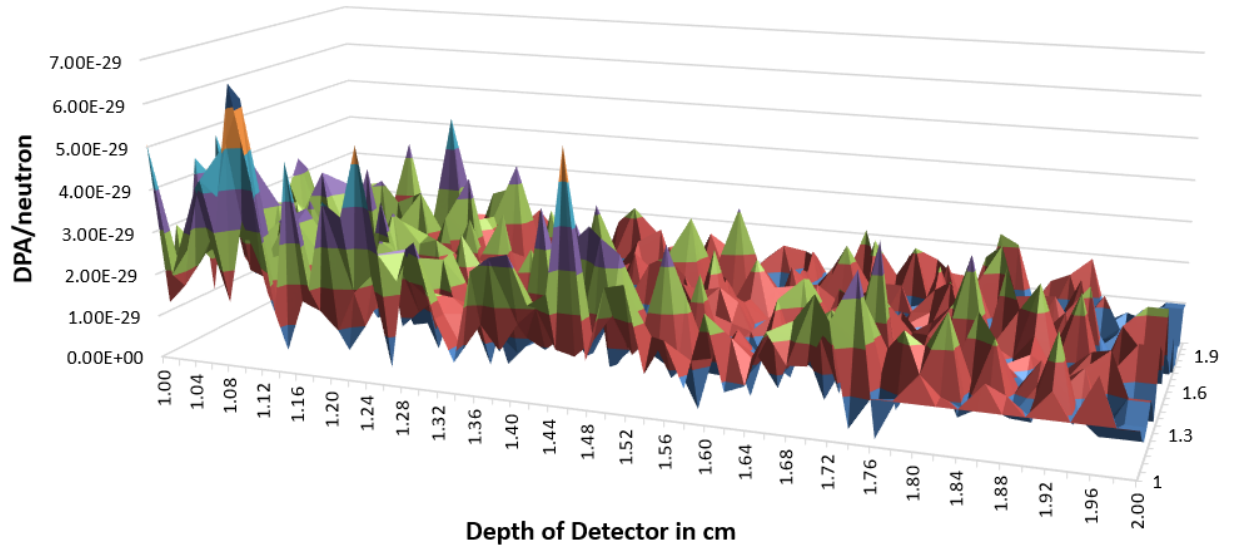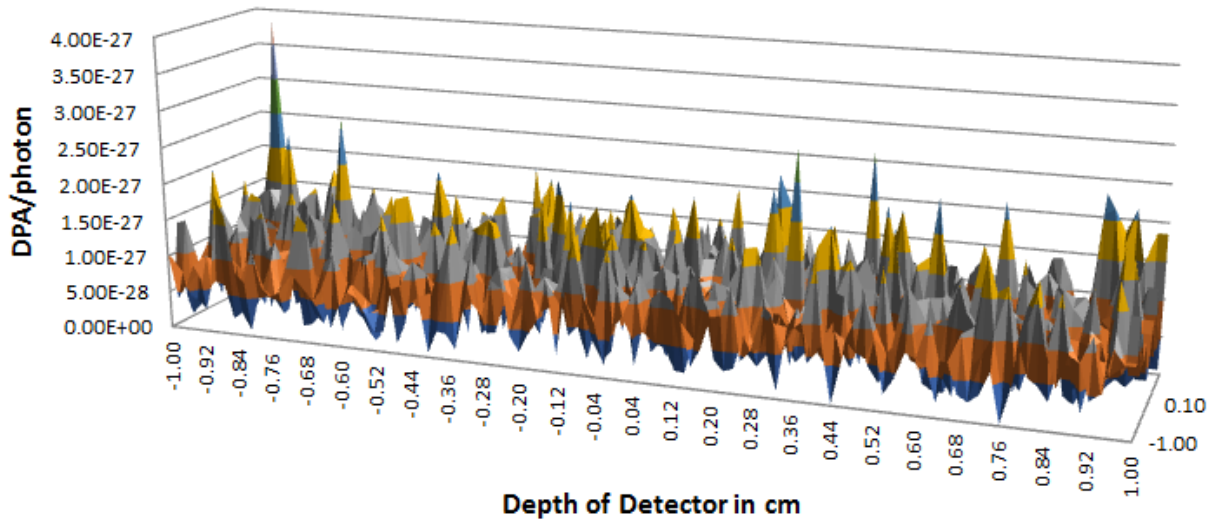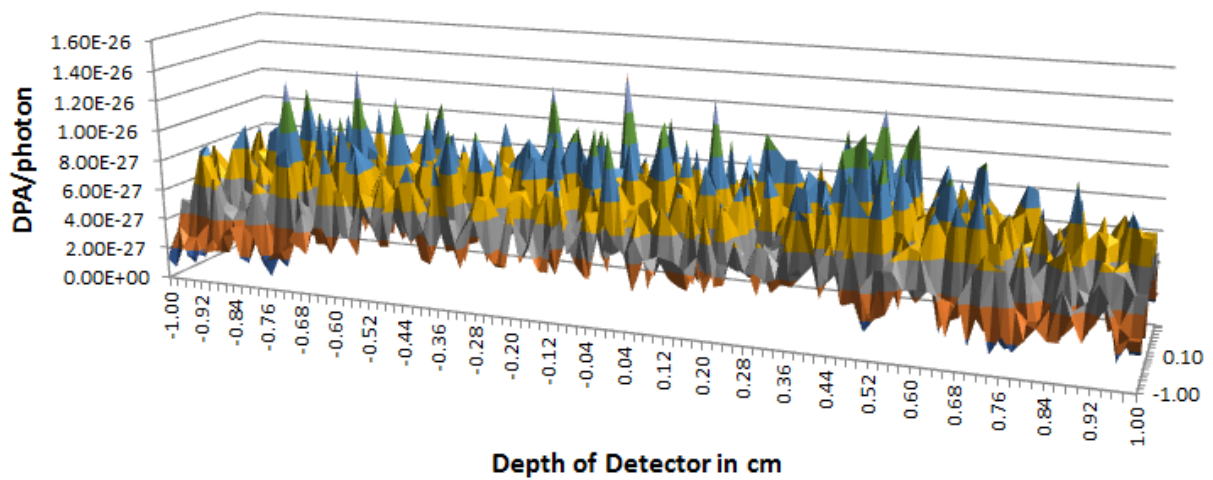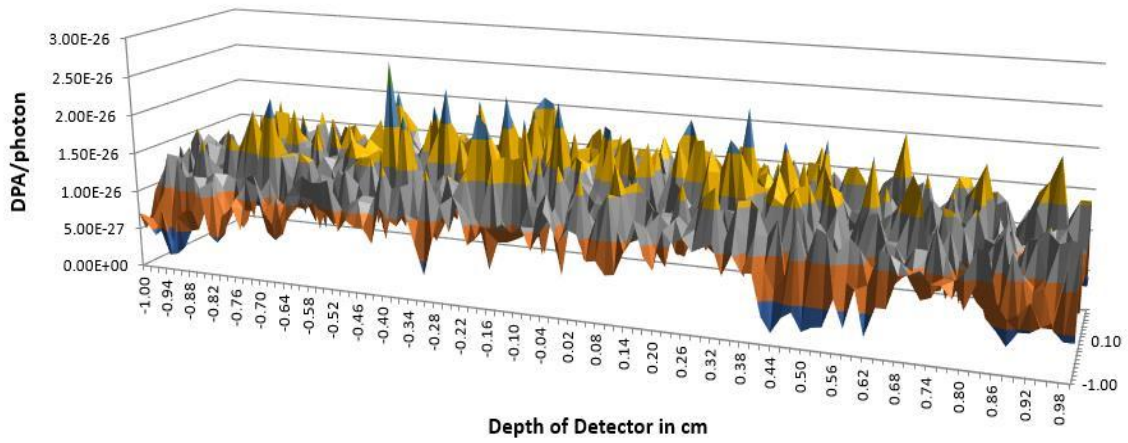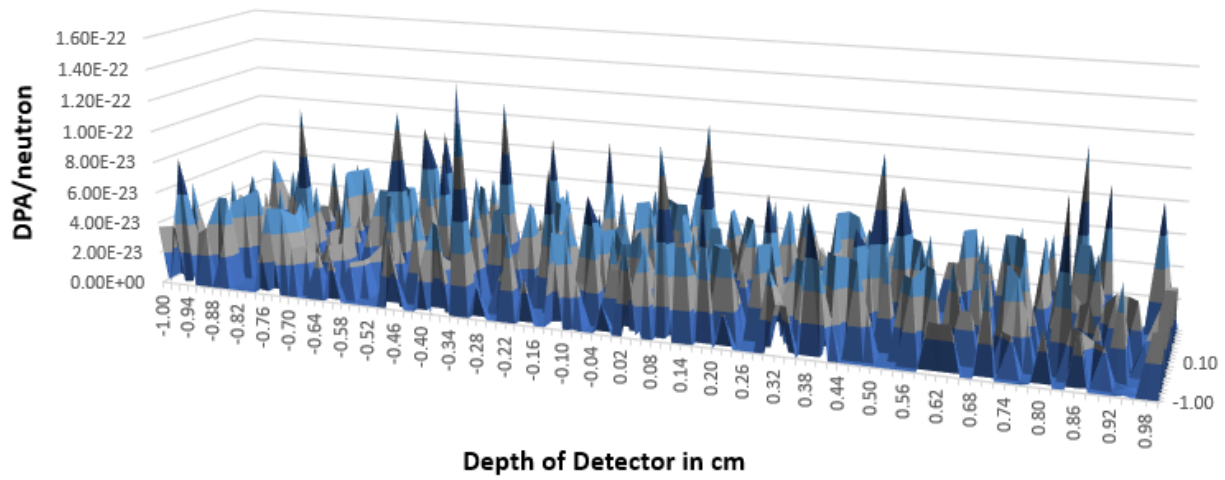
Neutron Beam: 1 MeV

(d)

Neutron Beam: 2 MeV

(e)

Neutron Beam: 3 MeV

(f)

107
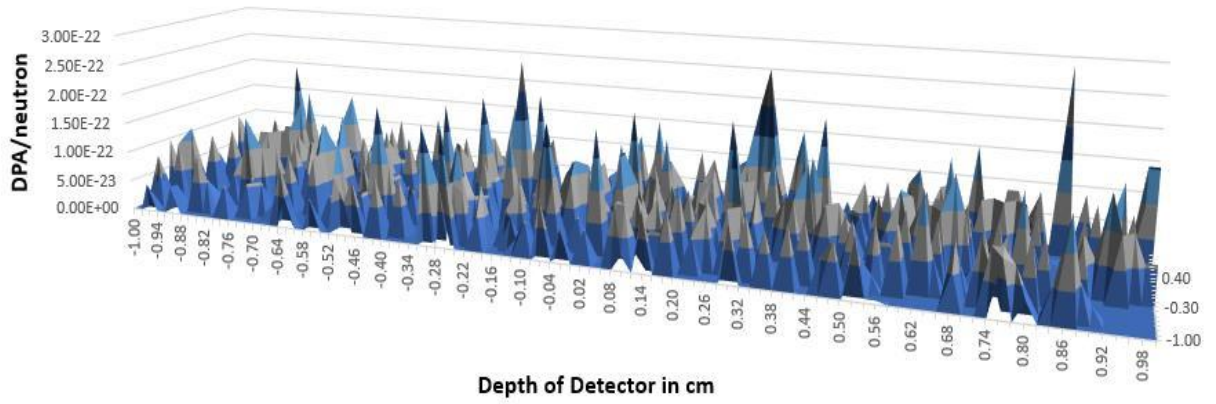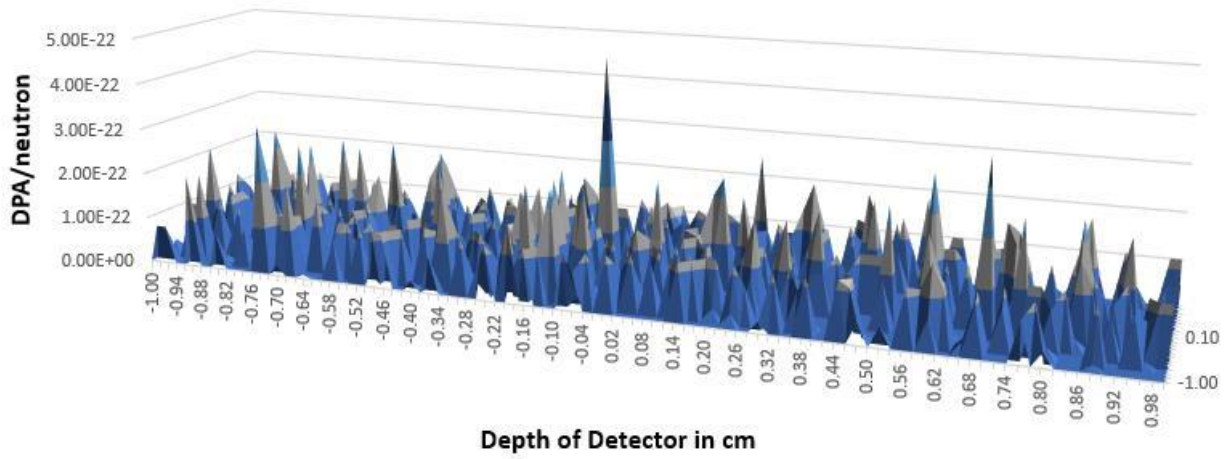
References

[1] J. R. Lamarsh and A. J. Baratta, Introduction to Nuclear Engineering, Upper Saddle River: Prentice Hall, 2001.

[2] S. Deme, Semiconductor Detectors for Nuclear Radiation Measurement, Budapest: Akademiai Kiado, 1971.

[3] M. Prokesch, "CdZnTe for Gamma and X-ray Applications," Solid-State Radiation Detectors: Technology and Applications, pp. 17-48, 2015.

[4] R. B. James, "Improved CZT for Gamma Detection," Brookhaven National Laboratory, 2015.

[5] A. Selivanova, J. Hulka, T. Vrba and I. Cespirova, "Efficiency Calibration of a CZT Detector and MDA Determination for Post Accidental Unmanned Aerial Vehicle Dosimetry," Elsevier, 2019.

[6] G. Healthcare, "CZT Technology: Fundamentals and Applications," Transformational Medical Technologies, pp. 1-8, 2010.

[7] S. Vichi, A. Infantino, F. Zagni, G. Cicoria, M. Marengo and D. Mostacci, "Efficiency Calibration of a Portable CZT detector for Nondestructive activation Assessment of a Cyclotron Bunker," Radiation Effects and Defects in Solids, vol. 173, pp. 705-713, 2016. doi: 10.1080/10420150.2016.1244675.

[8] I. Akkurt, K. Gunoglu and S. Arda, "Detector Efficiency of NaI Detector," Science and Technology of Nuclear Installations , vol. 2014, pp. 1-5. https://doi.org/10.1155/2014/186798.

[9] U. Kramar, "Scintillation Detector," Encyclopedia of Spectroscopy and Spectrometry, 1999.

[10] J. Hartman, A. Barzilov, E. Peters and S. Yates, "Measurement of Response Functions of EJ-299-33A Plastic Scintillator for Fast Neutrons," Nuclear Instruments and Methods in Physics Research Section A: Accelerators, Spectrometers, Detectors and Associated Equipment, vol. 804, pp. 137-143, 2015. https://doi.org/10.1016/j.nima.2015.09.068.

[11] W.E Kisieleski, "Principles of Radiotracers Methodology" Argonne National Laboratory, 1975, pp. 47-156.

[12] J. Hartman, A. Barzilov and I. Novikov, "Remote Sensing of Neutron and Gamma Radiation Using Aerial Unmanned Autonomous Systems," in 2015 IEEE Nuclear Science Symposium and Medical Imagining Conference (NSS/MIC), San Diego, CA, 2015, pp 1-4, doi: 10.1109/NSSMIC.2015.7581763.

[13] P. P. Guess, T. G. Stampahar, S. Mukhopadhyay, A. Barzilov and A. Guckes, "Scintillation Properties of a $Cs_2LiLa(Br_6)^{90\%}(Cl_6)^{10\%}$:Ce (CLLBC) Crystal," Proc. SPIE 9215, Radiation Detectors: Systems and Applications XV, 921505, 2014. https://doi.org/10.1117/12.2060204.

[14] P. Guss, T. Stampahar, A. Barzilov and A. Guckes, "Directional Detection of ^{239}Pu," in Proc Int Conference Plutonium Futures, Las Vegas, pp. 151-154, 2014.

[15] P. Guss, T. Stampahar, A. Barzilov, A. Guckes, J. Hartman, S. Mukhopadhyay, M. Haugh, J. Lee, K. Shah, W. Higgins and M. Squillante, "Novel deployment of Elpasolites as a Dual Gamma–Neutron Directional Detector," Site-Directed Research and Development, pp. 89-91, 2014.

[16] P. Guss, T. G. Stampahar, S. Mukhopadyay, A. Barzilov and A. Guckes, "Maximum Likelihood Source Localization Using Elpasolite as a Dual Gamma Neutron Directional Detector," 2015. doi:10.1117/12.2186179.

[17] J. Yu, Z. Wei, F. Meihua, Z. Zixia and C. Can, "Pulse Shape Discrimination Based on Fast Signals from Silicon Photomultipliers," Elsevier ScienceDirect, vol. 894, pp. 129-137, 2018.

[18] B. Morgan and A. Barzilov, "Neutron-Gamma Pulse Shape Discrimination in Elpasolite Scintillation Detector," in INMM Proc. 57th Annual Mtg, Atlanta, Georgia, 2016.

[19] P. G. Martin, "The 2011 Fukushima Daiichi Nuclear Power Plant Accident," Switzerland: Springer Nature, 2019.

[20] W. Yim, A. Barzilov and G. Friesmuth, "Development of Autonomous Robotic Monitoring Vehicle (ARMV) for Aerial Radiation Monitoring," in 10th International Conference of Ubiquitous Robots and Ambient Intelligence (URAI), Jeju, pp. 687-688, 2013. doi: 10.1109/URAI.2013.6677454.

[21] G. Friesmuth, N. Richardson, A. Barzilov and W. Yim, "Development of Aerial Platform for Remote Sensing and Monitoring of Nuclear Power Facilities," Topical Meeting on Decommissioning and Remote Systems 2014 (D&RS 2014) American Nuclear Society, p. 139, 2014.

[22] J. Lee, Z. Cook, A. Barzilov and W. Yim, "Control of an Aerial Manipulator with an On-Board Balancing Mechanism," in Proceedings of the ASME 2016 International Mechanical Engineering Congress and Exposition Volume 4A: Dynamics, Vibration, and Control, Phoenix, Arizona, pp. 11-17, 2016. https://doi.org/10.1115/IMECE2016-66976.

[23] "PhantomX AX Metal Hexapod Mark III," [Online]. Available: http://www/trossenrobotics.com/phantomx-ax-hexapod.aspx.

[24] Omni Vision, [Online]. Available: https://www.ovt.com/sensors/OV5645.

[25] Trossen Robotics Interboti, [Online]. Available: https://www.trossenrobotics.com/dynamixel-ax-18A-robot-actuator.aspx.

[26] Trossen Robotics Interboti, [Online]. Available: https://www.trossenrobotics.com/p/arbotix-robot-controller.aspx.

[27] DJI, [Online]. Available: https://www.dji.com/spreading-wings-s1000-plus.

[28] "ClearPath Robotics," [Online]. Available: https://clearpathrobotics.com/jackal-small-unmanned-ground-vehicle/.

[29] "RobotShop," Pixhawk 2.1 Standard Set, [Online]. Available: https://www.robotshop.com/en/pixhawk-21-standard-set.html.

[30] Kromek's CZT detector, [Online]. Available: https://www.kromek.com/nuclear/kromeks-czt-detectors/.

[31] J. Towler, B. Krawiec and K. Kochersberger, "Radiation Mapping in Post-Disaster Environments Using an Autonomous Helicopter," MDPI, vol. 7, no. 5, 2012.

[32] S. Wanna, B. Anderson, D. Haas, M. Pryor and S. Landsberger, "Automated Gamma Radiation Surveying with a Lanthanum Bromide Detector," Nuclear and Applied Robotics Group.

[33] J. Han and Y. Chen, "Cooperative Source Seeking and Contour Mapping of a Diffusive Signal Field by Formation of Multiple UAVs," in International Conference on Unmanned Aircraft Systems, Atlanta, GA, 2013.

[34] J. Y. Zhu, H. W. Dai and W.-X. Xie, "Maximum Likelihood Estimation of Neutron Source Location," Radiation Measurements and General Instrumentation, 2015.

[35] I. Pinera, C. Cruz, A. Leyva, Y. Abreu, A. Cabal, P. V. Espen and N. V. Remortel, "Improved Calculation of Displacement per Atom Cross Section in Solids by Gamma and Electron Irradiation," ScienceDirect, vol. 339, pp. 1-7, 2014.

[36] M. Bratchenko, V. Bryk, A. Dyuldya, A. Kalchenko, N. Lazarev and V. Voyevodin, "Comments on DPA Calculation Methods for Ion Beam Driven Simulations Irradiation," National Science Center, 2013.

[37] G. Linsley, "Radiological Risk Assessment and Environmental Analysis," The Radiation Safety Journal Health Physics, vol. 96, no. 4, 2009.

[38] K. Moody, I. Hutcheon and P. Grant, "Nuclear Forensic Analysis," Boca Raton, 2005.

[39] T. K. Sen, L. J. Moore and T. J. Hess, "An Organization Decision Support Sysyem for Managing the DOE Hazardous Waste Cleanup Program," Elsevier, vol. 29, no. 1, 2000.

[40] R.C. Runle, A. Bernstein and P. Vanier, "Securing Special Nuclear Material: Recent Advances in Neutron Detection and their Role in Nonproliferation," Journal of Applied Physics, vol. 108, no. 11, 2010.

[41] K. Nagatani, S. Kiribayashi, Y. Okada, K. Otake, K. Yoshida, S. Tadokoro, T. Nishimura, T. Yoshida, M. Fukushuma and S. Kawatsuma, "Emergency Response to the Nuclear Accident at the Fukushima Daiichi Nuclear Power Plants using Mobile Rescue Robots," Journal of Field Robotics, 2012.

[42] M. Kazemeini, A. Barzilov, "Remote Radiation Sensing using Aerial and Ground Platforms," in Waste Management Symposium, Phoenix, Arizona, 2020.

[43] Z. Cook, J. Lee, A. Barzilov and W. Yim, "Contour Mapping Based Radiation Source Localization by UAS Swarm," Transactions-American Nuclear Society, vol. 115, p.1425, 2016.

[44]   Z. Cook, M. Kazemeini, A. Barzilov, W. Yim, "Low-Altitude Contour Mapping of Radiation Fields using UAS Swarm," Intelligent Service Robotics, vol. 12, pp. 219-230, 2019. https://doi.org/10.1007/s11370-019-00277-8.

[45]   A. Barzilov and M. Kazemeini, "DualMode Radiation Sensor for UAS Platform," in Proc. 6th International Electronic Conference on Sensors and Applications, MDPI Proceedings, vol. 42, pp. 1-6, 2019. doi: 10.3390/ecsa-6-06541.

[46]   Z. Cook, M. Kazemeini, A. Barzilov and W. Yim, "Radiation Measurement and Contour Mapping using UAS Swarm," in Institute of Nuclear Materials Management, Novel Technologies, Techniques and Methods for Safeguards and Arms Control Verification, Albuquerque, New Mexico, 2017.

[47]   A. Barzilov and A. Guckes, "Time Encoded Imagining of Neutron and Photons using CLYC Detector Equipped with a Dual Mode Collimator," Sensors and Transducers, vol. 229, no. 1, pp. 78-83, 2019.

[48]   "Multispect Analysis," Kromek, [Online]. Available: https://www.kromek.com/images/products/MSAUSLRev9.pdf.

[49]   L. El-Khoury, "Use of Remote Sensing in Natural Resource Management," American University of Beirut, [Online]. Available: https://staff.aub.edu.lb/~webeco/rs%20lectures.htm.

[50] "Robot Operating System," [Online]. Available: http://www.ros.org.

[51]   A. Barzilov, B. Kessler and P. Womble, "Analysis of 14 MeV Neutron Induced Gamma-Ray Spectra using Multiwavelets," Radiation Measurements, vol. 79, pp. 43-49, 2015.

[52] M. Kazemeini, J. Vargas, A. Barzilov and W. Yim, "Gamma Ray Measurements using Unmanned Aerial Systems," in Use of Gamma Radiation Techniques in Peaceful Applications, IntechOpen, 2019. doi: 10.5772/intechopen.82798.

[53] M. Kazemeini, A. Barzilov and W. Yim, "Remote Sensing of Radiological Materials in a Wide Area using Unmanned Aerial Systems," Proc. Global/Top Fuel 2019, Seattle, Washington, pp.508-513, 2019.

[54] A. Giaz, "The CLYC-6 and CLYC-7 Response to Gamma Rays, Fast, and Thermal Neutrons," Nuclear Instruments and Methods in Physics Research, vol. 810, pp. 132-139, 2016.

[55] A. Barzilov, A. Guckes and P. Guss, "Directional Elpasolite Detector System for Measurements of Neutron and Photon Flux," International Conference on Methods and Applications of Radioanalytical Chemistry, 2015. no. DOE/NV/25946-2401.

[56] J. Hartman, A. Barzilov and S. Peters, "Measurements of Response Function of EJ-299-33A Plastic Scintillator for Fast Neutrons," Nuclear Instruments and Methods in Physics Research, vol. 804, pp. 137-143, 2015. https://doi.org/10.1016/j.nima.2015.09.068.

[57] M. Kazemeini, Z. Cook, J. Lee, A. Barzilov and W. Yim, "Plug-and-Play Radiation Sensor Components for Unmanned Aerial System Platform," Journal of Radioanalytical and Nuclear Chemistry, vol. 318, no. 3, pp. 1797-1803, 2018. https://doi.org/10.1007/s10967-018-6233-2.

[58] R. Morales-Herrera, A. Fernandez-Caballero, J. A. Somolinos and H. Sira-Ramirez, "Integration of Sensors in Control and Automation System," Journal of Sensors, no. 6415876, 2017.

[59] C. S. a. E. University of Minnesota, "Robotics and Artificial Intelligence," [Online]. Available: https://www.cs.umn.edu/research/research_areas/robotics-and-artificial-intelligence.

[60] M. S. Loffler, V. K. Chitrakaran and D. M. Dawson, "Design and Implementation of the Robotic Platform," in IEEE, Mexico City, Mexico, 2001.

[61] M. Kazemeini, A. Barzilov, J. Lee and W. Yim, "Integration of CZT and CLYC Radiation Detectors into Robotic Platforms using ROS," AIP Conference Proceedings, vol. 2160, pp. 050019-1 – 050019-6. https://doi.org/10.1063/1.5127711.

[62] J. Lee, J. Hartman, Z. Cook, J. Lee, W. Yim and A. Barzilov, "Development of Plug and Play Interchangeable Components for Unmanned Aerial System with Mobile Manipulation Capability," Transactions - American Nuclear Society, vol. 115, pp. 14-21, 2019.

[63] M. Mariscotti, "A Method of Automatic Identifications of Peaks in the Presences of Background and its Applications to Spectrum Analysis," Nuclear Instruments and Methods, vol. 50, pp. 309-320, 1967. doi.org/10.1016/0029-554X(67)90058-4.

[64] M. Kazemeini, A. Barzilov, W. Yim and J. Lee, "Gamma Ray and Neutron Sensors for Remote Monitoring Using Aerial Robotic Platforms," Sensors & Transducers, vol. 229, no. I, pp. 47-54, 2019.

[65] M. Kazemeini, A. Barzilov, G. Vazquez and W. Yim, "UAS Based Remote Sensing for Nuclear Power Plants," Proc. International Congress on Advances in Nuclear Power Plants, Juan-les-Pins, France, 2019.

[66] J. Hartman, A. Barzilov and I. Novikov, "Remote Sensing of Neutron and Gamma Radiation Using Aerial Unmanned Autonomous System," 2015 IEEE Nuclear Science Symposium and Medical Imaging Conference, pp. 1-4, 2015.

[67] P. Guss, T. Stampahar, S. Mukhopadhyay, A. Barzilov and A. Guckes, "Maximum Likelihood Source Localization using Elpasolite Crystals as a Dual Gamma Neutron Directional Detector," in Radiation Detectors: Systems and Applications XVI, 959502, 2015. https://doi.org/10.1117/12.2186179.

[68] A. Barzilov, M. Kazemeini, W. Yim, J. Vargas and I. Novikov, "MLE Localization of Radiation Sources in Aerial Remote Sensing," Proc. International Congress on Advances in Nuclear Power Plants, Juan-Les-Pins, France, 2019.

[69] Z. Cook, M. Kazemeini, A. Barzilov and W. Yim, "On-Board Radiation Sensor and Low Altitude Contour Mapping of Radiation Fields Using UAS Swarm," Proceeding of Waste Management Symposium, Phoenix, Arizona, pp. 1-12, 2018.

[70] A. Guckes and A. Barzilov "Development and deployment of the Collimated Directional Radiation Detection System ", Proc. SPIE 10393, Radiation Detectors in Medicine, Industry, and National Security XVIII, 1039306 (7 September 2017); https://doi.org/10.1117/12.2273205.

[71] "MarvelMind Robotics," 2020. [Online]. Available: https://marvelmind.com/.

[72] T. Goorley, "Initial MCNP6 Release Overview," Nuclear Technology, vol. 180, no. 3, pp. 298-315, 2012.

[73] T. Goorley, M. James, T. Booth, F. Brown, J. Bull, L. Cox, J. Durkee, J. Elson and M. Fensin, "Features of MCNP6," Annals of Nuclear Energy, vol. 87, no. 2, pp. 772-783, 2016.

[74] "Gazebo," 2014. [Online]. Available: http://gazebosim.org/.

[75] J. Till and H. Grogan, "Radiological Risk Assessment and Environmental Analysis," Oxford University Press, New York, 2008.

[76] A. Barzilov, P.C. Womble, "Study of Doppler Broadening of Gamma-Ray Spectra in 14-MeV Neutron Activation Analysis," Journal of Radioanalytical and Nuclear Chemistry, vol. 301, pp.811–819, 2014. https://doi.org/10.1007/s10967-014-3189-8.

[77] K. Nagatani, "Emergency Response to the Nuclear Accident at the Fukushima Daiichi Nuclear Power Plants Using Mobile Rescue Robots," Journal of Field Robotics, pp. 30-44, 2013.

[78] A. Guckes, A. Barzilov, P. Guss, "Directional Detection of Neutrons and Photons using Elpasolites: Computational Study," Radiation Measurements, vol. 124. pp. 127-131, 2019. https://doi.org/10.1016/j.radmeas.2019.04.003.

[79] Z. Cook, M. Kazemeini, A. Barzilov and W. Yim, "Plug-and-Play Radiation Sensor Components for Unmanned Aerial System Platform," Journal of Radioanalytical and Nuclear Chemistry, vol. 318, pp. 1797 – 1803, 2018. https://doi.org/10.1007/s10967-018-6233-2.

[80] M. Kazemeini, A. Barzilov, W. Yim and J. Vaz, "Analysis of Radiation Damage in Electronics of Unmanned Aerial and Ground Robotic Platforms," in Waste Management Symposium, Phoenix, Arizona, pp. 1-8, 2019.

[81] A. Ferrari, P. Sala, A. Fasso and J. anft, "FLUKA: A Multi-Particle Transport Code," 2005.

[82] L. Jones, P. Seller, M. Wilson, A. Hardie, " HEXITEC ASIC - A Pixellated Readout Chip for CZT Detectors, vol. 604, pp 34-37, 2009.

[83] K. Nordlund, "Primary Radiation Damage in Materials," Nuclear Science, vol. NEA, no. 9, 2015.

[84] M. Kazemeini, A. Barzilov, J. Lee and W. Yim, "Study of Radiation Effects in Electronics of a Hexapod Robotic Platform," AIP Conference Proceedings, vol. 2160, pp. 060003-1 – 060003-6, 2018. https://doi.org/10.1063/1.5127720.

[85] S. Yoon, "Evaluation of Radiation Damage Induced by a Proton Beam at the KOMAC Facility," J. Korean Physics Society, pp. 439-442, 2015.

[86] M. D. R. Silva, "Ionizing Radiation Detectors," in Intech, London, England, 2014.

[87] "Mirion Technologies". Introduction to Radiation Detectors.

[88] J. K. Shultis and R. E. Faw, "Radiation Shielding and Radiological Protection," in Handbook of Nuclear Engineering, Manhattan, Kansas, Springer Science Business Media LLC, 2010.

[89] J. F. Ziegler, "SRIM - The Stopping and Range of Ions in Matter".

[90] "Materials Used in Radiation Shielding," Thomas, 2020. [Online]. Available: https://www.thomasnet.com/articles/plant-facility-equipment/radiation-shielding-materials/.

[91] T. Spina, "Correlation Between the Number of Displacements Per Atom and Tc After High-Energy Irradiations of Nb3Sn Wires for the HL-LHC," IEEE, vol. 26, no. 3.

[92] M. A. Amirkhani, M. Asadabad, M. Hassanzadeh, S. M. Mirvakili and A. Mohammadi, "Calculation of dpa rate in graphite box of Tehran Research Reactor," Springer Link, vol. 30, 2019.

'

Curriculum Vitae
Monia Kazemeini
Mkazemeini93@gmail.com

EDUCATION

University of Nevada, Las Vegas   **May 2020**
Doctor of Philosophy, Mechanical Engineering   GPA 3.980
University of Nevada, Las Vegas   **May 2020**
Graduate Certificate, Nuclear Safeguards and Security   GPA 3.980
University of Nevada, Las Vegas   **May 2020**
Graduate Certificate, Nuclear Criticality Safety   GPA 3.980
University of Nevada, Las Vegas   **December 2015**
Bachelor of Science, Mechanical Engineering   GPA 3.552

SKILLS

- o MCNP6
- o SRIM/TRIM
- o FLUKA
- o Igor Pro
- o Robot Operating System (ROS)
- o C++
- o Matlab
- o AutoCad
- o GNU Radio Companion

- o Geant4
- o Solidworks
- o Linux
- o LabVIEW
- o MultiSpect (Kromek)
- o MarvelMind Dashboard
- o Revit
- o Comsol
- o Quickbooks

WORK EXPERIENCE

University of Nevada, Las Vegas   **August 2016 - Present**
Graduate Assistantship
Radiological Contamination Search and Mapping using Unmanned Aerial Systems (UAS)

- Detecting and Analyzing using Cadmium Zinc Telluride (CZT) detector and
$Cs_2LiYCl_6:Ce^{3+}$ scintillation detector
- High-resolution gamma-ray spectroscopy via digital analysis of photo peaks
- Spectral analysis and neutron/gamma pulse shape discrimination (PSD)
- Robot Operating System (ROS) integration with the UAS
- Gradient based source seeking and contour mapping algorithm
- MCNP (Monte Carlo N-Particle) radiation transport code was used to compute radiation fluxes

Mission Support and Test Services (MSTS)   **May 2019 - August 2019**
Student Internship
Applied Technology
- Designing components using Solidworks for multiple projects
- Working with the 3D printer to create the three-dimensional components
- Presentation of components with engineering explanations with deadlines
- GNU Radio Companion to create signal flow graphs and generate source codes
- ASK, FSK, and PSK Modulation

Precision Design Group   **January 2015 - July 2016**
Engineering firm specializing in HVAC
Mechanical Designer II
- Performed HVAC load analysis. Sized HVAC piping and ductwork
- Selected proper HVAC equipment. Documented specifications for projects
- Used training, problem-solving skills, communications in a team environment
- Designed ductwork and piping using Revit and AutoCAD. Visited jobsites

INVOLVEMENT

Las Vegas Business Academy (LVBA) Scholar	Spring 2019 - Current
Mission Support and Test Services (MSTS) Student Ambassador	Fall 2019 - Current
UNLV American Nuclear Society (ANS) Board Member	Fall 2018 - Current
American Nuclear Society (ANS) Student Member	Fall 2016 - Current
UNLV American Nuclear Society (ANS) Vice-President	Fall 2017 - Summer 2018
Conference Nuclear and Emerging Technologies for Space (NETS) Student Program Chair	Spring 2017 - Summer 2018
Institute of Nuclear Materials Management Student Member	Summer 2017 - Spring 2019

HONORS

UNLV College of Engineering Scholar Award (2019)
This inaugural award is given to a graduate student every year for publishing in the top technical journals in their fields.

UAV Methane Sensor Module (2014-2015)   **Mentor: Dr. Alexander Barzilov**
The UAV sensor module houses a methane sensor that is attached onto a quadcopter providing an accurate, measurement system.
  - o **Awards**
    - **2nd place** in the department of Mechanical Engineering at Howard R. Hughes College of Engineering
    - **1st place** in Sustainability Awards in the department of Mechanical Engineering at Howard R. Hughes. College of Engineering

AWARDS AND ACHIEVEMENTS

Nuclear Regulatory Commission Fellowship	Fall 2016 - Current
Roy G. Post Foundation Scholarship	Spring 2020
Las Vegas Business Academy Scholarship	Spring 2019 - Current
Patricia Sastaunik Scholarship	Fall 2019 - Current
UNLV Access Graduate Grant	Fall 2018 - Current
MSTS Hot Shot Award	Summer 2019
Summer Session Scholarship	Summer 2019
Alumni Association Scholarship	Fall 2018-Spring 2018
Differential Fees Funds	Spring 2018/Fall 2018
Beginning Visual Editor Workshop Award	Fall 2018
Southwest Travel Award	Fall 2017
GPSA Book Scholarship	Fall 2017
American Society of Plumbing Engineering Scholarship	Fall 2015
Helen and Roy Kelsall Engineering Scholarship	Fall 2014 - Fall 2015
Differential Engineering Scholarship	Fall 2015
Rebel Achievement Scholarship	Fall 2011 - Fall 2015
Millennium Scholarship	Fall 2011 - Fall 2015

PUBLICATIONS

Peer Reviewed Journal Papers

Kazemeini, M., Barzilov, A., Yim, W., Lee, J., "Gamma Ray and Neutron Sensors for Remote Monitoring Using Aerial Robotic Platforms," Sensors & Transducers 229(1), 47-54 (2019).

Kazemeini, M., Barzilov A., Yim, W., Cook, Z., "Plug-and-Play Radiation Sensor Components for Unmanned Aerial System Platform," Journal of Radioanalytical and Nuclear Chemistry 318, 1797 (2018).

Cook, Z., Kazemeini, M., Barzilov A., Yim, W., "Low-Altitude Contour Mapping of Radiation Fields using UAS Swarm," Intelligent Service Robotics 12, 219-230 (2019).

Book Chapter

Kazemeini, M., Vargas, J., Barzilov, A., Yim, W., "Gamma Ray Measurements Using Unmanned Aerial Systems," Chapter in Gamma Rays, Ed., IntechOpen, London, United Kingdom (2019). DOI: 10.5772/intechopen.82798. Available from: https://www.intechopen.com/online-first/gamma-ray-measurements-using-unmanned-aerialsystems.

Peer Reviewed Conference Proceedings Papers

Kazemeini, M., Barzilov, A., "Remote Radiation Sensing Using Aerial and Ground Platforms," Waste Management Symposium, Phoenix, Arizona. (2020).

Han, C., Kazemeini, M., Barzilov, A., "Computational Study of High Resolution Perovskite Gamma Detector," American Nuclear Society, Raleigh, North Carolina. (2020).

Dobler, J., Novikov, I., Kazemeini, M., Han, C., "Radiation Source Localization in Aerial Sensing using 2D and 3D MLE Methods," American Nuclear Society, Raleigh, North Carolina. (2020).

Barzilov A., Kazemeini, M., "DualMode Radiation Sensor for UAS Platforms," 6th International Electronic Conference on Sensors and Applications, Sciforum. (2019).

Kazemeini, M., Barzilov, A., Yim, W., "Remote Sensing of Radiological Materials in a Wide Area using Unmanned Aerial Systems," Global / Top Fuel 2019, Seattle, Washington. (2019).

Kazemeini, M., Barzilov, A., Yim, W., Vargas, J., "UAS Based Remote Sensing for Nuclear Power Plants," International Congress on Advances in Nuclear Power Plants, Juan-les-Pins, France. (2019).

Barzilov, A., Kazemeini, M., Yim, W., Vargas, J., Novikov, I., "MLE Localization of Radiation Sources in Aerial Remote Sensing," International Congress on Advances in Nuclear Power Plants, Juan-les-Pins, France. (2019).

Kazemeini, M., Barzilov A., Yim, W., Vaz, J., "Analysis of Radiation Damage in Electronics of Unmanned Aerial and Ground Robotic Platforms," Waste Management Symposium, Phoenix Arizona. (2019).

Kazemeini, M., Barzilov A., Lee, J., Yim, W., "Integration of CZT and CLYC Radiation Detectors into Robotic Platform using ROS," 25th Conference on Application of Accelerators in Research and Industry, Grapevine, Texas. (2018).

Kazemeini, M., Barzilov A., Lee, J., Yim, W., "Study of Radiation Effects in Electronics of a Hexapod Robotic Platform," 25th Conference on Application of Accelerators in Research and Industry, Grapevine, Texas. (2018).
        1st Place Winner - Best Poster Award

Cook, Z., Kazemeini, M., Barzilov A., Yim, W., "Radiation Measurement and Contour Mapping

using UAS Swarm," Institute of Nuclear Materials Management, Novel Technologies, Techniques and Methods for Safeguards and Arms Control Verification, Sandia National Laboratories. (2017).

Cook, Z., Kazemeini, M., Barzilov A., Yim, W., "Low-Altitude Contour Mapping of Radiation Fields using UAS Swarm," Waste Management Symposium, Phoenix Arizona. (2017).
Awards: **Paper of Note, Superior Paper Award**

Academic Proceedings
Kazemeini, M., Barzilov, A., "Remote Sensing of Radiological Materials in a Wide Area using Unmanned Aerial Systems," 22nd Annual Research Forum. (2020)
Honorable Mention

Kazemeini, M., Barzilov A., "Radiation Sensors for Remote Monitoring using Unmanned Aerial Systems," Rebel Grad Slam, UNLV. (2019).

Kazemeini, M., Barzilov A., "Study of Radiation Effects in Electronics of a Hexapod Robotic Platform," 21st Annual Research Forum. (2019).

Kazemeini, M., Barzilov A., Lee, J., Yim, W., "Plug -and-Play Radiation Sensor Components for Unmanned Aerial System Platform," 8th Annual Graduate Celebration. (2018).

Kazemeini, M., Barzilov A., "Integration of Radiation Sensors into an Unmanned Aerial Systems Platform," Rebel Grad Slam, UNLV. (2018).
Semi-Finalist

Kazemeini, M., Barzilov A., Yim, W., Cook, Z., "Radiation Measurement and Contour Mapping using UAS Swarm," 20th Annual Graduate & Professional Student Research Forum, UNLV. (2018).

Kazemeini, M., Barzilov A., Lee, J., Yim, W., "High Resolution Gamma-Ray Detector Components for UAS Based Radiation Sensing," 7th Annual Graduate Celebration. (2017).

Kazemeini, M., Barzilov A., Yim, W., Cook, Z., "High Resolution Gamma-Ray Detector Components for UAS Based Radiation Testing," Rebel Grad Slam, UNLV. (2017).
Semi-Finalist

DISSERTATION

Remote Radiation Sensing using Robotic Platforms   Advisor: Dr. Alexander Barzilov
- Improve the capabilities to detect, identify, and locate radiological materials
- Remote sensing allows for the evaluation and monitoring of radiological contamination
- Gamma-ray and neutron sensors were integrated onto the robotic platforms
- Allows for the radiation sensor data to be dynamically tracked and mapped thus enabling further analysis of the radiation flux
- Radiation damage was analyzed and assessed with electronic components shielded, and radiation hardened

EXTERNSHIP

Vegas Golden Knights   January 2020 - March 2020
- Learned the social media aspects of each game
- Assisted with the operations and engineering of the game, including with effectively resolving questions and concerns with upholding high standards
- Supported pre-game and post-game group experiences
- Helped with networking, check-in, and experiences at event

VOLUNTEER WORK

Nevada Regional High School Science Bowl   Spring 2020
- Served as a Scientific judge for high school students competing at the national Science Bowl hosted by the National Nuclear Security Administration at VegasPBS.

Nuclear Scout Workshop   Spring 2018
- Hosted a nuclear workshop for local boy scouts and girl scouts to introduce them to nuclear-related topics

UNLV College of Engineering Mixer   Spring 2018
- Increasing undergraduate membership for American Nuclear Society

UNLV College of Career Fair   Fall 2017
- Assisting in Career Services for UNLV undergraduates and graduate students

Radical Radioactivity Workshop   Fall 2017
- Hosted a tour for prospective undergraduates from Rose Mary Clark Middle School covering Nuclear Topics

Nuclear Scout Workshop   Fall 2017
- Hosted a nuclear workshop for local boy scouts and girl scouts to introduce them to nuclear-related topics